UNIVERSITÄT PADERBORN
Die Universität der Informationsgesellschaft

FAKULTÄT FÜR ELEKTROTECHNIK, INFORMATIK UND MATHEMATIK

Microwave and Millimeter-Wave Interferometers for Contactless Characterization of Dielectric Biomedical Samples

Von der Fakultät für Elektrotechnik, Informatik und Mathematik
der Universität Paderborn

zur Erlangung des akademischen Grades

Doktor der Ingenieurwissenschaften (Dr.-Ing.)

genehmigte Dissertation

von

Dipl.-Ing. Jan Wessel

Erster Gutachter: Prof. Dr.-Ing. Johann Christoph Scheytt
Zweiter Gutachter: Prof. Dr.-Ing. Dietmar Kissinger

Tag der mündlichen Prüfung: 24.05.2018

Paderborn 2018

Diss. EIM-E/342

UNIVERSITÄT PADERBORN
Die Universität der Informationsgesellschaft

FAKULTÄT FÜR
ELEKTROTECHNIK,
INFORMATIK UND
MATHEMATIK

Zusammenfassung der Dissertation:

Mikrowellen- und Millimeterwelleninterferometer zur kontaktlosen Charakterisierung biomedizinischer Dielektrika

des Herrn Jan Wessel

Die vorliegende Arbeit beschreibt die Entwicklung und Evaluierung von hochsensitiven elektrischen Interferometern zur Messung von Permittivität biomedizinischer Materialien. Das Ziel ist die Implementierung eines dielektrischen Sensors, welcher kontaktlose Messungen biomedizinischer Proben ohne den Einsatz optischer Marker ermöglicht. Dazu werden zunächst verschiedene Sensormethoden untersucht. Im Anschluss wird das Zusammenspiel unterschiedlicher Ausleseschaltungen mit der jeweiligen Sensorik behandelt, so dass die finale Strategie für eine optimale Messmethode bestimmt werden kann. Das elektrische Interferometer erweist sich dabei als am besten geeignet und wird daher zunächst auf einer Leiterkarte im Mikrowellenfrequenzbereich realisiert.

Die gewählte Strategie zur Miniaturisierung des Sensors für die Integration in mikrofluidische Aufbauten ist Skalierung. Der Einsatz hoher Frequenzen ermöglicht eine Verkleinerung der Schaltungskomponenten, so dass Sensor- und Probendimensionen vergleichbar sind. Dadurch können selbst Mikropartikel detektiert und charakterisiert werden. Um den Einsatz dieser Methode bei sehr hohen Frequenzen zu erforschen, werden Untersuchungen dielektrischer Probenmaterialien mit einem Dauerstrich-Interferometer und einem bereits bestehenden Millimeterwellensensor-Chip durchgeführt. Zusätzlich wird der Einsatz hoher Frequenzen in der Theorie motiviert und Dispersionseffekte analysiert.

Daraufhin wird ein Millimeterwelleninterferometer als integrierter Schaltkreis für den Betrieb bei 120 GHz entwickelt. Die genutzte Technologie basiert auf einem 130 nm BiCMOS Prozess mit einer f_t/f_{max}-Charakteristik von 240 GHz/330 GHz. Der finale Chip enthält einen spannungsgesteuerten 120 GHz Oszillator mit einem Durchstimmbereich von 7 GHz. Ein Frequenzteiler mit einer Teilerrate von 64 erzeugt Ausgangssignale für den Betrieb mit einem externen Phasenregelkreis. Der Ausgangsverstärker ermöglicht Ausgangsleistungen von 7 dBm bei 120 GHz. Zusätzlich enthält der finale Chip digital gesteuerte Phasenschieber, die auf dem Konzept eines Slow-Wave-Wellenleiters basieren. Diese Schaltungskomponenten sind die Kernelemente des entwickelten Konzepts zur Erfassung dielektrischer Eigenschaften von Proben. Weiterhin wurden ein rauscharmer Verstärker mit 17 dB Verstärkung und ein Leistungsdetektor integriert. Die verschiedenen Betriebsmodi des Interferometers werden untersucht, um den optimalen Einsatz für verschiedene Zielanwendungen zu ermitteln. Das so entstehende System ermöglicht automatisierte und kontaktlose Überwachung der Permittivität von biomedizinischen Proben. Der Sensor-Chip ist somit ein leistungsfähiges Instrument für biomedizinische Messanwendungen und Lab-on-Chip Systeme.

UNIVERSITÄT PADERBORN
Die Universität der Informationsgesellschaft

FAKULTÄT FÜR
ELEKTROTECHNIK,
INFORMATIK UND
MATHEMATIK

Zusammenfassung der Dissertation:

Microwave and Millimeter-Wave Interferometers for Contactless Characterization of Dielectric Biomedical Samples

des Herrn Jan Wessel

This thesis describes the development and evaluation of highly sensitive interferometers for permittivity measurements of biomedical materials. The objective is to engineer a sensor system enabling label-free and contactless characterization of dielectric samples. Initially, various sensing methods are discussed and compared. Subsequently, different approaches serving as read-out circuits suiting the investigated sensors are reviewed. The performance of sensors along with the respective read-out technology are compared to each other leading to the final method of choice: The interferometer is identified to be the best suited technique. It is initially realized on a printed circuit board at microwave frequencies for experimental investigations.

The selected strategy to realize an extremely compact sensor that can be integrated into microfluidic systems is scaling. The exploitation of higher frequency bands to minimize sensor dimensions renders the device and the sample of interest comparable in size. Hence, it is possible to even detect and characterize very small particles. Subsequently, millimeter-wave frequencies are inspected on suitability for permittivity measurements using a continuous wave interferometer as well as a preexisting millimeter-wave sensor integrated circuit. Theoretical investigations of very high frequencies further motivate the usage of the millimeter-wave band and explain dispersion related material parameters.

Finally, the interferometer architecture is scaled to work at 120 GHz and fabricated in a 130 nm BiCMOS process featuring an f_t/f_{max} of 240 GHz/330 GHz. The resulting system includes a 120 GHz voltage-controlled oscillator with a tuning range of 7 GHz. It features a divide-by-64 circuit to enable external phase-locked loop stabilization and a buffer circuit providing 7 dBm of output power at 120 GHz. Additionally, the final chip set contains high-precision and high-resolution phase shifters based on a slow-wave transmission line approach with digital control to provide direct readout ability. The slow-wave phase shifters are the key components for the final interferometer design. A 120 GHz LNA with 17 dB gain and a power detector to provide DC output signals are also realized on chip. The different operation modes of interferometers are evaluated and discussed leading to the identification of an optimum mode for the target cluster of applications. The resulting system enables automated, contactless and label-free permittivity monitoring for biomedical purposes. Hence, it represents a powerful solution for biomedical sensing applications and it provides a platform for future lab-on-chip devices.

Vorveröffentlichungen

[1] J. Wessel, K. Schmalz, J. C. Scheytt, and D. Kissinger, "Sensitive permittivity detector for dielectric samples at 120 GHz," in *Proc. IEEE Radio Wireless Symp.* IEEE, 2018, pp. 1–3.

[2] ——, "A 120-GHz electrical interferometer for contactless permittivity measurements with direct digital read-out," *IEEE Microw. Wireless Compon. Lett.*, vol. 27, no. 2, pp. 198–200, 2017.

[3] J. Wessel, K. Schmalz, C. Meliani, B. P. Cahill, and J. C. Scheytt, "A 7 GHz biosensor for permittivity change with enhanced sensitivity through phase compensation," in *Proc. Eur. Microw. Conf.* IEEE, 2014, pp. 699–702.

[4] J. Wessel, K. Schmalz, J. C. Scheytt, and C. Meliani, "Switchable slow wave transmission line in 130 nm SiGe technology at 115 GHz for phase detection based biosensors," in *Proc. IEEE MTT-S Int. Microw. Symp.* IEEE, 2014, pp. 1–3.

[5] J. Wessel, K. Schmalz, G. Gastrock, B. P. Cahill, and C. Meliani, "Contactless investigations of yeast cell cultivation in the 7 GHz and 240 GHz ranges," in *Proc. Journal of Physics: Conference Series*, vol. 434, no. 1. IOP Publishing, 2013, p. 012033.

[6] J. Wessel, K. Schmalz, B. P. Cahill, G. Gastrock, and C. Meliani, "Contactless characterization of yeast cell cultivation at 7 GHz and 240 GHz," in *Proc. IEEE Topical Conf. Biomed. Wireless Technol. Netw. Sens. Syst.* IEEE, 2013, pp. 70– 72.

[7] J. Wessel, K. Schmalz, J. C. Scheytt, B. P. Cahill, and G. Gastrock, "Microwave biosensor for characterization of compartments in teflon capillaries," in *Proc. Eur. Microw. Conf.* IEEE, 2012, pp. 534–537.

[8] F. I. Jamal, S. Guha, M. H. Eissa, J. Borngräber, C. Meliani, H. J. Ng, D. Kissinger, and J. Wessel, "Low-power miniature K-band sensors for dielectric characterization of biomaterials," *IEEE Transactions on Microwave Theory and Techniques*, vol. 65, no. 3, pp. 1012–1023, 2017.

[9] S. Vogt, M. Detert, D. Wagner, J. Wessel, R. Ramzan, W. Nimphius, A. Ramaswamy, S. Guha, C. Wenger, F. I. Jamal, M. H. Eissa, U. Schumann, B. Schmidt, G. Rose, C. Dahl, I. Rolfe, G. Notzon, C. Baer, and T. Musch, "A newly developed mm-wave sensor for detecting plaques of arterial vessels," *The Thoracic and Cardiovascular Surgeon*, 2017.

[10] M. H. Eissa, F. I. Jamal, S. Guha, C. Meliani, D. Kissinger, and J. Wessel, "Lowpower planar complex dielectric sensor with DC readout circuit in a BiCMOS technology," in *Proc. IEEE MTT-S Int. Microw. Symp.*, 2016, pp. 1–3.

[11] F. I. Jamal, S. Guha, M. H. Eissa, J. Borngräber, C. Meliani, D. Kissinger, and J. Wessel, "Comparison of microstrip stub resonators for dielectric sensing in lowpower K-band VCO," in *Proc. IEEE Topical Conf. Biomed. Wireless Technol. Netw. Sens. Syst.* IEEE, 2016, pp. 59–62.

[12] F. I. Jamal, S. Guha, M. H. Eissa, C. Meliani, D. Kissinger, and J. Wessel, "A 24 GHz dielectric sensor based on distributed architecture," in *Proc. German Microw. Conf.* IEEE, 2016, pp. 173–176.

[13] D. Wagner, F. I. Jamal, S. Guha, C. Wenger, J. Wessel, D. Kissinger, D. Ernst, K. Pitschmann, B. Schmidt, and M. Detert, "Packaging of a BiCMOS sensor on a catheter tip for the characterization of atherosclerotic plaque," in *Proc. IEEE Electron. Syst. Integr. Technol. Conf.* IEEE, 2016, pp. 1–3.

[14] H. J. Ng, J. Wessel, D. Genschow, R. Wang, Y. Sun, and D. Kissinger, "Miniaturized 122 GHz system-on-chip radar sensor with on-chip antennas utilizing a novel antenna design approach," in *Proc. IEEE MTT-S Int. Microw. Symp.*, 2016, pp. 1–4.

[15] F. I. Jamal, S. Guha, M. H. Eissa, C. Meliani, H. J. Ng, D. Kissinger, and J. Wessel, "A fully integrated low-power K-band chem-bio-sensor with on-chip DC read-out in SiGe BiCMOS technology," in *Proc. Eur. Microw. Conf.* IEEE, 2016, pp. 273–276.

[16] K. Schmalz, J. Borngräber, M. Kaynak, W. Winkler, J. Wessel, M. Neshat, and S. Safavi-Naeini, "A 120 GHz dielectric sensor in SiGe BiCMOS," *IEEE Microw. Wireless Compon. Lett.*, vol. 23, no. 1, pp. 46–48, 2013.

Microwave and Millimeter-Wave Interferometers for Contactless Characterization of Dielectric Biomedical Samples

Contents

List of Abbreviations

BiCMOS	bipolar complementary metal-oxide-semiconductor
BW	bandwidth
CMOS	complementary metal-oxide-semiconductor
DFB	twin distributed feedback laser
HBT	heterojunction bipolar transistor
HFSS	high frequency electromagnetic field simulation
IC	integrated circuit
IDC	interdigitated capacitor
ISM	industrial, scientific and medical
LNA	low noise amplifier
LTG	low temperature grown
MIM	metal-insulator-metal
MUT	material under test
PCB	printed circuit board
PM	polarization-maintaining
PTFE	polytetrafluoroethylene
PVC	polyvinyl chloride
RIE	reactive ion etching
S-parameters	scattering parameters
SiGe	silicon-germanium
SMD	surface mount device
SoC	system-on-chip
SOLT	short-open-load-thru
TEM	transverse electromagnetic
VBIC	vertical bipolar inter-company
VCO	voltage-controlled oscillator
VNA	vector network analyzer

1 Introduction

1.1 Motivation

Dielectric sensors for biomedical applications have gained great popularity over the past decade. In medical environments, it is crucial to provide the highest hygienic standards possible to avoid unwanted and dangerous contamination. Some of the methods applied in medical surroundings to sense permittivity and extract information need to be in physical contact to the sample under test. Hence, measurements are often prone to sample contamination and modification. Sensor elements, moreover, are regularly not suited for sterilization using the common cleaning methods. Therefore, it is highly desirable to measure permittivity without contacting the respective element under investigation. Microwave characterization, which renders screening a sample under test without contact feasible, minimizes the chance of contaminating the object of interest. Handling the samples and routing can be done efficiently by using microfluidic systems. That way, the samples can be processed and brought into close proximity to a sensing element. Contactless measurements demand a very high sensitivity, since the electric field needs to penetrate the wall of the respective microfluidic channel and still screen the sample to a sufficient depth. Furthermore, miniaturized sensing structures are required to achieve highly compact systems that can be integrated into the microfluidics. More importantly, when sensor dimensions are minimized to a level where sensing device and the object of interest are comparable in size, even very small particles can be detected and characterized.

Dielectric sensors have versatile application fields. A particular showcase, one of the target applications addressed in this thesis, is the monitoring of microorganism cultivation progress. The demand arises from the modern food industry as well as many biotechnological applications, which make use of a variety of microorganisms. Microorganisms serve as a functionalizing element in various products e.g. tooth paste, textiles or washing powder [17, 18]. Researchers working in this field assume that less than one percent of the existing microorganisms have been discovered and put into cultivation [19]. Standard cultivation techniques, like those based on microtiter plates and shake flasks, do not allow for a very high throughput, so that the process of finding and cultivating new specimens is slow and expensive. The approach presented in [20] is called segmented flow cultivation and is a highly parallel method enabling faster discovery of new specimens. Small droplets, consisting of a nutrient solution and potentially one single microorganism, are created and stored in microfluidic channels. Fig. 1-1 depicts the general process of compartment generation. The two syringes displayed in Fig. 1-1 exhibit different diameters and are driven by a single syringe pump device for synchronization. One syringe contains the sample with cells and a nutrient medium. The second syringe is filled with a hydrophobic separation medium, to isolate the single droplets. The injector chip depicted in Fig. 1-1 is utilized to merge the fluids and generate the segments of sample medium confined within the separation fluid. Subsequently, the droplets are collected into a Teflon tube. The droplets, referred to as compartments, are small bioreactors. The compartments inside the microfluidic system are shown in Fig. 1-2. They have a volume of about 60 nl in the depicted case. The ultra high throughput that is achievable with this cultivation

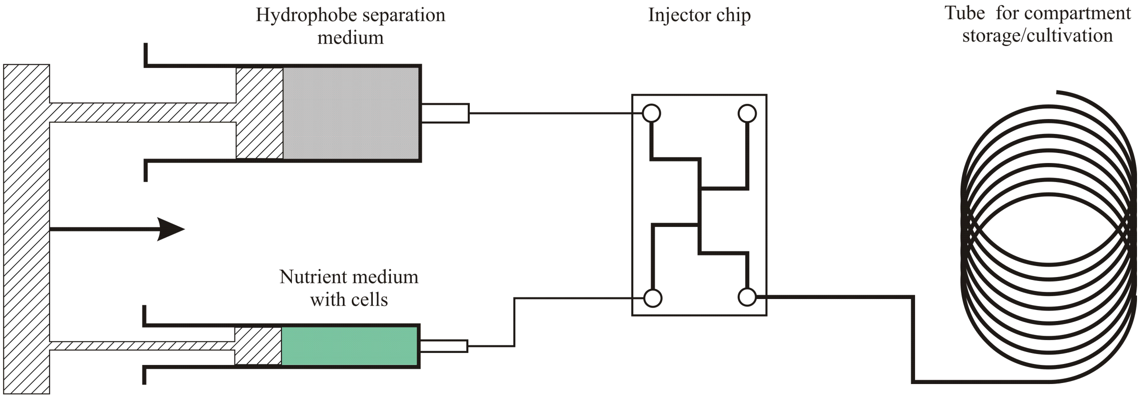

Figure 1-1: *Segmented flow procedure for compartment generation.*

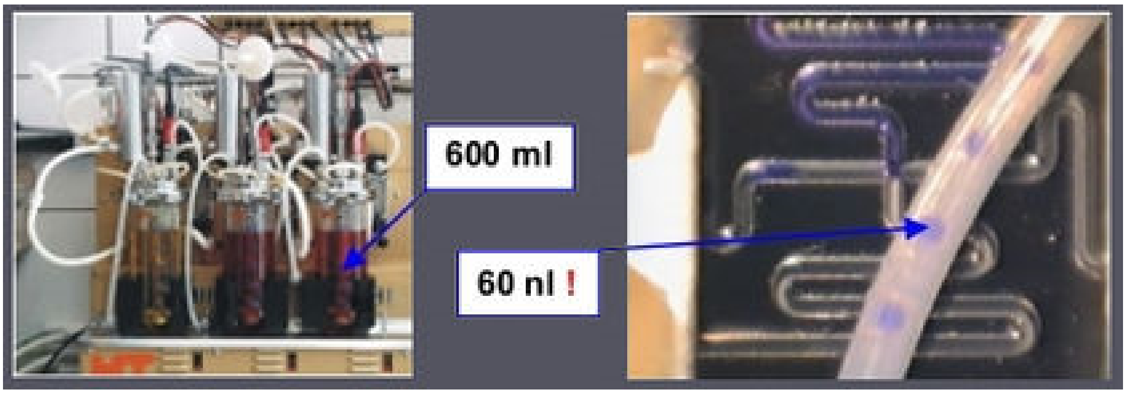

Figure 1-2: *Picture of compartments used as bioreactors for cell cultivation [27].*

procedure demands new techniques to monitor the progress of cultivation within those compartments efficiently and reliably. Moreover, it is desirable to characterize the stadium of cultivation contactless and without any kind of markers. As described in [21], the characterization of the cultivation stadium is usually observed via indirect verification procedures like the ones presented in [22,23], demanding visual markers. In order to exert effective process control over the compartment based cell cultivation, there is the need for contactless and label-free solutions.

The technique chosen in this thesis is based on dielectric sensing. An increasing number of cells within a single compartment affects the average permittivity, which is detectable using microwave spectroscopy. The permittivity of disperse substances has been actively studied, thus, detailed models for disperse media can be found in the literature [24–26]. The conclusion to draw is that dielectric sensors are well suited for characterization of cell numbers in carrier fluids and hence cultivation states.

1.2 Objective

This work's core objective is to develop a generic dielectric sensor for versatile biomedical applications. Target samples for investigation are assumed to be in very low volumes in the nanoliter scale, which is regularly the case in both biological and medical environments. Hence, the sensor needs to be highly sensitive to be able to detect marginal changes

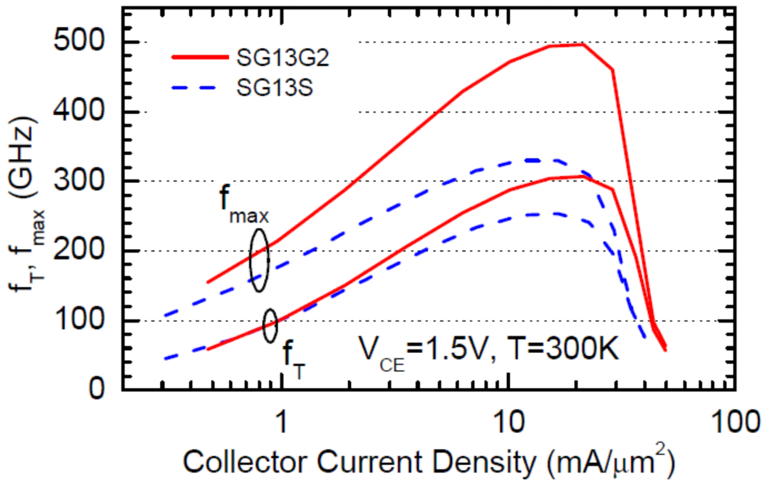

Figure 1-3: *f_T and f_{max} versus collector current density of heterojunction bipolar transistors in the target bipolar complementary metal-oxide-semiconductor (BiCMOS) technology [28].*

in samples under test. The sensor dimensions have to be in the scale of samples, so that a sufficiently high sensitivity can be achieved. This further encourages the development of a miniature sensor system. The sensor should be capable of sample characterization without the need for additional, bulky lab equipment. Hence, an integrated solution needs to be developed to provide a highly compact, miniature device, which embeds all features required for a dielectric sensor system providing several important features like sensor calibration and sample read out directly on chip.

1.3 Strategy

A suitable mechanism to miniaturize circuits and microchips is the application of high frequencies. The dimensions of passive devices scale with the wave length so that for higher frequencies, smaller components can be designed. From the perspective of active integrated circuits, using millimeter-wave frequencies can be a delicate procedure in terms of device performance regarding noise and maintenance of a suitable amount of amplifier gain. Hence, the pros and cons of high frequency bands need to be carefully studied.

The combination of different requirements, which are high performance active circuits at millimeter-wave frequencies and system complexity for system-on-chip (SoC) solutions make a silicon-germanium (SiGe) technology favorable for the final design. Silicon germanium heterojunction bipolar transistor (HBT)s show a much better performance compared to complementary metal-oxide-semiconductor (CMOS) transistors for device dimensions in the same scale. This technology is suitable for the development of ultra high frequency integrated circuits. The final technology of choice is a 130 nm BiCMOS process, described in section 6.2. Its performance and suitability for the development of millimeter-wave circuits was demonstrated in [28] by the f_t/f_{max} characteristics depicted in Fig. 1-3. Moreover, SiGe technologies are known for equal cost and performance benefits, potentially interesting for product-oriented design.

Since the BiCMOS platform is based on a Silicon CMOS platform and provides high speed HBTs, it is well suited for high volume applications where pure CMOS technologies cannot provide the required performance. Other technologies with similar or better performance used in military applications prove too expensive for the target applications. Along with design flexibility allowing for the combination of high-performance analog blocks with digital logic units in low cost designs, these features make the 130 nm SiGe process the technology of choice.

This work describes the development of a millimeter-wave sensor device featuring a high sensitivity while fulfilling the geometrical demands for lab-on-chip approaches. For that purpose, in the beginning, relevant methods for permittivity measurements are discussed and the method of choice is indicated in chapter 2. Chapter 3 explains the read-out circuits required to complete the sensors for putting them into operation.

Based on conclusions from chapters 2 and 3, the final decision for the method of choice is presented and explained. Chapter 4 presents a first implementation of an interferometer, which was identified to be the best suited approach for the target applications. It is realized on a printed circuit board (PCB) at microwave frequencies to obtain first proof of concept. By utilizing the microwave interferometer, the target approach is evaluated experimentally to verify theoretical investigations. This way the applicability of the concept can be tested and its functionality is demonstrated.

To investigate the feasibility of very high frequencies for dielectric screening, processes at millimeter-wave frequencies are tested and experiments using continuous-wave spectroscopy as well as measurements with available millimeter-wave sensor technologies are conducted. These are presented and evaluated in chapter 5. Considering the target applications, the analyses from chapters 2-5 lead to the conclusion that a mixed signal integrated circuit (IC) design of a millimeter-wave interferometer is the best choice.

The physical implementation of the final on-chip millimeter-wave interferometer along with measurements and simulation results are detailed in chapter 6. A mathematical model for permittivity extraction from measurements is presented. Subsequently, chapter 7 gives a summary of this thesis and conclusions. Finally, a lab-on-chip system with microfluidics integrated in silicon is discussed as an outlook based on the presented sensor IC design.

2 Dielectric Sensors

The applications for dielectric sensors mentioned in chapter 1 require the sensor to operate contactless to guarantee a clean and sterile procedure for characterizing samples of interest without physical contact. A very efficient way to achieve this is to apply electromagnetic waves to screen the matter of interest. The material under test (MUT) is affecting the waves penetrating it so that the transmitted and reflected radiation carries information about its permittivity. There are different approaches to determine the dielectric properties of materials which can be classified as either lumped or distributed sensing elements. Furthermore, both categories provide resonant and non-resonant methods. The following subsections deal with different sensor approaches. Their advantages and drawbacks will be evaluated in the context of the respective read-out procedure in chapter 3.

2.1 Interdigitated Capacitor Detection

The first sensing element up for discussion is an interdigitated capacitor (IDC). It can be classified as a lumped element type sensor. It is featuring a planar structure, making it feasible for on-chip integration. Fig. 2-1 shows the principle layout of an IDC. The two electrodes forming a capacitor consist of a set of N metal fingers respectively and are closely coupled to each other as indicated in Fig. 2-1. Layout dimensions are defined by the length L, the line spacing S and the line width W. To describe this kind of device analytically, the capacitance of a unit cell can be calculated by means of conformal mapping

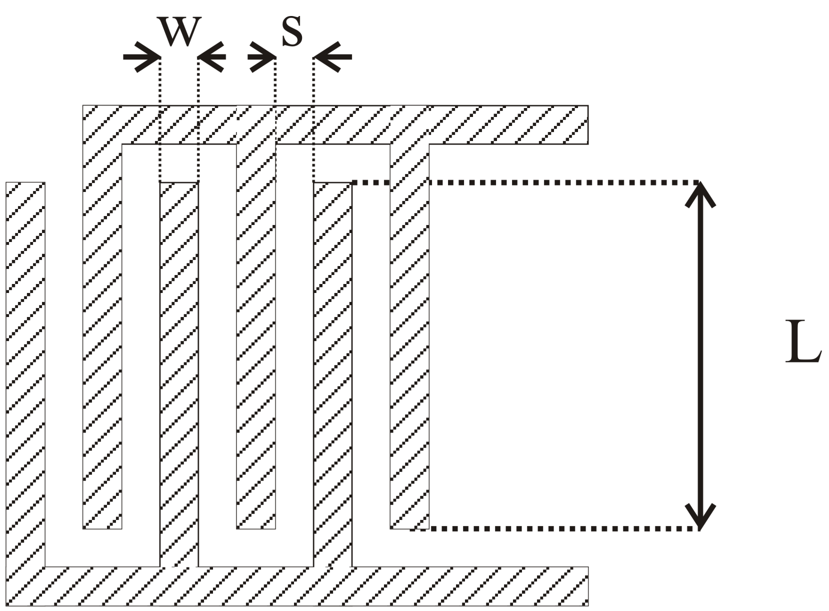

Figure 2-1: *Interdigitated electrode with electrode width W, spacing S, and overlap length L.*

and integral calculations [29] leading to:

$$C_U = \frac{\varepsilon_0 \varepsilon_r K[\sqrt{1-k^2}]}{2K(k)} \tag{2-1}$$

Here, $K(k)$ is the complete elliptic integral of the first kind and k is a geometrical parameter. The parameter N describes the number of metal fingers each of the two electrodes are composed of. For $N > 2$, k is calculated as follows:

$$k = \cos\left(\frac{\pi}{2}\frac{W}{S+W}\right) \tag{2-2}$$

The quotient $(W)/(S+W)$ describing the metal density of the surface is called metallization ratio. To obtain the overall capacitance of the complete IDC, (2-3) is applied:

$$C_{IDC} = (N-1)\,LC_U \tag{2-3}$$

One way to use the IDC as a permittivity sensor is to cover the planar device with a particular material of interest so that the setup displayed in Fig. 2-2 is obtained. The

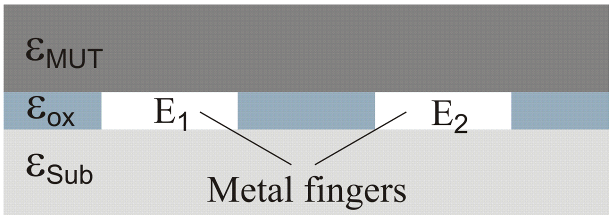

Figure 2-2: *Cross section of IDC with MUT.*

two electrodes E_1 and E_2 are separated from each other by an oxide featuring a dielectric constant ε_{ox}. The underlying substrate has a permittivity of ε_{Sub} and the sample of interest ε_{MUT}. The dielectric material on top of the device is effecting the electrical properties of the capacitor.

Deductions from [29] yield in a set of equations that allow for the extraction of the conductivity of a particular liquid MUT. Measuring the IDC's capacitance the permittivity is calculated by applying (2-1). The remaining parts in (2-1) are entirely based on the IDC's dimensions. Using Ohm's law and the Maxwell equations, Olthuis et al. derived the following relation:

$$RC_{IDC} = \varepsilon_0 \varepsilon_r / \sigma \tag{2-4}$$

In (2-4), σ is the conductivity of the sample and R the IDC's resistance. It is possible to measure the resistance and extract the MUT conductance with the help of (2-5):

$$\sigma = \frac{2K(k)}{R\,(N-1)\,LK[\sqrt{1-k^2}]} \tag{2-5}$$

The cell constant describes the proportionality between the measured resistance of a device and the specific resistance of an MUT leading to (2-6):

$$\kappa = R/\rho = R\sigma \tag{2-6}$$

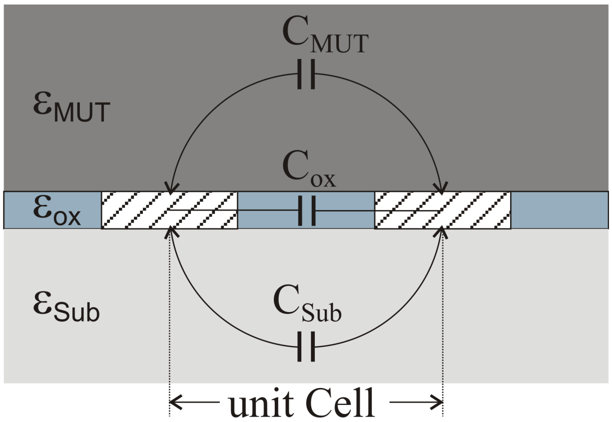

Figure 2-3: *Equivalent schematic of passivated IDC.*

The obtained analytic description of the cell constant derived in [29] is (2-7):

$$\kappa = \frac{2K(k)}{(N-1)\,LK\left[\sqrt{1-k^2}\right]} \tag{2-7}$$

In [29] the cell constant was used to compare experimental results to analytical calculations and a discrepancy of up to 20 % was demonstrated.

Using the definition of the complex relative permittivity, the real part of the permittivity can be derived as follows:

$$\varepsilon' = \frac{\kappa C_{IDC}}{(N-1)\,L} \tag{2-8}$$

The imaginary part is obtained applying (2-9):

$$\varepsilon'' = \frac{\kappa}{\omega R} \tag{2-9}$$

With the help of equations (2-8) and (2-9) it is possible to extract the complex permittivity from the measured capacitance and resistance of the IDC.

A method to obtain permittivity values from bio impedance spectroscopy using IDCs was presented by several research groups [30–33]. The presented methods generally combine analytical calculation schemes and circuit theory, using equivalent circuits representing the IDC device. Fig. 2-3 displays an example of an equivalent schematic for a standard IDC cell. In the depicted case, the capacitance per unit length C_U consists of three parts:

$$C_U = C_{ox} + C_{Sub} + C_{MUT} \tag{2-10}$$

C_{ox} is contributed by the isolation layer which is silicon oxide, C_{Sub} by the substrate and C_{MUT} is the parameter stemming from the potential material under test, which is on top of the IDC. The sum of C_{Sub} and C_{MUT} can again be derived using the elliptic integral K. The overall capacitance of the IDC can be calculated from the unit cell capacitance based on the number of IDCs metal fingers. The MUT capacitance is depending on its permittivity, hence providing the opportunity to extract the dielectric characteristics of the MUT from the overall capacitance.

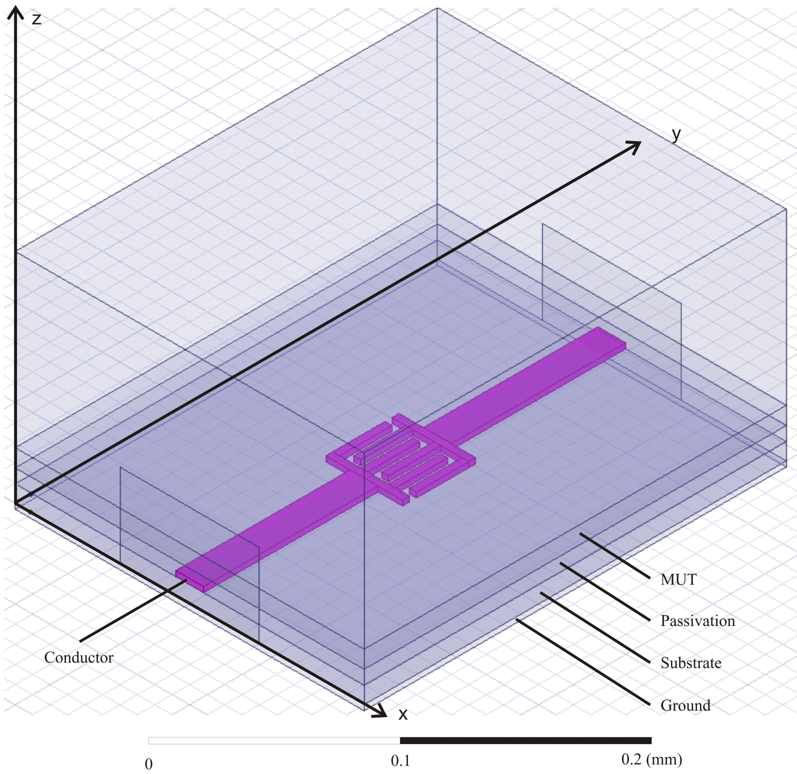

Figure 2-4: *IDC model in HFSS for EM simulations.*

In biomedical applications, it is usually highly desired to apply contactless methods. The approach presented in [33] makes use of electrodes that are covered by a silicon nitride passivation layer, a layer, that is not accounted for in the first calculation step but needs to be considered to obtain accurate results. That passivation layer is separating the material under test from the IDC, protecting the device and the sample. The correlation of the IDC capacitance taking the passivation into account and MUT permittivity at 12 GHz has been investigated in [33]. To analyze the discussed measurement technique, the IDC was modeled using high frequency electromagnetic field simulation (HFSS) to simulate the response of the architecture to permittivity changes of MUTs at 12 GHz. The model is depicted in Fig. 2-4. For simulation purposes, the IDC is connected via 50 Ω microstrip lines fed by wave ports to obtain scattering parameters for device characterization.

One important aspect investigating dielectric sensors is their sensitivity. In the target technology, the passivation, separating the electrodes from MUTs, is a silicon nitride layer on top of the sensor. The sensor response to a distinct sample on top is directly depending on the volume that is penetrated by the electromagnetic fields surrounding the conducting fingers of the IDC. That means, the passivation layer should be as thin as possible to keep the distance between MUT and sensor small and maximize the penetration depth into the MUT. However, it also needs to be resilient in liquids to provide protection for the circuits requiring a certain thickness. The sensor response to fluids exhibiting different permittivities was simulated for a varied thickness of passivation layers to investigate that effect.

The parameter of interest is the IDC reactance, since electromagnetic energy is coupled into the material by capacitive effects, reflected in the reactive part of the impedance. The

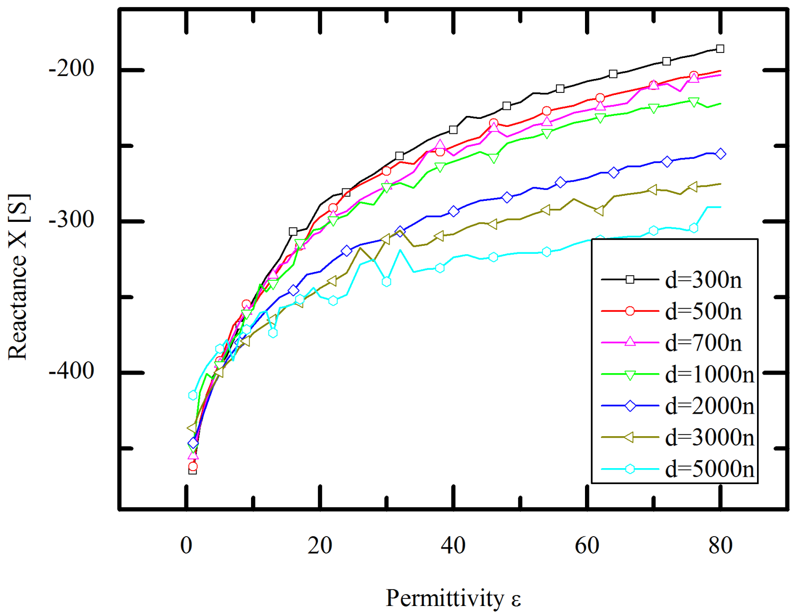

Figure 2-5: *IDC reactance versus MUT permittivity for different thickness of SiO_2 passivation layer.*

obtained simulation results for the IDC reactance are depicted in Fig. 2-5. The important parameter regarding the sensitivity is the change of capacitance with permittivity change $\delta C/\delta\varepsilon$, since it is desired to distinguish between different dielectric MUTs. These investigations confirmed the assumption, that a thinner passivation layer allows for a higher sensitivity, as indicated in Fig. 2-5. The observed effect is stemming from a smaller effective cross section that is screened by the electromagnetic radiation for an increased silicon nitride thickness. The simulations proof that this kind of sensor can be applied for dielectric characterization. Still, the overall sensor sensitivity can only be evaluated in conjunction with the respective read-out circuitry. Both parts of a sensing system need to be characterized as a unit, which is done in 3.1.

2.2 Patch Antenna Detection

The concept of resonant structures as dielectric sensors is widely used, as in cavity or split-ring resonators [34–37]. Using patch antennas for dielectric characterization of materials has been investigated for several decades by many researchers [38–42]. The geometry of such an antenna is sketched in Fig. 2-6. The geometrical parameters d, W and L designated in Fig. 2-6 define the resonance frequency of the patch. Despite these values, the antenna characteristics like input impedance and Q factor are dependent of the dielectric material located on top of the patch. Thus, when a material is placed on top of that structure, the impedance, the resonance frequency and the Q factor carry information about the complex dielectric properties of that material which can be extracted applying the appropriate models. Using a transmission line model, the resonance frequency can be calculated using the following equation [43]:

$$f_r = \frac{c_0}{2(L + 2\Delta L)\sqrt{\varepsilon_{r,eff}}} \tag{2-11}$$

In this equation, c_0 is the speed of light in vacuum. Both the material on top of the patch and the substrate material affect the complex effective permittivity $\varepsilon_{r,eff}$. The concept of effective permittivity is explained in detail later in this chapter. The impact of fringing fields is accounted for by ΔL, a virtual length that is added, increasing the electrical length of the patch. Experimental results presented in [44] were evaluated in [45] to obtain (2-12) by transforming the capacitance to the virtual line extension ΔL:

$$\Delta L/h = 0.412 \frac{\left(\varepsilon_{r,eff} + 0.3\right)\left(\frac{W}{h} + 0.262\right)}{\left(\varepsilon_{r,eff} - 0.258\right)\left(\frac{W}{h} + 0.813\right)} \tag{2-12}$$

In (2-12), W is the width of the patch and h is the thickness of the substrate. Applying (2-12) to replace ΔL in (2-11), an expression is obtained linking the resonance frequency to the effective permittivity of the patch covered by an MUT. Solving this expression for the effective permittivity, the inverse function $\varepsilon_{r,eff} = f(f_r)$ is obtained. That analytical expression is very complicated and not practical for comparison with other sensing methods. Hence, it is numerically solved for a particular patch antenna working around 60 GHz presented later in this section.

In standard designs, the patch is uncovered so that there is free space above the metal. The patch antenna is very sensitive against permittivity changes in the covering material since the complete surface of the device is in close proximity to the MUT and hence effected by it. However, this makes it also prone to malfunction caused by the MUT loss, saying that it might loose its resonant nature. As a consequence, the choice of samples is limited to low loss materials. To obtain the complex dielectric constant of a material, it is necessary to measure both, frequency of resonance and loss tangent. From the resonance frequency it is possible to extract the effective permittivity applying 2-11 and (2-12). To identify real and imaginary parts, the loss needs to be taken into account. The loss tangent is related to the permittivity as follows:

$$tan\delta = \frac{\varepsilon''_{r,eff}}{\varepsilon''_{r,eff}} = \frac{1}{Q_d} \tag{2-13}$$

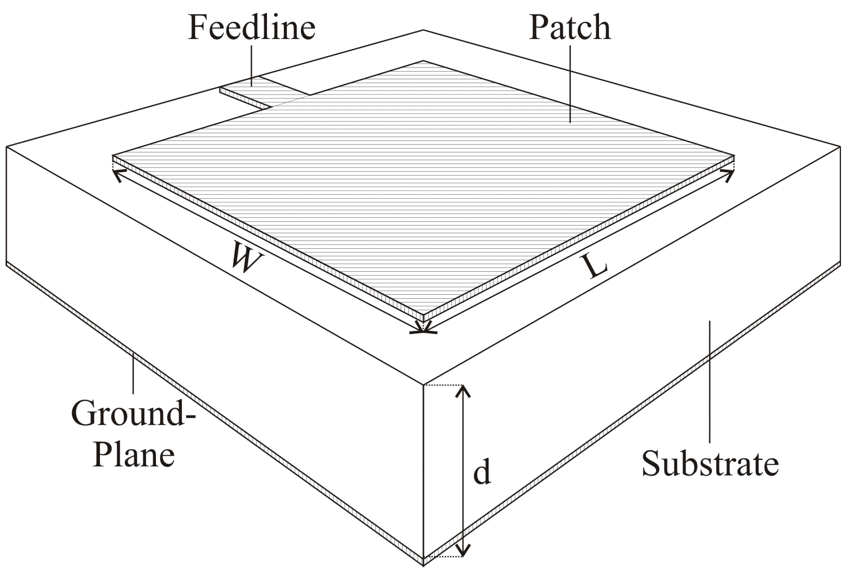

Figure 2-6: *Patch antenna schematic drawing.*

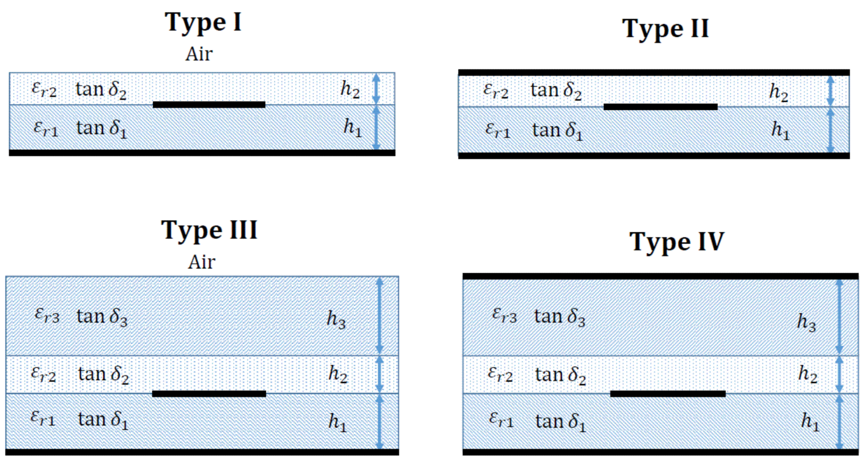

Figure 2-7: *Cross sections of the patch versions investigated in [48].*

In (2-13), Q_d is the part of the total quality factor representing dielectric loss. The total quality factor encloses all antenna losses and is a figure-of-merit. Losses stem from radiations Q_{rad}, conductor loss Q_C, dielectric and surface wave losses Q_{SW}. Therefore, the total quality factor Q_t, influenced by all of these losses, can be written as [46]:

$$\frac{1}{Q_t} = \frac{1}{Q_{rad}} + \frac{1}{Q_C} + \frac{1}{Q_d} + \frac{1}{Q_{SW}} \tag{2-14}$$

The total quality factor can be retrieved from measurements determining the voltage standing wave ratio (VSWR) and the bandwidth (BW) according to [46]:

$$BW = \frac{\Delta f}{f_0} = \frac{VSWR - 1}{Q_t \sqrt{(VSVR)}} \tag{2-15}$$

The different loss mechanisms can be modeled by the following set of equations:

$$\begin{aligned} Q_C &= h\sqrt{\pi f \mu \sigma} \\ Q_{rad} &= \frac{2\omega\varepsilon_r}{hG_t/l}K \\ Q_{sw} &= Q_{rad}\frac{P_{sp}}{P_{sw}} \end{aligned} \tag{2-16}$$

In (2-16), h is the substrate height, μ is the permeability, σ the conductivity of the conductor, G_t/l the total conductance per unit length and K the radiating aperture. A closed form expression to derive space wave power P_{sp} and the surface wave power P_{sw} as well as their accuracy can be found in [47].

From measurements of the return loss and the analytical evaluation applying (2-11)-(2-16), it is possible to extract the complex effective dielectric constant of the material on top of a patch antenna. At first, the real part of the dielectric constant is extracted from the resonance frequency. The total Q factor is obtained by measurements so that (2-14) can be applied to calculate Q_d. Finally, the imaginary dielectric constant is gained using (2-13).

The response of different variants of patch antennas has been investigated in [48]. The structures under investigation are depicted in Fig. 2-7. The parameters are designed for

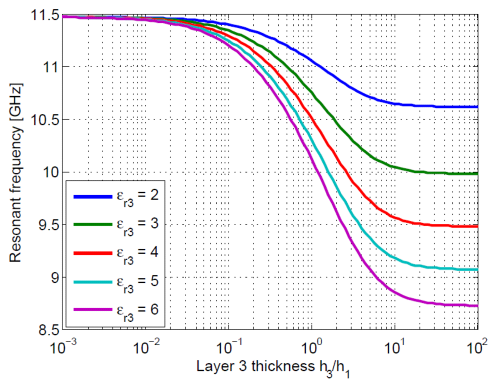

(a) *Resonance frequency shifts.*

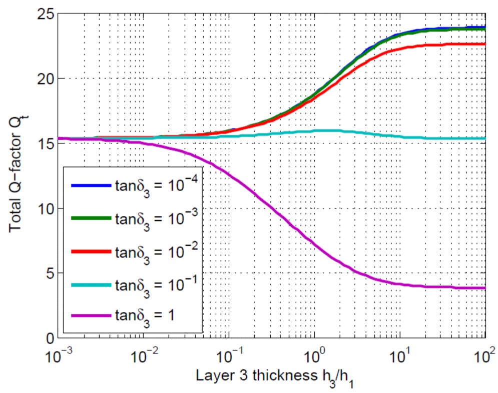

(b) *Q-factor shifts.*

Figure 2-8: *Measurements, type III patch and fixed layer parameters h_1 and h_2 [48]*

the patch to work in the X-band (8-12 GHz). These variants differ in number of layers as well as backplane type - air versus metal. To compare it to the other approaches considered in this thesis, only type 3 is of interest with respect to the target application and the fact that measuring needs to be contact-less. The layer directly above the metal with the thickness h_2 in Fig. 2-7 can be regarded as a passivation layer, separating the metal patch of the sensor from the MUT.

The patch has been characterized in [48] using HFSS for 3D EM simulations. The shift in resonance frequency according to those results is depicted in Fig. 2-8a. The graphs visualize the impact of the superstrate layer onto the patch behavior. Therefore, the layer thickness h_3 as well as the permittivity ε_3 are swept. It is demonstrated that for values of h_3 higher than a certain threshold, the superstrate's thickness does not affect the behavior of the patch anymore. Simultaneously, the sensitivity of the patch in terms of resonance frequency versus permittivity reaches its maximum value. To also investigate the sensor response to changes in the loss tangent of a respective MUT, the total quality factor was extracted from the conducted simulations. The results for different h_3 and $tan\delta$ values are shown in Fig. 2-8b. A behavior similar to that of the resonance frequency is observed for the Q-factor when h_3 reaches a certain threshold. As a conclusion, the simulation results proof that a patch antenna is suitable as a complex dielectric sensor. Using it in a constellation where the MUT is placed on top as a superstrate layer (Type III), a sufficient sample volume must be provided to obtain the necessary sensitivity. Moreover, the loss tangent may not exceed values corrupting the device's resonance. In [48], to be able to accurately characterize the MUT, low loss materials are investigated.

Compared to other dielectric sensors considered in this thesis, the patch antenna is quite bulky, especially at relatively low frequencies like the K band. With respect to the target applications, it is important to miniaturize the device. This can be accomplished by using higher frequencies of operation. Patch antennas working around 60 GHz have been investigated in [39]. The resonance frequency for the dimensions given in [39] was derived with respect to the effective permittivity using (2-12) and (2-11). Solving the expression for $\epsilon_{r,eff}$ yields the relation represented by the graph displayed in Fig. 2-9. It shows that the effective permittivity can be extracted from the resonance frequency. The relation between the MUT permittivity and the effective permittivity is based on transmission line theory and will be presented in section 2.4. In [39] it was demonstrated that the patch antenna is also capable of detecting liquid MUTs at millimeter-wave frequencies. Measurements presented there are depicted in Fig. 2-10. They show the shifted center frequency of the measured input return loss. The change in resonance frequency along with a varied Q-factor make this structure suitable for complex dielectric sensing. However, using patch resonators for extracting the loss tangent or the imaginary part of the dielectric constant of an MUT presented in [49], [50] and [48] showed errors of 12 % and higher. The reported accuracy of the real part of the dielectric constant was in the range of 2 %.

2.3 Open-Ended Coaxial Detection

A solution that allows the acquisition of broadband information on a material's permittivity is the reflection type approach presented in [51] using an open-ended coaxial probe. The probe needs to be in contact with the MUT or with an interim layer, depending on the required sensitivity in the respective application. The resulting setup is sketched in Fig. 2-11. Along with a vector network analyzer (VNA) a transverse electromagnetic (TEM) wave is excited in the coaxial system and partially reflected at the interface of the probe and the MUT, as sketched in Fig. 2-11. Evaluating the reflection coefficient of the setup, information on the sample permittivity is obtained, since the admittance of the coaxial probe is affected by the MUT according to (2-17).

$$\underline{Y}(\omega, \underline{\varepsilon}_r) = j\omega Z_0(\underline{\varepsilon}_r C_0 + C_f) \tag{2-17}$$

This equation has been presented in [51]. Z_0 refers to the TEM characteristic impedance. C_f represents the fringing field in the dielectric material of the cable, and another parallel capacitance C_0 represents the fringing field in the external dielectric material. The change

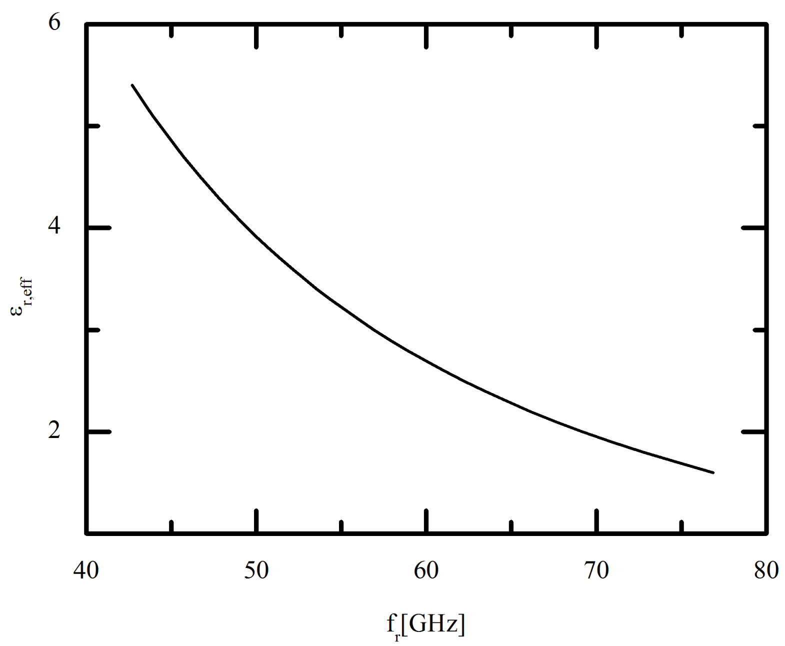

Figure 2-9: *Effective permittivity versus resonance frequency of the 60 GHz patch.*

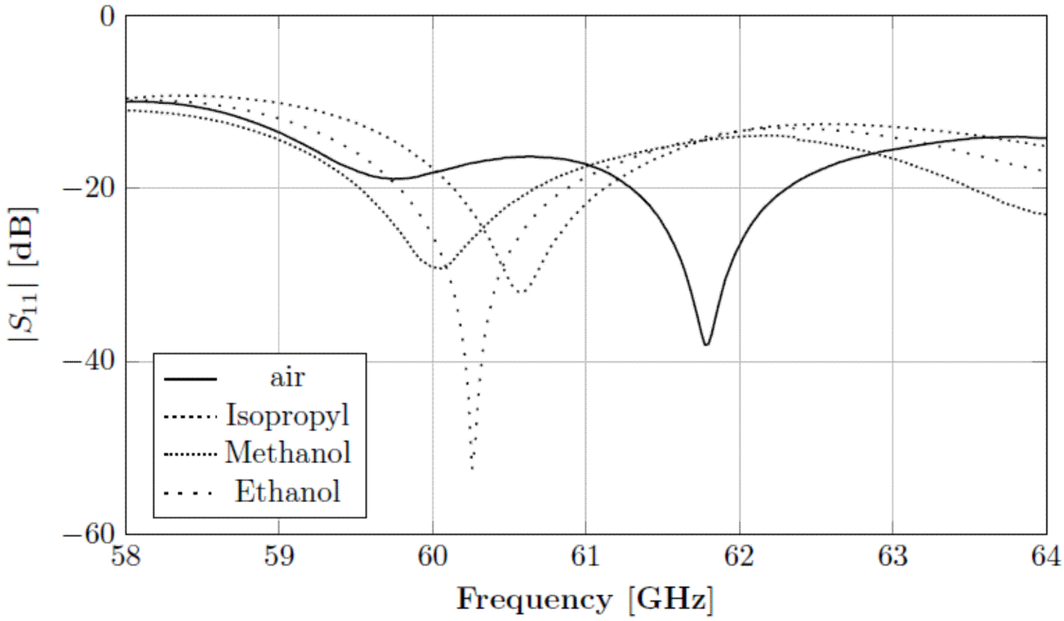

Figure 2-10: *Measured magnitude of S_{11} for different liquid materials on top of the patch antenna [39].*

in the admittance can be investigated by reflection measurements using the VNA since the admittance altering the incident wave $\underline{a}_{1-MUT}$ and the reflected wave $\underline{b}_{1-MUT}$ is determining the reflection coefficient S_{11}. The results are subsequently used to extract the MUT permittivity. The method is explained in detail in [52]. Thorough investigations on the permittivity extraction from reflection measurements using open-ended coaxial probes as well as the accuracy of that technique are presented in [53]. Complying with the geometrical and electrical limitations discussed in [53], the complex permittivity can be obtained by reflection measurements along with equations (2-18) and (2-19):

$$\varepsilon' = \frac{2S_{11}\sin(-\phi)}{\omega Z_0 C_0(1 + 2S_{11}\cos\phi + 2S_{11}^2)} - \frac{C_f}{C_0} \tag{2-18}$$

$$\varepsilon'' = \frac{1 - S_{11}^2}{\omega Z_0 C_0(1 + 2S_{11}\cos\phi + 2S_{11}^2)} \tag{2-19}$$

S_{11} is the magnitude and ϕ the phase of the measured reflection. Z_0 is the characteristic impedance of the unloaded coaxial probe and ω is the angular frequency. The particular termination can be modeled with a load impedance consisting of two parallel capacitances C_f and C_0. C_f accounts for the fringe field independent of the sample. It stems from the air-filled part of the coaxial line and C_0 from the field inside the MUT. The ratio C_o/C_f can be determined from measurements using dielectrics, exhibiting a known permittivity [54]. As an example, measurements on particular dielectrics with a 14 mm coaxial line yielded $C_o/C_f = 0.2$ [54].

It is also possible to extend this method by a second port and probe for transmission measurements, S_{21} to gain additional information about the sample under test. This has also

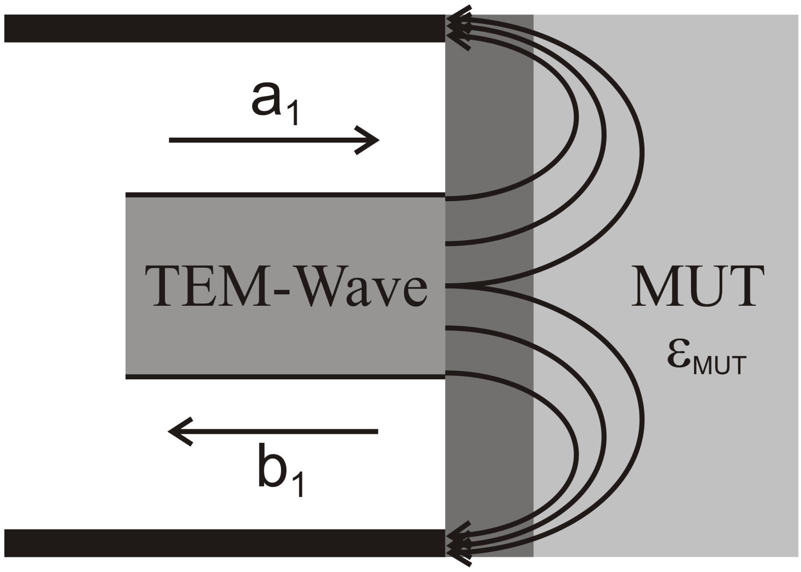

Figure 2-11: *Open-ended coaxial probe for reflection measurements.*

been investigated in [52]. The main information here is in the wavenumber of the material that is screened by the EM signal. In [52], the change of glucose concentration was the parameter of interest. It is affecting the permittivity, and with that the wave number for a propagated signal. The described effect is demonstrated by the graphs depicted in Fig. 2-12. The change of the wavenumber is reflected in both: reflection and transmission of the signal emitted by the open ended coaxial probe tip. Hence, reflection and transmission measurements can be used for material characterization. This method also needs further evaluation which is feasible with an appropriate read-out architecture. The sensitivity strongly depends on the device that is used for S-parameter measurements. The overall performance of sensing and read-out unit is discussed in 3.2.

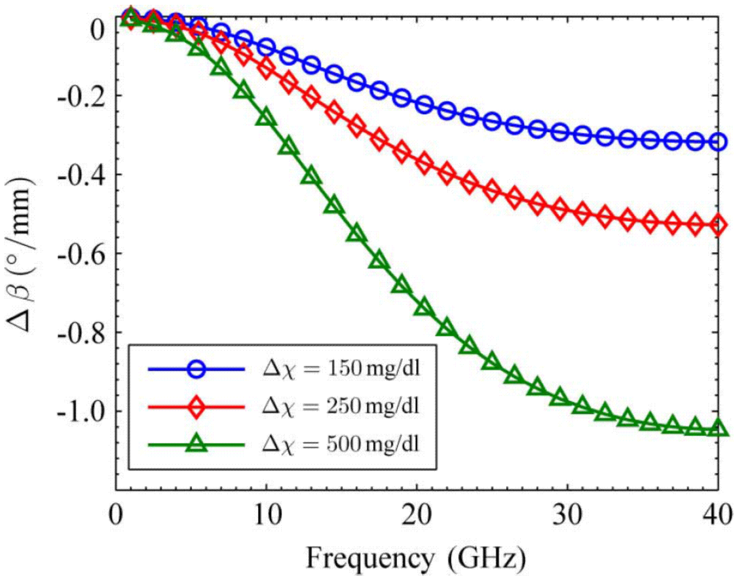

Figure 2-12: *Variation of the wave number for a plane wave in aqueous glucose solution obtained by numerical simulations [52].*

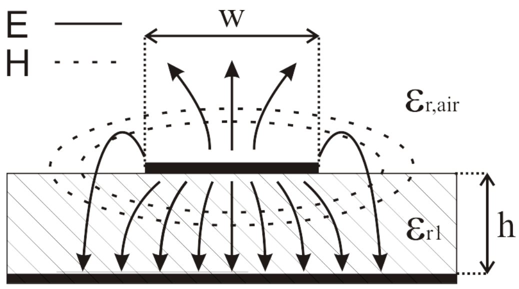

Figure 2-13: *Microstrip crosssection and qualitative field distribution.*

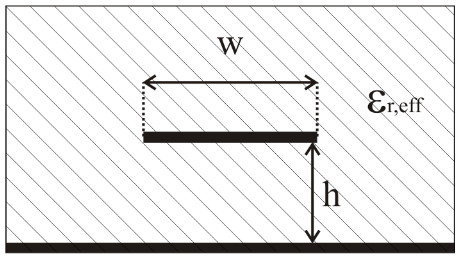

Figure 2-14: *Model of the equivalent microstrip setup with effective dielectric constant.*

2.4 Transmission Line Detection

The detection using a microstrip line is based on the permittivity dependent wave propagation and the concept of effective permittivity. The setup of a microstrip is sketched in Fig. 2-13. The ground conductor with the width w is separated by the ground plane by the substrate exhibiting a dielectric constant of ε_{r1} and the height h. Since the microstrip has an asymmetrical cross section compared to striplines and some part of the energy is propagated through air and some through the dielectric substrate material, it does not feature pure TEM mode characteristics. Still, quasi TEM mode wave propagation can be assumed in good approximation [55] so that a valid solution can be obtained from the telegrapher's equation and the wave propagation can be described by the propagation constant γ. For quasi-TEM mode waves in the regarded frequency range, the propagation behavior of the wave is described by the wave's amplitude and phase as follows (2-20):

$$A_0 = A_x e^{-\gamma x} = A_x e^{-(\alpha + j\beta x)} \tag{2-20}$$

, where α is the attenuation constant, β the phase constant, x the position in the direction of propagation and A_0 the amplitude of the input signal. In the concept of effective permittivity, the goal is to find the equivalent dielectric constant of a line completely embedded in a single dielectric material. The model concept is depicted in Fig. 2-14. This is an effective way to be able to derive the propagation constant of a propagated wave. It can be demonstrated, that the phase constant is related to the effective permittivity of the transmission line as follows [55]:

$$\beta = \frac{2\pi}{\lambda} = \frac{2\pi f \sqrt{\varepsilon'_{eff}}}{c_0} \tag{2-21}$$

Here, c_0 is the speed of light in free space and ε'_{eff} is the effective dielectric constant of the microstrip line taking into account the dielectric constants of all materials involved as

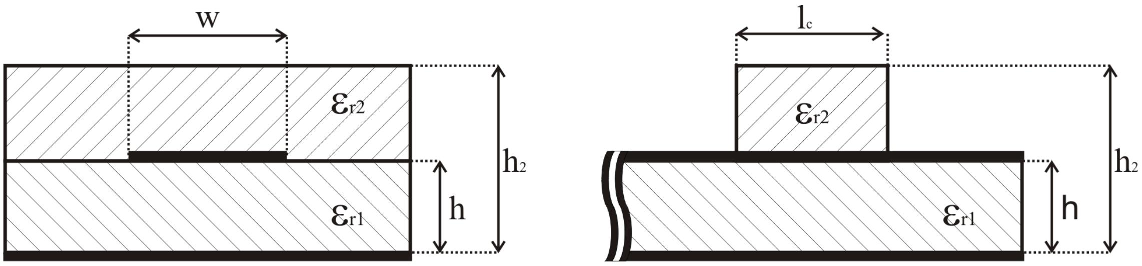

Figure 2-15: *Microstrip with substrate permittivity ε_{r1} and cover permittivity ε_{r2}.*

well as the line geometry. In the setup sketched in Fig. 2-15 a part of the line with the length of l_c is covered by a certain material with a dielectric constant of ε_{r2} instead of air. The substrate dielectric constant is ε_{r1}.

This kind of microstrip geometry can be characterized via its overall effective dielectric constant. The real part of it can be extracted from phase measurements using the following equation:

$$\varphi = \beta l = \frac{2\pi f \sqrt{\varepsilon'_{eff}}}{c_0} l_c \tag{2-22}$$

Knowing the line length l_c, it is possible to determine the real part of the effective permittivity. To gain information on the properties of the material covering the microstrip, it is required to correlate the dielectric constant of the material with the effective dielectric constant of the line. With the help of conformal mapping [56], [57], the following equation was derived in [58] based on certain geometrical simplifications.

$$\varepsilon_{eff} = \varepsilon_{r1} q_1 + \varepsilon_{r2} \frac{(1-q_1)^2}{\varepsilon_{r2}(1-q_1-q_2)+q_2} \tag{2-23}$$

, where q_1 and q_2 are filling factors depending on the line geometry which can be calculated using Wheeler's transformation [56]. The effective dielectric constant in (2-23) turns complex when either of the materials, the substrate or the cover, is complex. The resulting equations also reported in [58] are leading to a discrepancy of less than 2% compared to other approaches [59], [60], [61]. This provides a closed form solution to extract the real part of a material´s permittivity from phase characterization of microstrip line signals. This equation is valid for the physical setup depicted in Fig. 2-15. The filling factors are depending on both: the microfluidic channel and microstrip dimensions. Applying Wheeler's transformation for a wide microstrip line ($w/h \geq 1$), the filling factors can be calculated with the following equations:

$$q_1 = 1 - \frac{1}{2} \frac{\ln\left(\frac{\pi}{h} w_{eff-1}\right)}{\frac{w_{eff}}{h}} \tag{2-24}$$

$$q_2 = 1 - q_1 - \frac{1}{2} \frac{h - v_e}{w_{eff}} \ln\left[\pi \frac{w_{eff}}{h} \frac{\cos\frac{v_e \pi}{2h}}{\pi\left(\frac{h_2}{h} - \frac{1}{2}\right) + \frac{v_e \pi}{2h}} + \sin\frac{v_e \pi}{2h}\right] \tag{2-25}$$

$$w_{eff} = w + \frac{2h}{\pi} \ln\left[17.08\left(\frac{w}{2h} + 0.92\right)\right] \tag{2-26}$$

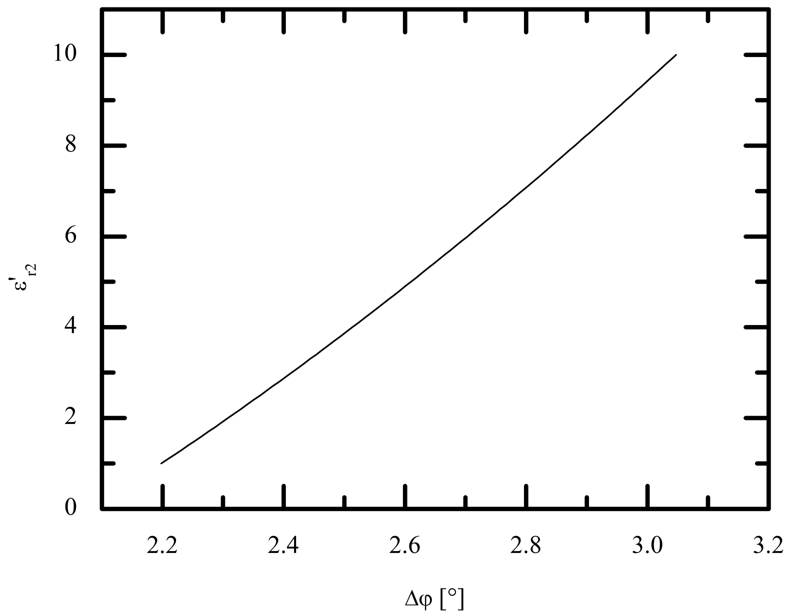

Figure 2-16: *Real part of the MUT permittivity versus phase difference at 120 GHz signal frequency.*

$$v_e = \frac{2h}{\pi} \arctan\left[\frac{\pi}{\frac{\pi w_{eff}}{2h} - 2}\left(\frac{h_2}{h} - 1\right)\right] \tag{2-27}$$

The variables in these equations, which are entirely based on geometrical properties, are depicted in Fig. 2-13. That means for a precisely build transmission line setup, the real part of the effective dielectric constant can be determined via phase measurements and correlated to the material's permittivity as follows:

$$\varepsilon_{r2} = \frac{q_2\left(\varepsilon_{eff} - \varepsilon_{r1} q_1\right)}{(1 - q_1)^2 + (q_1 + q_2 - 1)\left(\varepsilon_{eff} - \varepsilon_{r1} q_1\right)} \tag{2-28}$$

, where the real part of ε_{eff} can be written as:

$$\varepsilon'_{eff} = \left(\frac{\varphi c_0}{2\pi f l_c}\right)^2 \tag{2-29}$$

Considering the target BiCMOS process, the parameters for a 50 Ω microstrip line are: $\varepsilon_{r1} = 4.1$, $h = 9.83\,\mu$m and $w = 16\,\mu$m. The material on top of the line is considered to have a square shaped geometry exhibiting a 500 µm × 500 µm cross section, since these are the target sample dimensions. The resulting filling factors are: $q_1 = 0.685$ and $q_2 = 0.2523$. With these parameters, the correlation between the permittivity and the signals' phase difference can be calculated. The result for 120 GHz operation can be used to extract the real part of an MUT permittivity and is depicted in Fig. 2-16. The considered permittivity range has been chosen from 1-10, to cover all of the relevant materials at 120 GHz from air to aqueous solutions like water ($\varepsilon'_r \approx 7$) [62]. Fig. 2-16 reveals that the phase differences in the regarded permittivity range from 1-10 are less than 1° for the discussed scenario. To perform highly accurate phase measurements and simultaneously

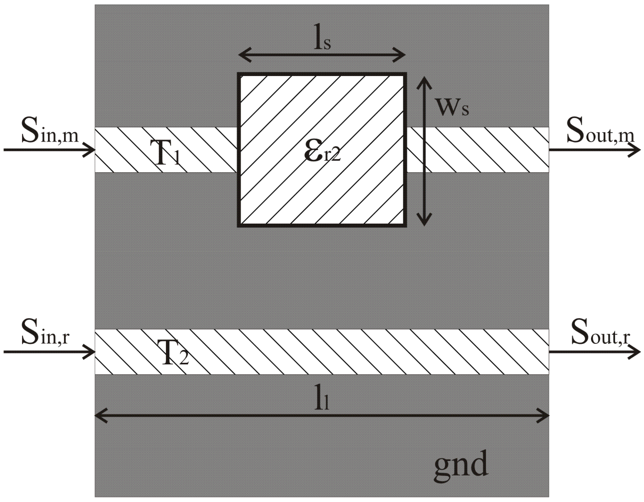

Figure 2-17: *Microstrip line pair for reference based phase detection.*

eliminate influences of process variations or temperature, a simple transmission line with the same length can be used as reference in parallel to the sensor line. The setting is sketched in Fig. 2-17. The input signals $S_{in,m}$ (measurement) and $S_{in,r}$ (reference) are in phase, thus the phase difference of the two output signals $S_{out,m}$ and $S_{out,r}$ is evoked by the MUT covering the measurement line and can be derived using the following equation [63]:

$$\Delta\varphi = 360° \frac{\sqrt{\varepsilon'_{eff,covered}} - \sqrt{\varepsilon'_{eff,uncovered}}}{\lambda_0} l_s \tag{2-30}$$

Here, $\varepsilon'_{eff,covered}$ is the real part of the effective dielectric constant for a covered line and $\varepsilon'_{eff,uncovered}$ of the pure microstrip. The latter can be calculated using the following equation for standard microstrips [55].

$$\varepsilon_{eff,uncovered} = \frac{\varepsilon_{r1} + 1}{2} + \frac{\varepsilon_{r1} - 1}{2} \frac{1}{\sqrt{1 + 12h/w}} \tag{2-31}$$

Measuring the phase difference between a signal conducted by a covered microstrip compared to a not covered one enables extraction of the effective dielectric constant of materials covering the line using the phase-permittivity dependency derived earlier in this section. The exploitation of these relations for permittivity characterization in phase-sensitive bio sensors is explained in section 3.3.

When complex dieletric measurements are required, the attenuation of the microstrip must be considered and evaluated. As presented in [64] it can be derived with the following equation:

$$\alpha = 8.686k \left[\frac{\varepsilon'_{eff}}{2} \sqrt{1 + \tan^2\delta} - 1 \right]^{1/2} dB/m \tag{2-32}$$

Here, k is the free space phase constant and $\tan\delta$ is the loss tangent:

$$\tan\delta = \frac{\varepsilon''_{eff}}{\varepsilon'_{eff}} \tag{2-33}$$

(2-33) and (2-32) show that the line attenuation depends on both real (ε'_{eff}) and imaginary part (ε''_{eff}) of the materials' permittivity. In [65] a method is presented how moisture content can be detected by making use of the attenuation characterization. The measured attenuation of the covered microstrip is evaluated to attain the complex dielectric constant.

Another important parameter that can be exploited for dielectric measurements is the characteristic impedance of the line. It is changed by variation of the cover material and can be correlated to the effective permittivity as follows [55]:

$$Z_0 = \frac{120\pi}{\sqrt{\varepsilon_{eff}}[\frac{w}{h} + 1.393 + 0.667\ln(\frac{w}{d} + 1.444)]} \tag{2-34}$$

Hence, the effective permittivity and thus the material's dielectric constant can also be obtained by determining the characteristic impedance of the microstrip.

In the case of integrated transmission lines, the thickness t of the conductor can be higher so it might become relevant for the line characteristics. In the target process, the conductor is 3 µm thick, which is in the same order of magnitude as the distance of the conductor to the ground plane (h). The effect was studied by many researchers [45, 57, 66–68]. The finite thickness of a conductor effects both the characteristic impedance and the effective dielectric constant. Closed form expressions have been derived in [66] based on highly accurate equations presented in [45] by introducing the effect of t/h. Bahl et al. modified the correctional terms presented in [57] and [67] yielding the following set of equations:

$$\begin{aligned}
Z_0 &= \frac{120\pi}{\sqrt{\varepsilon_{r,eff}}}\left[\frac{W_e}{h} + 1.393 + 0.667\ln\left(\frac{W_e}{h} + 1.444\right)\right]^{-1} \\
\frac{W_e}{h} &= \frac{W}{h} + \frac{1.25}{\pi}\frac{t}{h}\left(1 + \ln\frac{2h}{t}\right) \\
\varepsilon_{r,eff} &= \frac{\varepsilon_r + 1}{2} + \frac{\varepsilon_r - 1}{2}\left(1 + \frac{12}{W/h}\right)^{-1/2} - C \\
C &= \frac{\varepsilon_r - 1}{4.6}\frac{t/h}{\sqrt{W/h}}
\end{aligned} \tag{2-35}$$

In (2-35), W_e is the effective line width taking into account the conductor's thickness and C is a correctional term. Further classification of these equations for different W/h values, what is commonly done for this type of equations, is omitted here, since for all the microstrip lines considered and designed in the frame of this thesis $W/h > 1$ holds. Using these equations and parameters from the target process, it is possible to compare the influence of the thickness on $\varepsilon_{r,eff}$ and Z_0. The effective permittivity is hardly affected and changes by 0.03 % to 3.085. There is a much higher impact onto the characteristic impedance. Without taking the thickness into account, the impedance is $Z_0 = 56.94\,\Omega$. When (2-35) is applied, this drops to $Z_0 = 49.58\,\Omega$. The chosen value of the conductor width was obtained by EM simulations so it is clear that the more accurate set of equations (2-35) yields the value closer to $Z_0 = 50\,\Omega$. The design procedure will be discussed in chapter 6. These results show that for certain types of microstrip sensors, where the input impedance plays a substantial role, the conductor thickness needs to be considered. Since the calculated effective permittivity is basically unchanged when t is considered, transmission line sensing based on phase and attenuation measurements can accurately

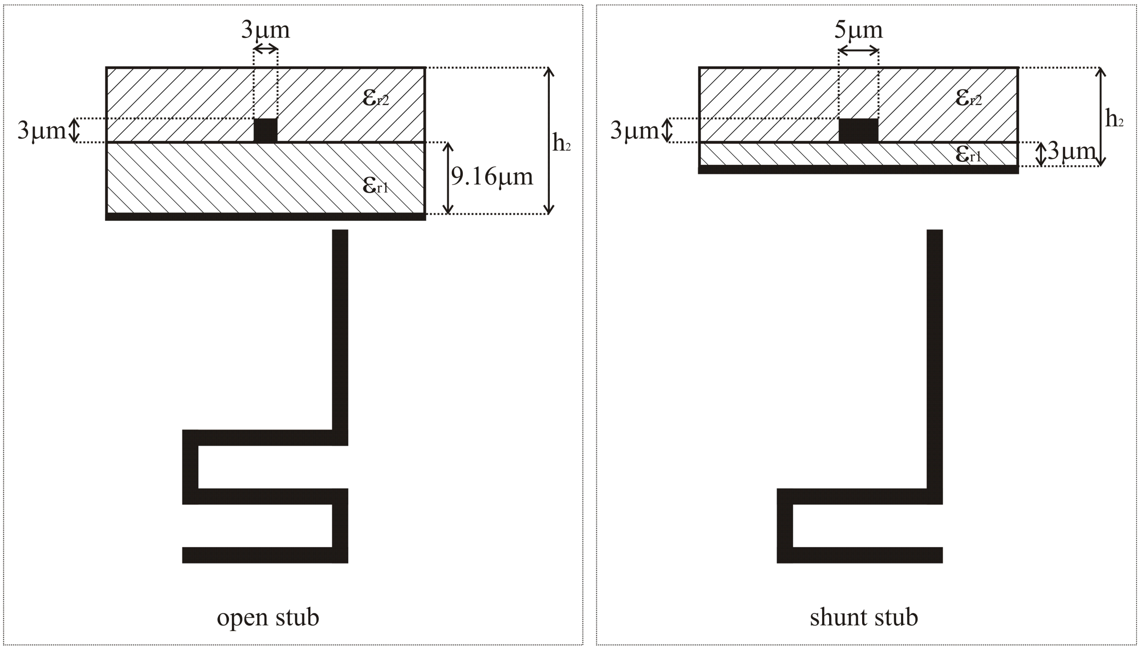

Figure 2-18: *Layout and cross section of open and shunt stubs as microstrip lines [8].*

be conducted without it. Further mitigation of the impact of a conductor's thickness is obtained by applying a differential sensing approach displayed in Fig. 2-17.

Fig. 2-18 shows two line examples featuring either capacitive or inductive behavior depending on the operational frequency. To emphasize the effect of a change in characteristic impedance, the microstrip is used in a lambda fourth stubline and a resonant circuit is obtained. The parameter h_2 in Fig. 2-18 varies with the volume of the MUT that is put on top of the line. This behavior was investigated and presented in [8], where these lines are connected to oscillators as reactive elements. The oscillator can be regarded as a read-out circuit. This is discussed further in 3.1. The input admittance of the open stub line considering line losses can be described as follows:

$$Y = Y_0 \tanh(\gamma l) = Y_0 \tanh((\alpha + j\beta)l) \tag{2-36}$$

Resonance occurs, when the imaginary part of the admittance, the susceptance, is zero. This is depicted in Fig. 2-19. The transition frequency at which the characteristic changes from capacitive to inductive behavior, is depending on the effective permittivity of the line and with that on the MUT permittivity.

The intended oscillator circuit for read-out demands the stub to show capacitive behavior to maintain oscillation. Hence, the stub sensor needs to be designed for a certain permittivity range with respect to the oscillator performance. That means, it is restricted to a certain range of permittivity. This will be discussed further in chapter 3.

2.5 Summary

The presented and discussed methods for dielectric characterization of samples are all suitable for the target applications ranging from cytometry to food quality control based

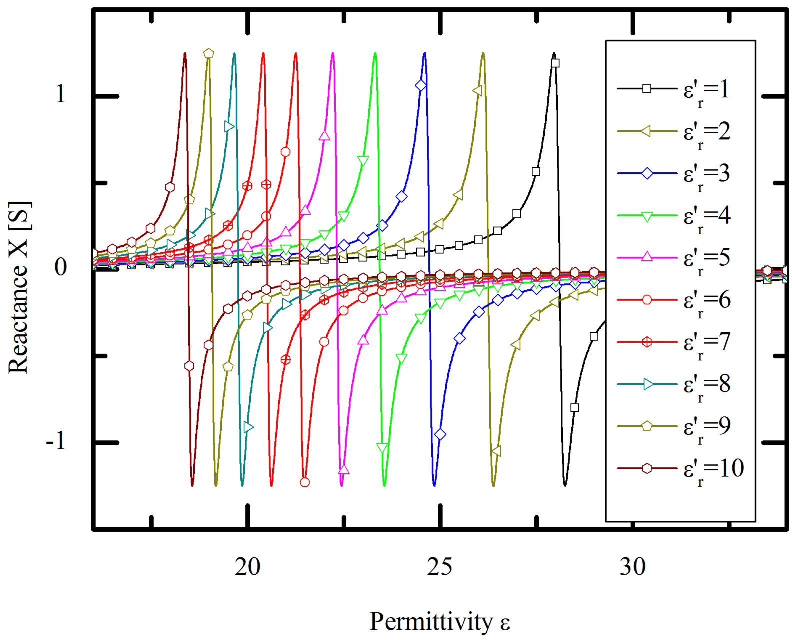

Figure 2-19: *Input characteristics of open- and shunt-stub versus frequency for different dielectric superstrates [11].*

on water content. They have been chosen for consideration based on their applicability to contactless determination of dielectric sample properties since that feature is substantial in both medical and bio sensing application to avoid contamination. Comparison of their performance concerning accuracy, resolution and complexity of the respective sensing approach can only be done in combination with the respective read-out approach. However, at first, benchmarking can be done based on their basic physical properties as a standalone sensor. The patch antenna method requires the biggest sensing area and hence the highest sample volume. This is disadvantageous in biomedical applications where only little sample volumes are available. Further scaling to higher frequencies can provide a remedy to that issue. Additionally, the large effective area of the device interacting with the MUT makes it sensitive to malfunction because of potentially lossy MUTs. All of the target applications are dealing with water as a carrier liquid or at least a considerable ingredient in the samples. Experiments using an interferometer at millimeter-wave frequencies and above, along with theoretical investigations on the dielectric constant, will be presented in chapter 5. It will be demonstrated that the imaginary part is even higher than the real part for frequencies above the relaxation frequency of the material, meaning that loss is becoming a considerable factor.

Open-ended coaxial detection is a very promising method since the cross section of the screened material under test is maximized compared to the other approaches owing to its field distribution at the open end of the coaxial line. Moreover, data extraction is generally based on network theory and well understood and studied S-parameter measurements as well as deembedding techniques that have been widely reported and documented. For that reason, it is also used for commercially available dielectric measurement kits. Nevertheless, read-out circuits can become quite complex, depending on the accuracy and resolution needed in the respective application. Regarding accuracy and resolution, VNAs are the perfect candidate . However, they are very expensive and quite bulky laboratory equipment that is only relevant for testing and not considered for the final sensor system. Examples of integrated single chip VNAs can be found in the literature. The method will be evaluated and considered within this thesis and further discussions on the topic will be presented in chapter 3.

The transmission line approach is a straightforward sensing approach, since models are well known and documented in literature. Furthermore, transmission line sensing bears the potential of easy permittivity extraction using analytical methods discussed in this chapter that have been tested experimentally. In addition to that, transmission line designs exhibit the lowest design complexity for the sensor itself. However, read-out circuits can also prove to be complex and to some extent power hungry. The sensitivity is also limited compared to transmission and reflection based methods as well as resonant approaches based on the sample geometry and position. The strong advantage of linear phase behavior towards changes in the real part of an MUT motivates to develop a system that applies a microstrip sensor in a resonant, differential setup. This system can be implemented as an interferometer which is one of the read-out approaches that will be presented in chapter 3.

The sensing methods in this chapter have all been investigated both through literature and experimentally. The definitive choice of the final sensor structure along with respective read-out strategies will be discussed in chapter 3.

3 Read-out Circuits for Dielectric Sensors

The sensors presented in chapter 2 serve as a detector sensing the permittivity of a material as the physical quantity of interest. A distinct parameter is changed based on material properties. To benefit from that, it is necessary to characterize, extract and evaluate the parameter used as the indicator in the particular case. Moreover, those sensors exhibit a limited sensitivity which can be enhanced by using resonance for example. Here, sensitivity is gained by an increased conversion factor from one physical quantity to another in proximity to the resonant frequency. Different sensing methods often require an individual approach to interpret the sensor's response, entailing certain advantages and drawbacks that need to be investigated for choosing the appropriate tool suiting the target application best. The following sections demonstrate and discuss the considered read-out techniques to finally identify the optimum approach for permittivity-based characterization of dielectric materials in biomedical contexts.

3.1 Tuned Oscillator

The first circuit that is discussed is an oscillator, which is transposing a change of impedance to a shift of the resonance frequency. Therefore, it is applicable to all sensors changing the impedance as a response to permittivity variations of an MUT. A frequently applied circuit is a Colpitts type oscillator shown in Fig. 3-1. The circuit depicted on the left

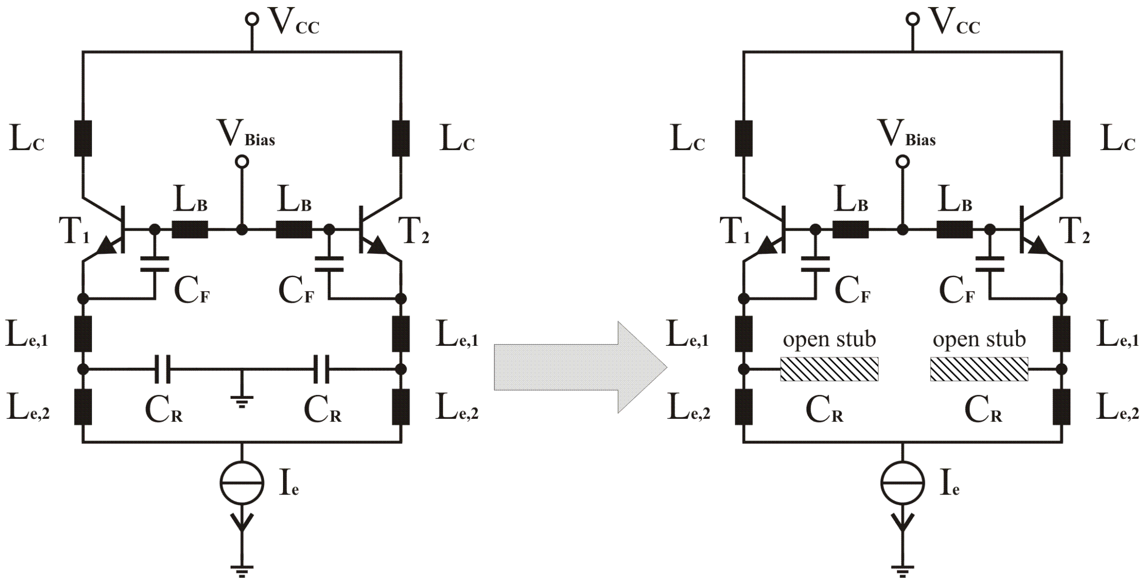

Figure 3-1: *Schematic of the differential Colpitts oscillator (left) and stub line placement (right).*

side in Fig. 3-1 is basically a differential common collector Colpitts oscillator featuring additional components for improved performance as explained in the following.

The differential nature of the investigated topology provides several advantages. Noise generated on chip is substantially reduced compared to a single ended circuit [69]. Regarding high-frequency grounding and decoupling of supply and bias voltages, differential circuits are preferable due to the virtual ground nodes [70].

The Colpitts architecture potentially has a high frequency tuning range. As explained later in this chapter, this results in a higher sensitivity for the presented approach. Additionally, it features a moderate to high loaded Q factor and good isolation, due to self-buffered operation stemming from the common collector topology [71]. The frequency of oscillation of this kind of oscillator depends on the effective capacitance that is active at the nodes of the transistor according to (3-1) [72]:

$$\omega_{osc} = \frac{1}{\sqrt{LC_{eff}}} \tag{3-1}$$

The parasitic capacitance of the transistor as well as the reactive elements active at the emitter node are contributing to the effective capacitance C_{eff}. It can be calculated with the help of (3-2) [72]:

$$C_{eff} = C_{bc} + \frac{(C_{be} + C_F)C_{equ}}{C_{equ} + C_{be} + C_F} \tag{3-2}$$

In (3-2), C_F is the feedback capacitance depicted in Fig. 3-1, C_{be} and C_{bc} are the parasitic capacitances of the bipolar transistor. The mentioned capacitors are either defined by the respective transistor dimensions and bias points or their value is simply chosen by design. The equivalent capacitance C_{equ} is accumulated by all reactive elements effective at the emitter node of the transistor. From standard circuit theory, this can be calculated for the circuit shown on the right in Fig. 3-1 according to (3-3):

$$C_{equ} = \frac{1}{\omega^2(\frac{1}{\omega^2 C_R - 1/L_{e2}} - L_{e1})} \tag{3-3}$$

The circuit depicted on the right in Fig. 3-1 shows the position of the sensing stub lines. The component C_R in the left schematic in Fig. 3-1 is the capacitive element that is substituted by the stub lines. The imaginary part of their input admittance is affecting the oscillation frequency of the oscillator so that the oscillation frequency can be used as a measure for the admittance and, applying the appropriate model, the MUT permittivity accordingly.

The sensing method based on stub lines presented in 2.4 is compatible with this kind of read-out strategy. The stub line can function as a reactive element in the tank, as depicted in Fig. 3-1, affecting the frequency of oscillation according to its input admittance. It can be calculated with the help of (2-34) and (2-36). The phase constant β is correlated to the effective permittivity which again contains the MUT permittivity according to (2-29). Using this set of equations, the real part of an MUT permittivity can be extracted from the oscillation frequency which can be measured with a very high accuracy.

The dimensioning of the circuit elements needs to be designed to ensure that the stub line shows capacitive behavior at the designated resonance frequency to obtain oscillation. Hence, a negative imaginary part of the impedance is required.

The described method was implemented at 27 GHz in a 130 nm SiGe process as reported in [8]. The experimental measurement setup is depicted in Fig. 3-2. The displayed

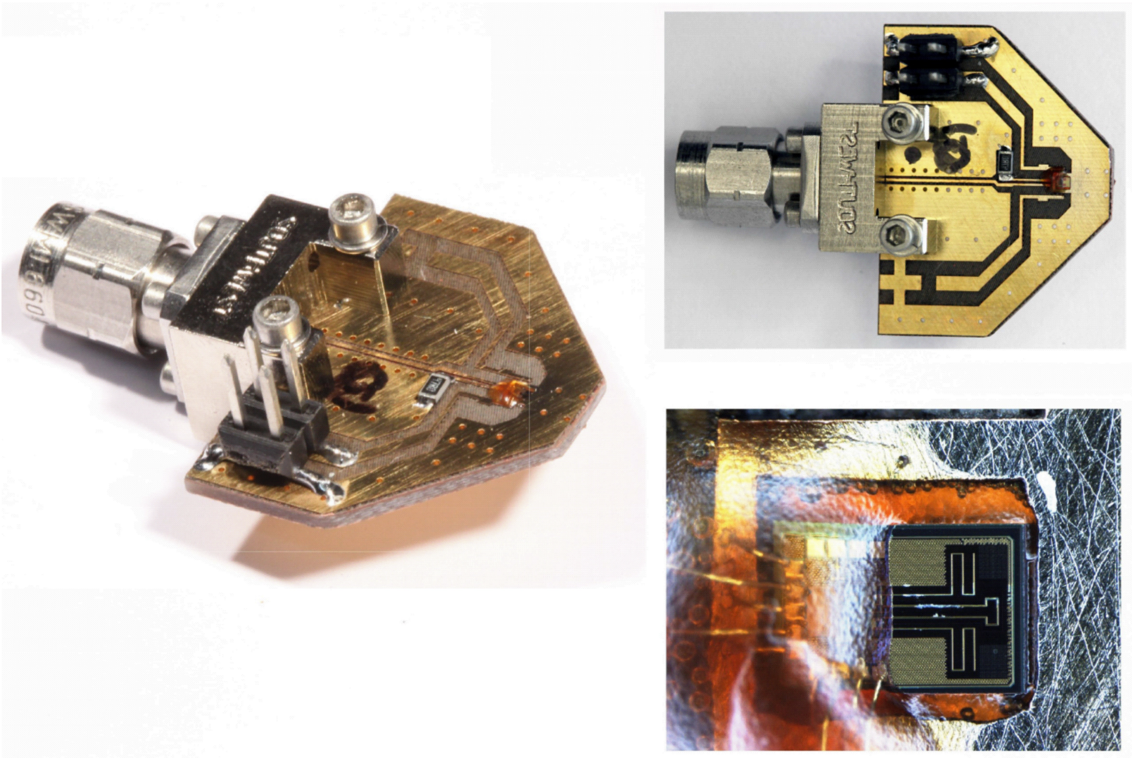

Figure 3-2: *VCO based sensor protected by glue and test PCB [8].*

arrangement was applied for test measurements using reference samples like ethanol, methanol and water to characterize the sensor response to MUTs exhibiting various dielectric properties. The graphs in Fig. 3-3 compare the simulated and measured results. Fig. 3-3a shows the change in oscillation frequency and Fig. 3-3b changes in output power for different liquid samples. The results are presented with respect to the sensor output signals for a bare sensor, thus, the sensing lines are exposed to air. Both the power as well as the frequency of oscillation provide information onto the sample permittivity, one on the real and the other on the imaginary part.

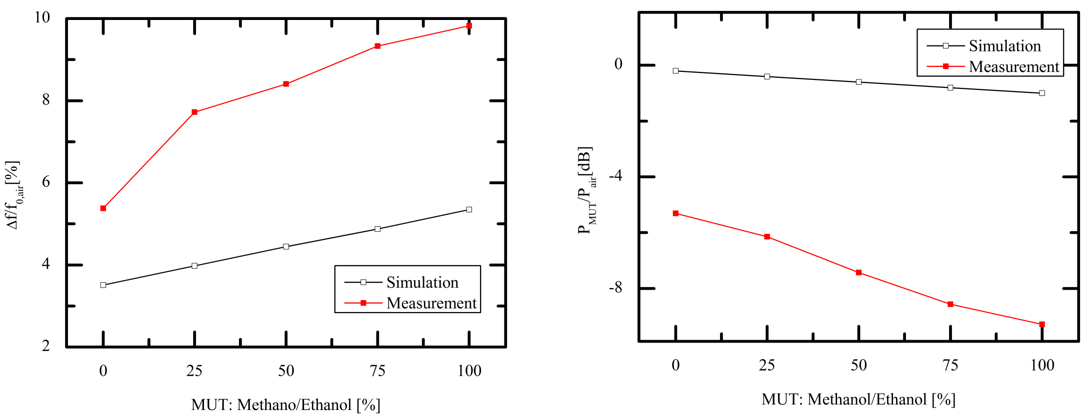

(a) *Oscillation frequency change.*

(b) *VCO output power change.*

Figure 3-3: *VCO based sensor: Measurement versus simulation results for changing mixing ratio: Methanol/ethanol [8].*

The sample for testing was composed of methanol and ethanol in different concentrations, to synthesize a mixture with adjustable dielectric values. The lower x-coordinates in the graphs displayed in Fig. 3-3 show the concentration of methanol in ethanol, so that the MUT ranges from pure ethanol to pure methanol. The corresponding values of permittivity and loss tangent are on the upper x-coordinates, respectively. The experiments show that both the measured output power and frequency exhibit stronger changes than expected based on the simulation results. The oscillation frequency is changed by almost 5 % and the output power by approximately 4 dB.

Tuned oscillators can also be applied to interact with other reactive elements. In [33] a CMOS cross-coupled oscillator operating at around 12 GHz is used along with an IDC element to detect the concentration of particle suspensions. The principle is the same, tuning the resonance frequency with the reactive sensing structure based on dielectric properties of an MUT. The circuit is depicted in Fig. 3-4. The oscillation frequency

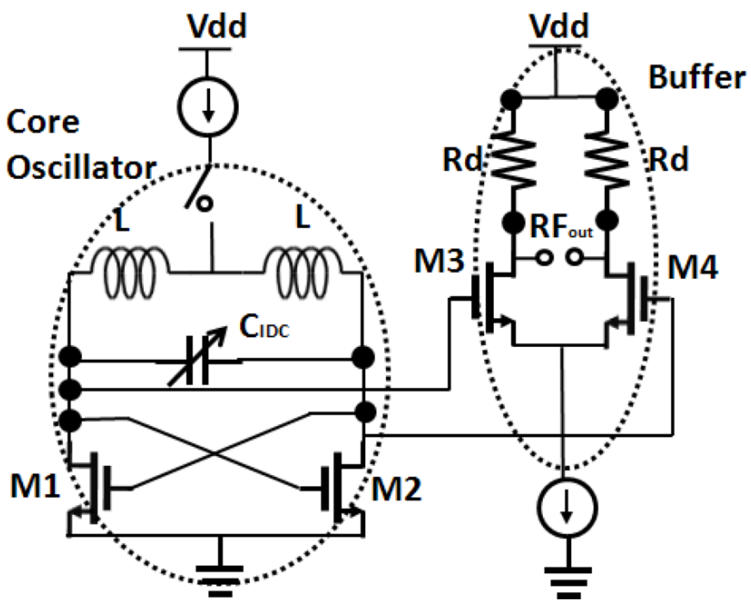

Figure 3-4: *Schematic of the cross-coupled CMOS oscillator [33].*

depends on the IDC capacitance according to the following equation.

$$f = \frac{1}{2\pi\sqrt{LC_{total}}} \tag{3-4}$$

L is the accumulated inductance of all inductors depicted in Fig. 3-4 and C_{total} is the IDC capacitance plus parasitic capacitances of the active devices building the oscillator. The overall capacitance can be found to be:

$$C_{total} = C_{IDC} + C_{parasitics} \tag{3-5}$$

The correlation of the IDC capacitance to the dielectric constant of the MUT was discussed in section 2.1. To investigate the sensor's response to different dielectric samples, in [33] the sensor was implemented in a 130 nm SiGe BiCMOS process and tested with isopropanol, methanol, ethanol and acetone. The results are displayed in Fig. 3-5.

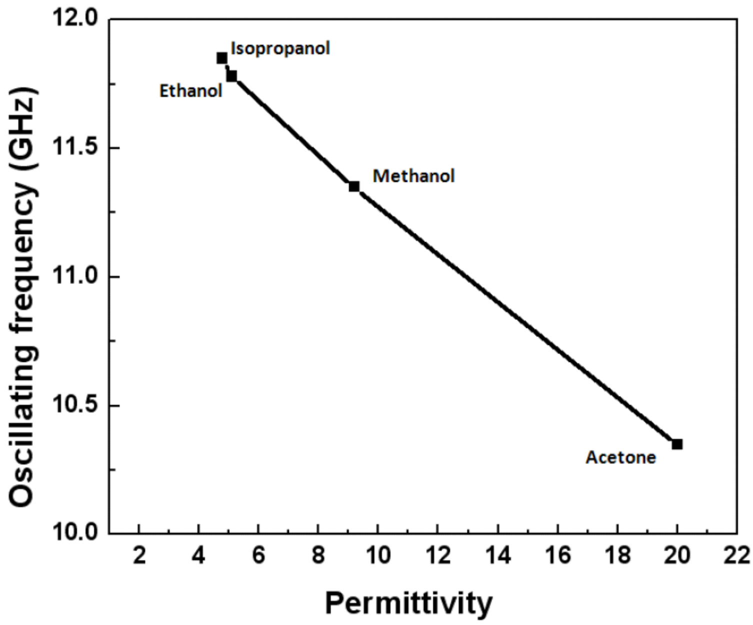

Figure 3-5: *Measured oscillation frequency versus permittivity ε for different calibration fluids [33].*

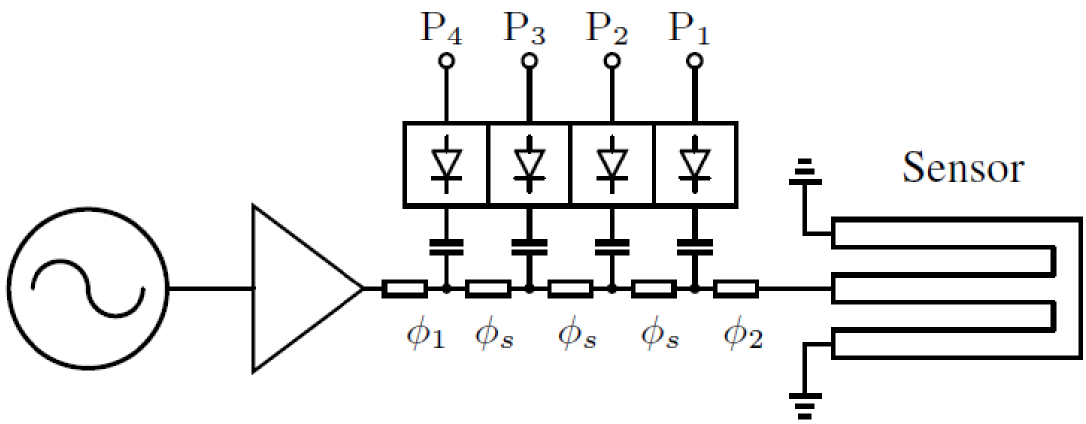

Figure 3-6: *Sampled-line reflectometer topology [73].*

The real part of the permittivity could approximately be tuned from 5-20 by using those fluids and, as depicted in Fig. 3-5, it caused the center frequency to shift about 100 MHz/*unit*.

To evaluate and discuss these results, the other approaches considered in this thesis need to be investigated and finally compared to each other to settle on the finite choice for a read-out along with the proper sensing method. The following subsection discusses the more generic ones of the presented read-outs, the VNA and reflectometer circuits.

3.2 Reflectometer and VNA

Both methods discussed in this section can be applied to all sensors changing either their impedance or their transmission-reflection characteristics, which is usually associated with each other. All sensors discussed in this thesis could be characterized by the VNA approach. The reflectometer can only work with sensors having a single input port. In [73] the read-out consists of a multi-probe reflectometer with an on-chip voltage-controlled oscillator (VCO) as signal source. Further components are a buffer, a capacitive coupled line, and four power detectors. The applied method is a sampled line principle from [74] and the dielectric sensor is a shorted coplanar waveguide. The topology is depicted in Fig. 3-6.

When the impedance of the waveguide changes, mismatch occurs at the input port causing reflections and a standing wave pattern emerges, recorded by the four power detectors. The sensor was tested with binary methanol-ethanol mixtures exhibiting different permittivities. The extracted phase is depicted in Fig. 3-7.

The investigations indicated that the sensor possesses a resolution of at least $\varepsilon' = 0.0125$ and the phase changes more than 30° for methanol and ethanol measurements implying a change in the real part of the dielectric constant from 2 to 4.2 at 125 GHz. The main advantage of the reflectometer is its flexibility so it is capable to read out any sensor having a single wave port. When further information about a sensor response is desired, a more sophisticated approach must be used based on the concept of vector network measurements. Fig. 3-8 features the block diagram of the single- and dual-port VNA chips presented in [75]. The single chips include a reference receiver module and a reflection receiver module each. A third receiver module enables measurement of transmission parameters. Passive wide band balun structures are used at the interface between the differential blocks and the single-ended directive elements and LNAs. The depicted system is capable to perform two port measurements from 50-100 GHz characterizing reflections and transmissions from a sensor being the device under test (DUT). The comparison conducted in [75] between the non-coherent reflectometer approach and a coherent detection

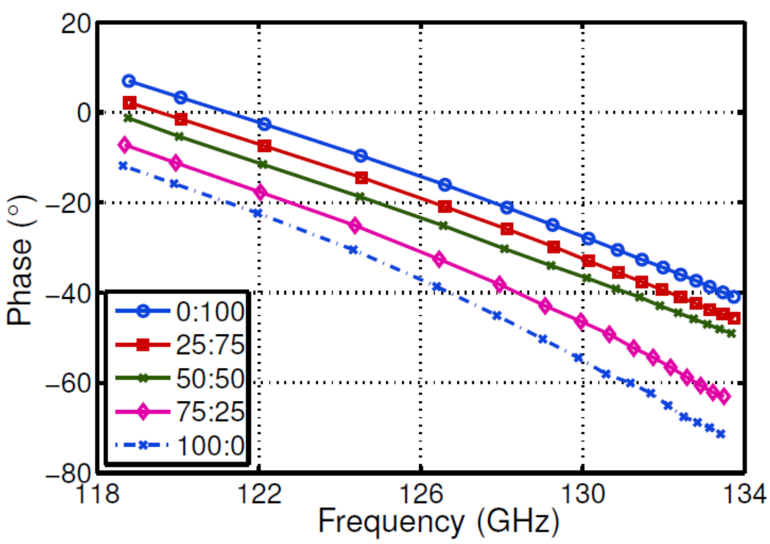

Figure 3-7: *Example of reflectometer phase measurements [73].*

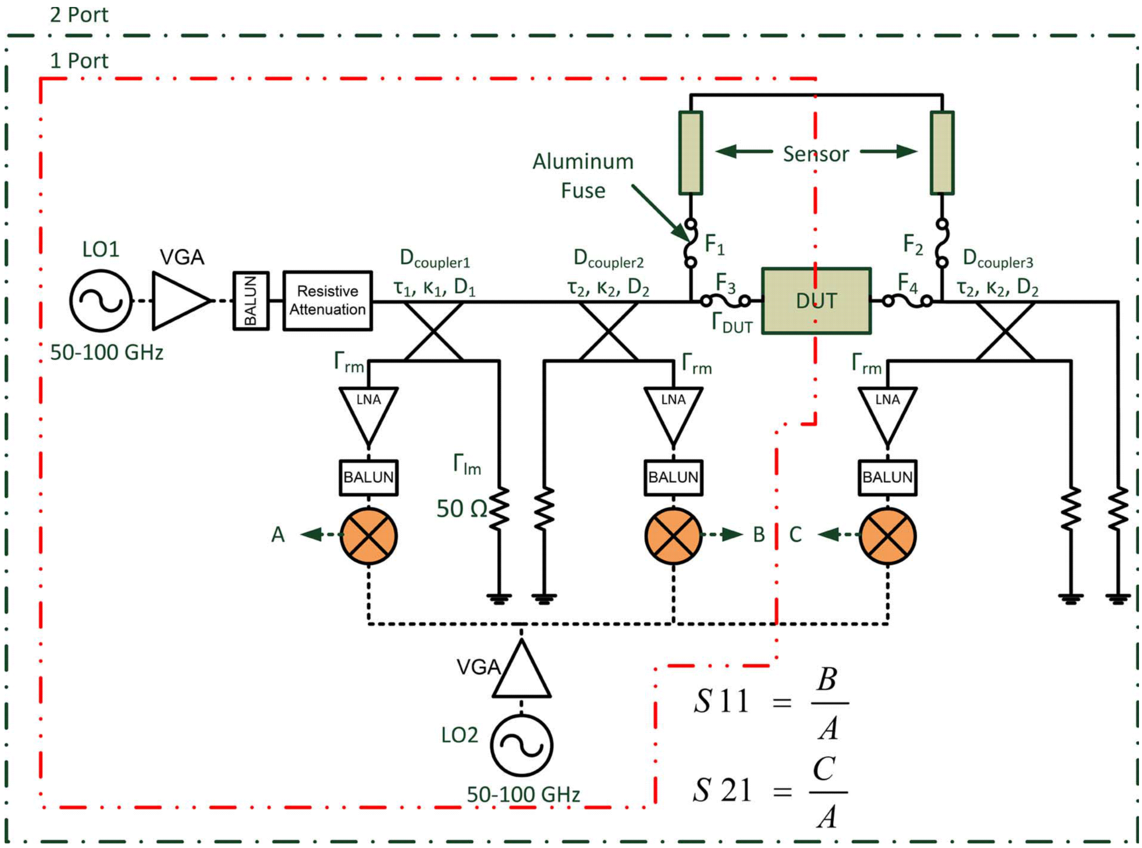

Figure 3-8: *Block diagram of an integrated VNA [75].*

technique show that the coherent detection offers the best dynamic range at the expense of increased circuit complexity, also evident from Figs. 3-6 and 3-8. The results obtained using that system were compared to measurements performed with a commercial VNA. The measured component is a V-band horn antenna connected to a waveguide to coaxial adapter. Both results are depicted in Fig. 3-9. The figure shows clearly that the results are very similar to each other. Phase measurements have been performed with binary solutions in [75]. Fig. 3-10 displays the phase versus frequency for 5 different samples. The sensing element is a 1.2 mm long microstrip transmission line sensor that was immersed in the fluids. It is indicating high sensitivity of that sensing approach. It means that this approach is well suited for high accuracy sample characterization when the consumed DC power and complexity are of less importance. For portable devices, this might become an issue and lower power systems are preferable.

3.3 Interferometer

When marginal changes in the composition of a material must be detected, one efficient way to increase a sensor's response is to measure in parallel, comparing the sensing path to a reference path. This approach using parallel microstrip sensors has been presented in section 2.4. The structure depicted in Fig. 2-17 compares the transmission of a microstrip that is partially covered by the MUT to a not-covered one.

The principle of the chosen technique is depicted in Fig. 3-11a. To be able to compare

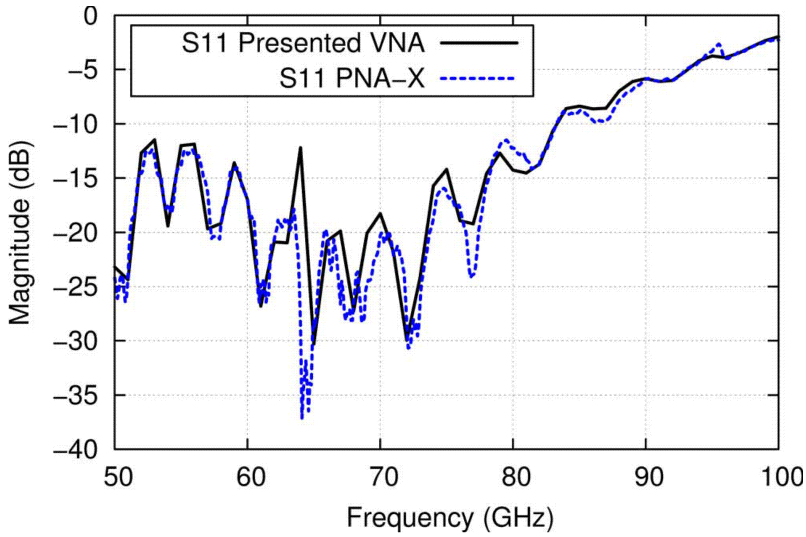

Figure 3-9: *Measured magnitude of the input reflection coefficient of a V-band horn antenna connected to a waveguide to coaxial adapter using the presented VNA and a commercial VNA (PNA-X) [75].*

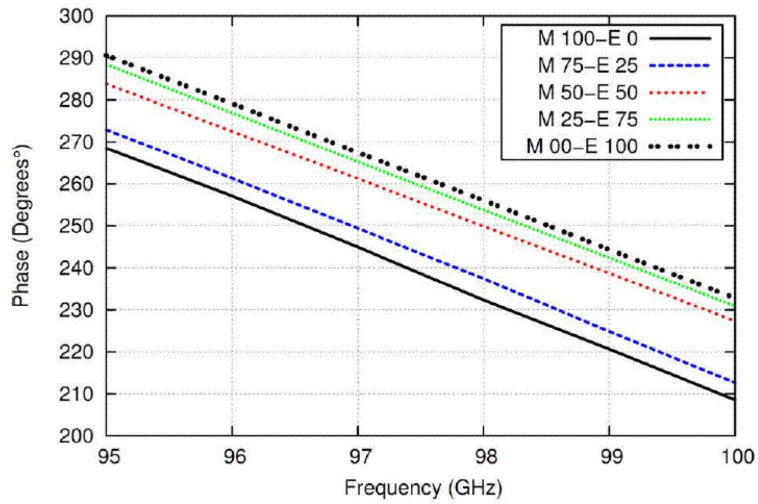

Figure 3-10: *Measured phase of the transmission parameter of binary methanol-ethanol solutions [75].*

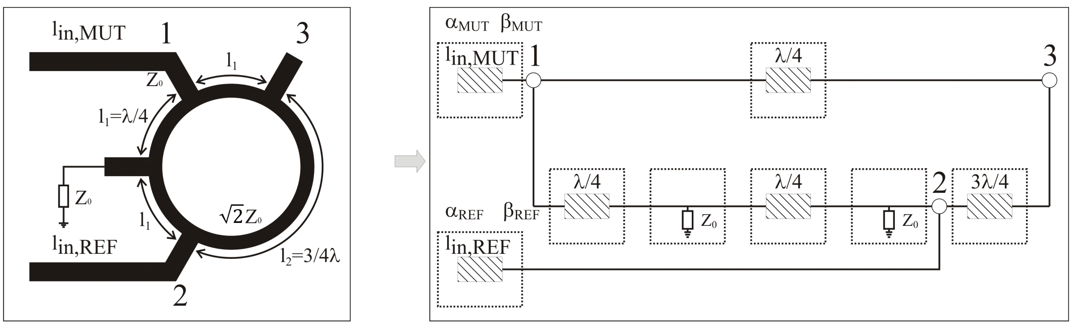

(a) *Hybrid ring coupler layout.* (b) *Hybrid ring coupler: Network of line sections.*

Figure 3-11: *2-port based line model used for Matlab coding of the hybrid ring coupler function.*

both line's transfer characteristics, the excitation must be identical in amplitude and phase, which is assumed to be the case in the following considerations. Finally, this will be accomplished using a Wilkinson power splitter, providing two identical signals from a single source. The comparison between the transmissions of the two lines is realized by a hybrid ring coupler. This method, applied in [76], is increasing the sensitivity of a simple microstrip sensor as explained in the following. The lines, reference ($l_{in,REF}$) and measurement ($l_{in,MUT}$) microstrip line, ideally propagate signals equal in phase and amplitude for an unloaded sensor. The signal of the sensing microstrip is altered by an MUT according to its dielectric properties. In section 2.4 it was shown that this effect is small so that both signals are still quite similar to each other. The hybrid ring coupler superimposes both signals at its delta port, port 3 in Fig. 3-11. Both signals have a phase difference evoked by the path length difference which, for the center frequency, is equivalent to half of the wavelength. For identical signals, this amounts to 180° and both signals cancel each other. Small differences in phase and magnitude will change the hybrid ring coupler output according to its transfer function. The phase difference of measurement and reference signal is 180° only at the designated center frequency making the device narrow band. This is the key feature making the overall concept more sensitive to marginal changes in the sensed signal.

At the output of the hybrid (port 3), the phase conditions of the two output signals, which are superimposed, is described as follows:

$$\begin{aligned}\Delta\varphi_{out} &= \varphi_2 - \varphi_1\\ \varphi_1 &= \varphi_{0,1} + \beta_{rat} l_{\lambda/4}\\ \varphi_2 &= \varphi_{0,2} + 3\beta_{rat} l_{\lambda/4}\end{aligned} \tag{3-6}$$

$\varphi_{0,1}$ and $\varphi_{0,2}$ are the initial phase conditions of the signals entering the hybrid ring coupler at port 1 and port 2. β_{rat} is the phase constant of the lines composing the hybrid. $\varphi_{0,1}$ contains the information about the phase shift evoked by the particular sample on top of the line. Hence, the difference in $\varphi_{0,1}$ and $\varphi_{0,2}$ is caused by the MUT. The equations that have been introduced in section 2.4 relating the phase constant β to the real part of the effective permittivity together with the condition of $\Delta\varphi = 180° \equiv 2\pi$ at the center frequency lead to relation (3-7):

$$f_c = \frac{c_0}{2l_c(\sqrt{\varepsilon'_{eff,2}} - \sqrt{\varepsilon'_{eff,1}}) + 4l_{\lambda/4}\sqrt{\varepsilon' eff, rat}} \tag{3-7}$$

In this equation, $\varepsilon'_{eff,1}$ refers to the effective dielectric constant of the sensing line, $\varepsilon'_{eff,2}$ to that of the reference line and $\varepsilon'_{eff,rat}$ to the effective dielectric constant of the lines composing the hybrid ring coupler. The length $l_{\lambda/4}$ is designated in 3-11a.

Equation (3-7) gives a very first approximation of the expected behavior of the circuit in terms of center frequency shift versus permittivity changes of the MUT and hence is serving the purpose of giving an understanding of the functional principle. The combined sub components constitute an interferometer, which identifies marginal changes through superposition.

A more accurate mathematical model is based on microwave network analysis using two-port blocks representing the single transmission line sections of the RF circuitry. The partitioning of the RF network is indicated in Fig. 3-11b. Since it exhibits shunt and series components, one appropriate method is to use ABCD and Y-parameters and convert them to the S-parameters which are finally desired. A Matlab code was created for that purpose based on the schematic block diagram displayed in Fig. 3-11b. To obtain the overall transfer function, it is necessary to split the depicted circuit and derive the S_{31} and S_{32} functions individually. Afterwards, the vector sum is calculated to get the superimposed output signal. Both input ports (1,2) are assumed to be excited with the same power and in phase. The basic mathematical functions that are part of the matrices are simple solutions of the wave equation describing the transfer characteristics of the standalone components visible in Fig. 3-11b. The model takes loss of the line into account leading to an ABCD matrix of a simple line as follows:

$$A = \begin{bmatrix} \cosh(\gamma l) & Z_0 \sinh(\gamma l) \\ 1/Z_0 \sinh(\gamma l) & \cosh(\gamma l) \end{bmatrix} \tag{3-8}$$

In the above matrix l is the length of the line and γ the complex propagation constant, comprised of the attenuation and the phase constant as follows:

$$\gamma = \alpha + j\beta \tag{3-9}$$

To determine the complete transfer characteristics, the ABCD matrix of the shunt impedance Z_0 must be taken into account.

$$A_Z = \begin{bmatrix} 1 & 0 \\ 1/Z_0 & 1 \end{bmatrix} \tag{3-10}$$

It represents the $50\,\Omega$ terminations present in the design in Fig. 3-11. To calculate S_{31}, two parallel paths, the upper and the lower signal path in Fig. 3-11, are taken into account and the following calculation scheme, exemplarily shown for S_{31}, is applied:

$$\begin{aligned} A_{31_1} &= A_{\lambda/4} && \rightarrow Y_{31_1} \\ A_{31_2} &= A_{\lambda/4} \cdot A_Z \cdot A_{\lambda/4} \cdot A_Z \cdot A_{\lambda/4} && \rightarrow Y_{31_2} \\ Y_{31_{tot}} &= Y_{31_1} + Y_{31_2} && \rightarrow S_{31_{tot}} \end{aligned} \tag{3-11}$$

The arrows indicate a conversion from ABCD to Y- or S-parameters. The same scheme holds for S_{32}. The vector sum of S_{32} and S_{31} represents the transfer function S_{21} for the hybrid ring coupler driven by a Wilkinson power splitter. The calculated results are depicted in Figs. 3-12 and 3-13 for different parameters $\Delta\alpha$ and $\Delta\varphi$. The initial transfer function is displayed in Fig. 3-12 for $\Delta\alpha = 0$. The graph represents the characteristics of an unloaded sensor. It is shown that the interferometer behaves like a notch filter with a minimum S_{21} at the center frequency, here 120 GHz.

This analytical model of the interferometer was used to investigate the impact of different parameters being relevant for the proposed sensing technique. It can be used to demonstrate the impact of phase and attenuation changes induced by a sample under test onto the signal propagated by the sensing line. The investigations point out that the hybrid ring coupler conducts a separation of phase and attenuation effects. The model was applied to simulate the coupler's response to an imbalance between both input signals in terms of amplitude. The graph in Fig. 3-12 shows the calculated S_{21} for different signal attenuation from 1-10. Transfer functions are simply shifted in power, whereas phase imbalances

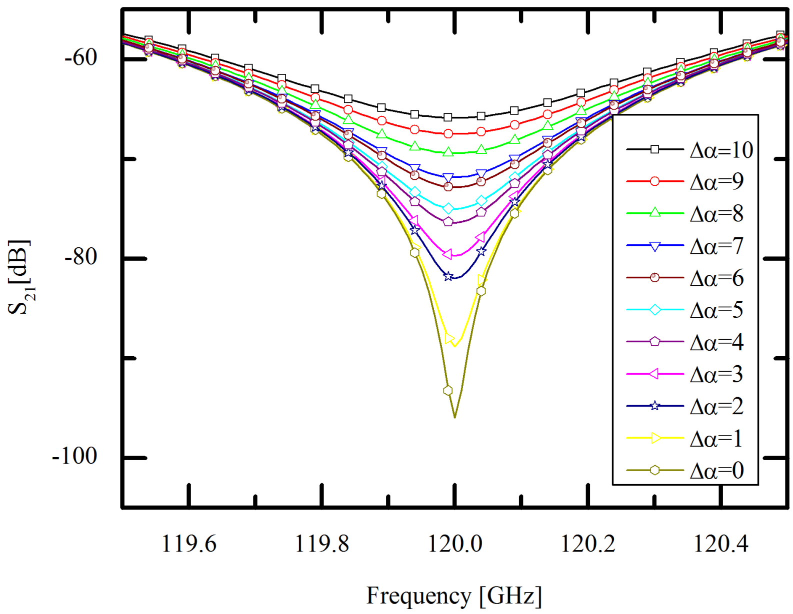

Figure 3-12: *Hybrid ring coupler transfer function* S_{21} *with attenuation as parameter.*

cause a frequency shift in the S_{21} notch, as displayed in Fig. 3-13. This feature of the hybrid ring coupler enables the great potential of characterizing different dielectric properties of samples individually. However, when a sample changes both the attenuation and the phase of the sensing line, the attenuation affects the phase frequency characteristics of the interferometer. The occurrence of the combined effects might veil the results, depending on the magnitude of attenuation. Chapter 6 will address this issue and a solution will be presented.

Figure 3-13 highlights that the absolute minimum of the transfer function achievable by the circuit is neither for 0° phase shift nor at 120 GHz. The figure displays the extracted

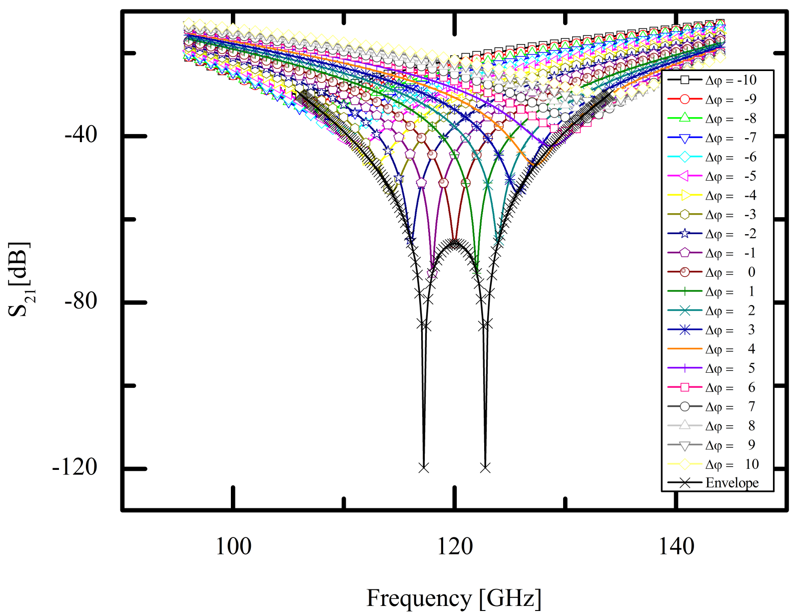

Figure 3-13: *Hybrid ring coupler transfer function* S_{21} *with phase as parameter.*

minimum from all S_{21} functions for the different phase differences designated as envelope. The envelope shows the two absolute minimums that are achievable by phase tuning symmetrically positioned around 120 GHz. To explain that effect, further simulations using ADS were conducted. Additionally, these simulations account also for other effects in the RF circuitry, like frequency dependent port matching. The transmission of the interferometer simulated with ADS is displayed in Fig. 3-14. It is confirmed that the absolute minimum of the transfer function achievable by the circuit is not for 0° phase shift. This can be understood with the help of the hybrid ring coupler transfer functions displayed in Fig. 3-15.

The hybrid ring coupler does not feature absolute symmetry for both paths S_{31} and S_{32} leading to a different power level at the center frequency. This is evident from the gap in the transfer functions at 120 GHz as depicted in Fig. 3-15. At the center frequency, the phase condition for a minimum in the superimposed signals stated in (3-7) at port 3 is fulfilled, so that the minimum appears despite the magnitude imbalances. In other words, the phase difference of 180° is always the dominant factor. When an additional phase shift is introduced in the measurement path, it can be achieved that both criterions - equal amplitude and 180° phase difference - are fulfilled simultaneously. This leads to a lower minimum and a higher Q-factor of the interferometers S_{21}. The sensitivity is not affected by that, as evident by the linear phase frequency behavior of the interferometer shown in Fig.3-16. The Figure compares the frequency phase correlation obtained from Matlab and ADS simulations to validate the calculation scheme. Even though the sensitivity in terms of frequency shift versus phase change is not affected by the deeper notch level, still, the potential read-out precision is increased for higher Q-factors since higher changes in the power level are occurring. Further investigations of the phase frequency characteristics were conducted. The impact of simultaneous changes of phase and attenuation was simulated and the results are depicted in Fig. 3-17a.

To emphasize the impact of the attenuation, a constant phase shift of 2° was adjusted and

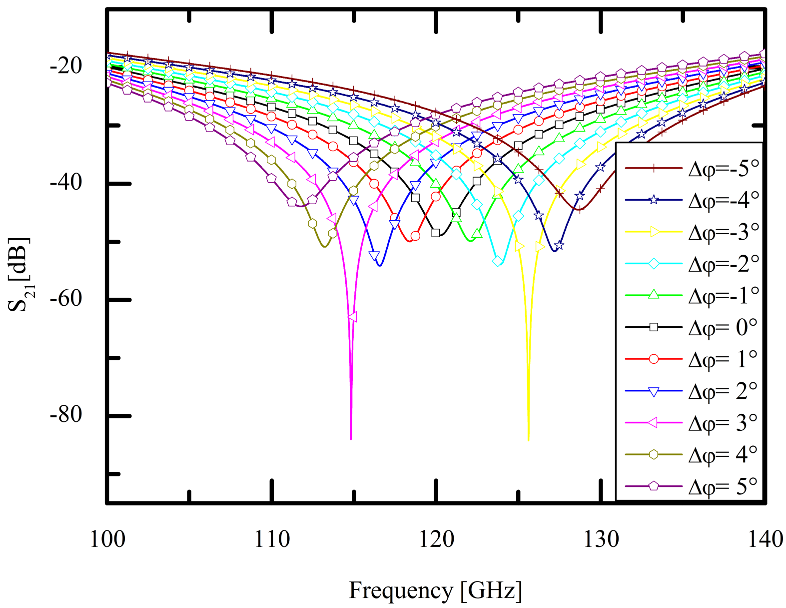

Figure 3-14: *ADS simulation of the interferometer transfer function* S_{21}.

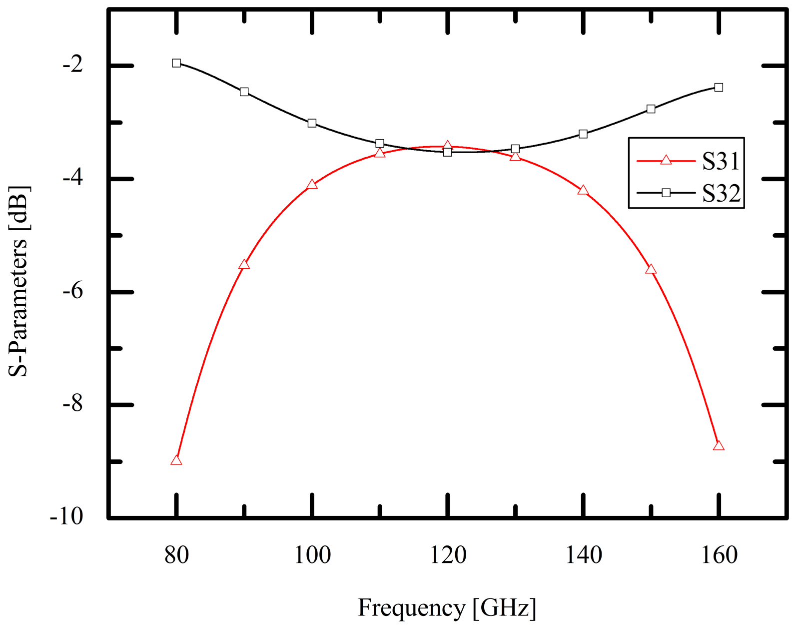

Figure 3-15: *ADS simulation of the hybrid ring coupler transmissions S_{31} and S_{32}.*

the attenuation was varied from 0-0.2. The figure displays S_{21} versus frequency. The center frequency, reflected by the S_{21} minimum is depending on α as depicted in Fig 3-17b. As expected, the impact of phase shift onto the center frequency is the highest for zero attenuation, which hence is the operation point of maximum sensitivity. The position of the S_{21} minimum is determined by a combined effect of the phase difference and the amplitude of the signals entering the hybrid ring coupler. When the attenuation in the reference path is increased, it means that this attenuation is added to the transfer function of the coupler. This can be visualized by shifting down the S_{31} curve depicted in Fig.

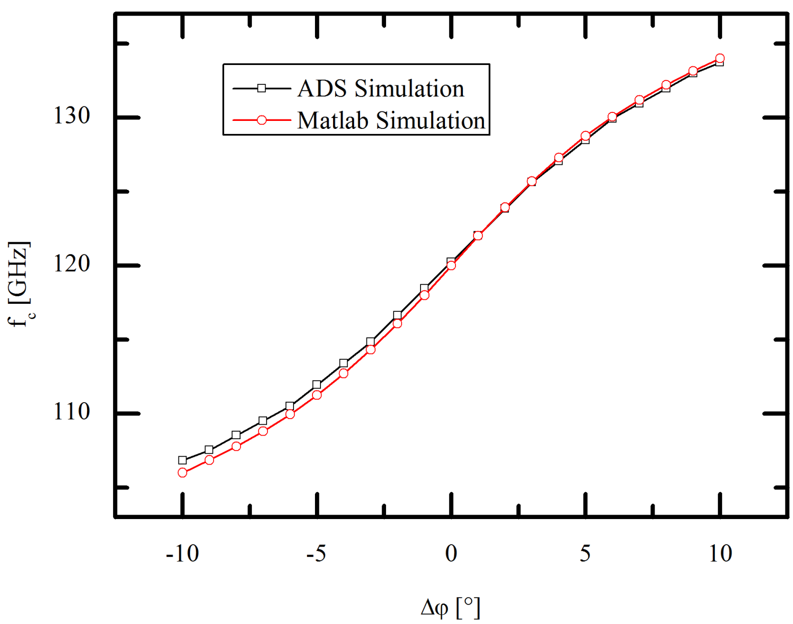

Figure 3-16: *Center frequency f_c of the transfer function versus phase imbalance $\Delta\varphi$.*

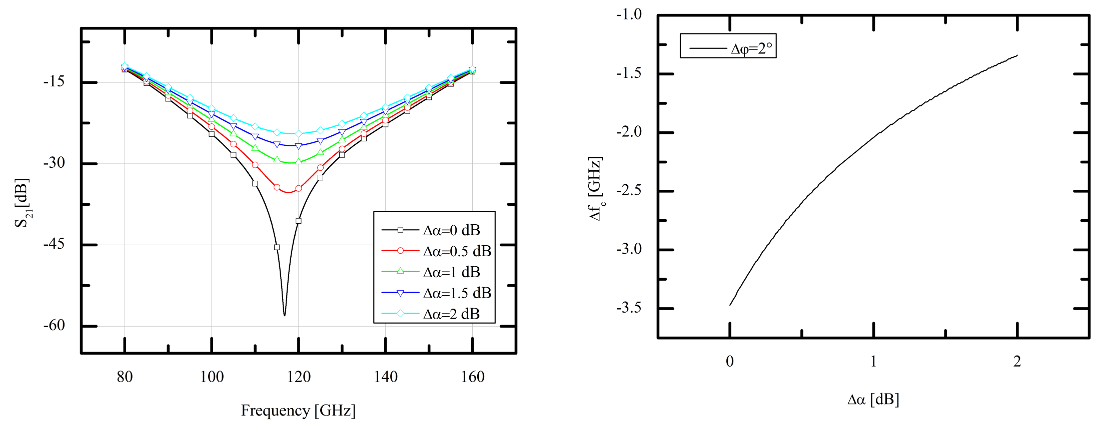

(a) S_{21} *for a phase shift of* 2°.

(b) *Frequency shift evoked by* 2° *phase shift versus attenuation.*

Figure 3-17: *Effect of attenuation on the interferometer transfer function.*

3-15 by the amount of attenuation added by the measurement line's attenuation. For low attenuation differences, the reference and the measurement path, S_{31} and S_{32}, match best, hence, the minimum is mainly governed by the position of a 180° phase shift. For higher differences in attenuation, the amplitudes are not matched anymore becoming a relevant factor for the notch position in frequency. To illustrate that effect, Fig. 3-18 compares the actual notch position with the frequency where a 180° phase shift between the two signals occurs. Simulation results depicted in Fig. 3-18 were obtained using ADS. The

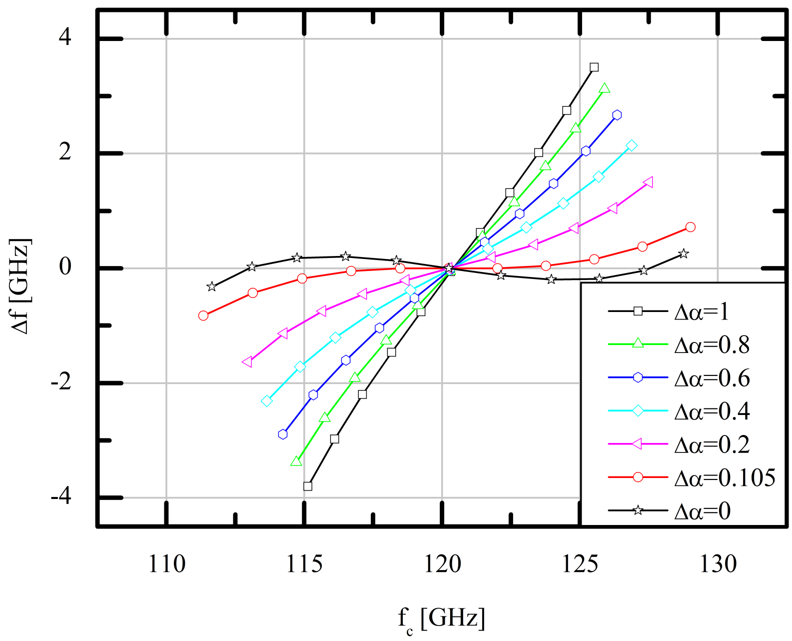

Figure 3-18: *Notch (center) frequency deviation from frequency where* 180° *phase shift occurs.* $-5° \leq \Delta\varphi \leq 5°$.

phase was swept from $-5°$ to 5° to shift the S_{21} notch in frequency. The attenuation of the measurement line was adjusted to several values, as stated in the legend of Fig. 3-18. This emulates the behavior of a sample that affects both, propagation phase and frequency. The parameter α was altered to demonstrate the effect of attenuation onto the frequency shift. The key information obtained from that simulation is that attenuation affects the frequency shift due to the fact that the phase condition, a 180° phase shift between reference and measurement signal, is not dominating anymore and the amplitude's impact increases.

For small phase differences in the measurement and the reference path the notch shift is approximately linear. When it increases above that linear region, it shows hyperbolic behavior. For the target applications and the planned setup, phase changes induced into the measurement microstrip are less than 2° at 120 GHz. This will be calculated in chapter 6. For that reason, the hybrid ring coupler's response is considered to be linear and the sensitivity according to simulation results is $\Delta f_C/\Delta\varphi = 1.8\,\mathrm{GHz}/°$ saying that the interferometer gets tuned by 1.5 % for 1° phase shift. The linear phase frequency characteristics along with the high sensitivity render the interferometer the method of choice for measuring dielectric properties of samples.

3.4 Summary

This chapter demonstrated read-out circuits for collaboration with the sensors presented in chapter 2. The generic approaches, the reflectometer and the VNA, showed the highest potential accuracy. This was demonstrated by comparing measurement results to results achieved by commercially available VNAs. The flexibility of both approaches makes them applicable to all the discussed sensor structures. Hence, they are preferable when lab experiments with several sensor structures are desired. Still, their design exhibits also the highest complexity and also the biggest size and power consumption, which is not feasible for portable dielectric sensors. For reading out IDCs and stub lines, the tuned oscillator method was presented. Since it is based on a resonant approach, it shows a high sensitivity towards changes in the dielectric sample. If a high accuracy is desired with reasonable effort, the models for dielectric constant extraction become quite elaborate owing to the nonlinear response. Thus, a final system would need extensive computation capability, unwanted for compact and portable solutions that are targeted here. The interferometer approach showed linear behavior within the desired phase range. A direct digital read-out feature, that was developed within the frame of this thesis, will be presented in chapter 6. These features yield in a powerful sensing device to characterize biological and medical dielectric samples.

To experimentally examine the interferometer concept, it was first implemented in the 7 GHz range on a PCB and measurements with biological samples were conducted. The following chapter presents the design of the microwave interferometer, related topics and finally measurement results.

4 Microwave Interferometer

It has been demonstrated in section 3.3 that the interferometer concept can be realized with the help of microstrip lines acting as both transmission line structures and sensing elements. One goal of this thesis is the development of an on-chip dielectric sensor for lab-on-a-chip solutions to provide a miniature device to characterize dielectric samples. The first step in that direction has been to implement a highly compact sensor at microwave frequencies, in order to experimentally investigate the operation principle of electrical interferometers in the context of dielectric characterization. The frequency range was chosen in the proximity of 7 GHz to compare simulation and measurement results to experiments presented in [76], where this concept was realized as a single component using one complete wafer. Moreover, the use of this frequency range is profitable due to two aspects: ease of fabrication, which is practical using a printed circuit board setup with the appropriate epoxy material and the low complexity of measurement equipment and the measurement procedure. Both aspects significantly reduce the timeframe of the construction process to finally gain experimental results. The structure presented in the following could be fabricated in-house using a laser based PCB structuring device. In addition to that, it is feasible to measure the microwave sensor using SMA connectors and coaxial cables. This alleviates the measurement procedure notably, since no on-wafer measurement equipment is required. Still, the electromagnetic processes are the same compared to a higher frequency spectrum in the millimeter-wave range, so this structure is well suited as an experimental test setup to investigate dielectric sensing applying electromagnetic waves in particular in an interferometer. The microstrip line based circuitry was designed using proper line models followed by EM simulations based on the method of moments technique with very high accuracy so that the fabrication step could be accomplished without the need for several iterations. The design methodology followed by simulations and experimental results are demonstrated in the following subsections.

4.1 Design

In section 2.4 it has been explained that the EM field of a microstrip line is suitable to detect and characterize dielectric materials. In the chosen frequency range, this structure can be implemented on a printed circuit board. The principle is based on the parallel sensing line approach discussed in section 2.4 and is displayed in Fig. 4-1. The Wilkinson coupler at the input provides two signals equal in magnitude and phase to the following microstrip sensors. The hybrid ring coupler superimposes both signals with a certain frequency dependent phase difference at the output port, denoted Δ in Fig. 4-1. Because of its properties underlined in section 3.3, the hybrid is the most vital element in this design. The key functions of the applied devices relevant for the overall design will be explained later in this chapter.

The following design considerations are customized for a Rogers 3003 (RO3003) material PCB, since it exhibits excellent radio frequency characteristics in the applied band [77], namely a frequency stable dielectric constant and a low loss factor. The approach ex-

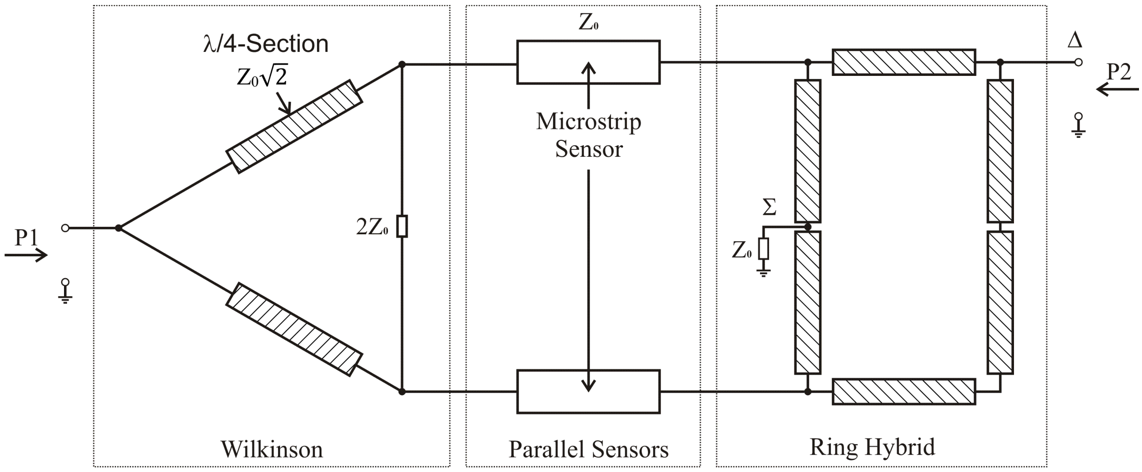

Figure 4-1: *Schematic of the microwave interferometer.*

plained in section 3.3 can be realized on the basis of microstrip lines exhibiting 50 Ω or 70.71 Ω as characteristic impedance, respectively. Additionally, two surface mount device (SMD) resistors are required. This guarantees that interfaces between circuit stages do not cause high reflections caused by impedance mismatch of transitions since the sensing structures are also microstrip lines. In addition to that, all of the interferometer components are passive, thus beneficial in terms of power dissipation and linearity. The presented methodology requires the following steps of development:

- Determination of the microstrip line geometry for different characteristic impedances
- Calculation of the effective wavelength stemming from the substrate and the line geometry
- Designing the circuit components based on previously determined parameters
- EM simulation of the single components and their composition followed by iterative optimization
- Fabrication and measurements

The optimum geometry of a microstrip is determined by two parameters, depicted in Fig. 2-13. These are the substrate thickness h and the substrate dielectric constant ε_{r1}. The chosen substrate exhibits the following parameter values: $h = 127\,\mu\text{m}$ (5 mil) and $\varepsilon_{r1} = 3$ [78]. One way to accurately calculate the geometrical parameters is to apply the Hammerstad and Jensen formula. This formula describes the static impedance, Z_0 and the effective dielectric constant, ε_{eff} [79]. The attenuation factor, α, is calculated using the rule of incremental inductance [80]. For these calculations, the tool LineCalc, a software feature of ADS, was used, which is based on the aforementioned formulas and rules. The tool can be used to synthesize the line parameters for the required impedance and respective substrate. The line width that is obtained by that procedure is $w_l = 302\,\mu\text{m}$. It is noticeable that the applied calculation tool is considering frequency dispersion, skin effect and dielectric loss. This leads to highly accurate parameters for microstrip line design comparable to parameters gained by applying EM characterization techniques.

To reach close agreement between simulations and measurements, the calculated parameters were taken as a start value and the structure was simulated using the method of moments approach [81]. The results of that simulation can be evaluated for identifying all details about the line, the characteristic impedance, the effective permittivity and several other parameters. The most relevant parameters for this design are the characteristic line impedance for good matching, and the effective permittivity, since the other circuits' performances described later are depending on a well defined line impedance and phase propagation. The line width has been optimized considering the boundaries of fabrication accuracy. The resulting value is $w_l = 300\,\mu\mathrm{m}$, which is very close to the value obtained by using LineCalc. To calculate the effective permittivity of the microstrip realized on that particular substrate, the phase of the scattering parameter S_{21} was evaluated leading to $\varepsilon_{eff} = 2.51$. This value is used to calculate the wavelength of a signal propagated by that line using (4-1):

$$\lambda = \frac{c_0}{\sqrt{\varepsilon_{eff}} f} \tag{4-1}$$

As a result, the wavelength of the described microstrip transmission line is $\lambda = 27.04\,\mathrm{mm}$. To obtain a characteristic line impedance of $70.71\,\Omega$, a line width of $w_l = 160\,\mu\mathrm{m}$ needs to be applied. The resulting wavelength is $\lambda = 27.82\,\mathrm{mm}$. The different wavelength is ascribed to a different ε_{eff} stemming from a different line width. The wavelength is important since the developed components are distributed microwave circuits using lines in multiples or fractions of the signal wavelength at the chosen frequency of operation to achieve impedance matching. The calculated parameter values were used for a first design of the coupler structures explained in the following.

Since the combination of several line elements forming a distributed microwave circuit will add parasitic effects due to junctions and bends, the respective circuit needs to be EM characterized, scaled, and optimized in several simulation iterations. Also, solder pads for SMD elements add capacitance that needs to be taken into account.

The method described in 3.3 requires two identical signals, equal in phase and magnitude, one as a reference and one as a measurement signal. A passive circuit based on microstrip lines that generates two equal signals from a single input is the Wilkinson power splitter [82]. The basic principle and layout of the splitter is displayed in Fig. 4-2.

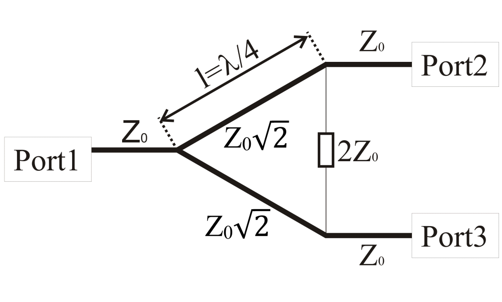

(a) *Schematic.*

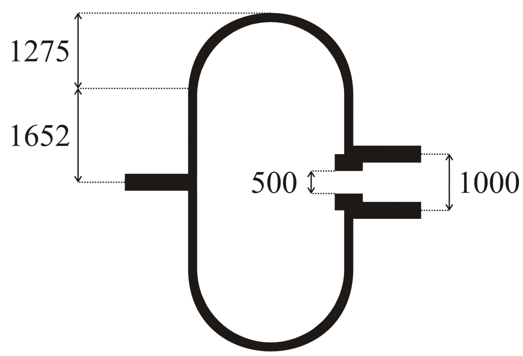

(b) *Layout (true to scale, units in* µm*).*

Figure 4-2: *Wilkinson power splitter.*

To characterize the behavior of that circuit, one can apply an even-odd mode analysis technique [83]. In doing so, the depicted power splitter can be broken down to two quarter

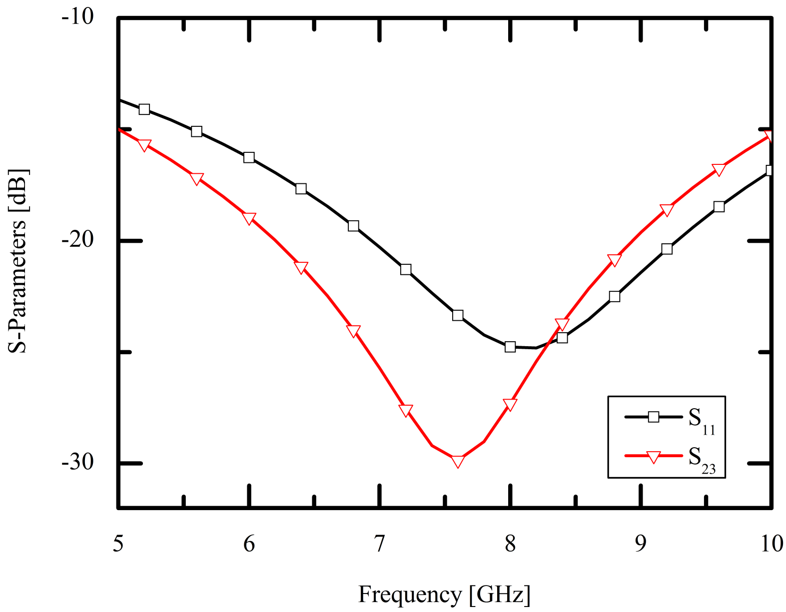

Figure 4-3: *Input matching and isolation of the Wilkinson split ports.*

wave transformers in parallel. The input and output ports are connected to 50 Ω lines respectively. To achieve matching at the split ports, serving as output ports, and the common port at the input, the quarter wave transformers need to have a characteristic impedance of $Z_C = Z_0\sqrt{2}$. A reciprocal and zero-loss three port network cannot be matched at all three ports simultaneously. This is why a 100 Ω resistor, or more generally speaking, an element of twice the characteristic impedance, needs to be inserted between the split ports. The input impedance of the Wilkinson can be derived by analyzing one branch of the symmetrical structure and subsequently calculating the input impedance of two of those branches in parallel. The circuit displayed in 4-2 can be viewed as two quarter wave transformers in parallel with a 50 Ω load. Neglecting the loss, the impedance of the half circuit can be calculated by [55]:

$$Z_{in} = Z_C \frac{Z_L + jZ_C \tan \beta l}{Z_C + jZ_L \tan \beta l} \tag{4-2}$$

Here, Z_C is the characteristic impedance of the quarter wave lines, Z_L is the load impedance, β is the phase constant and l is the line length. For $l = \lambda/4$ and $Z_C = 50\,\Omega\sqrt{2} = 70.71\,\Omega$, this impedance amounts to $Z_{in} = 100\,\Omega$. That means two of those lines in parallel exhibit 50 Ω as the overall target input impedance. Similar calculations can be conducted for both output ports, leading to 50 Ω at the designated center frequency. The lumped 100 Ω resistor serves matching and enhances isolation between Port 2 and Port 3. The final layout, that was characterized and optimized for a 127 µm Rogers RO3003 PCB using MoM simulations, is depicted in Fig. 4-2b. One very important layout aspect, when a PCB implementation is intended, is the quarter wave lines ending exactly at the pads accommodating the 100 Ω SMD resistor to eliminate parasitic effects of leads. The simulation results for the layout depicted in Fig. 4-2b are presented in Figs. 4-3 and 4-4. The graph in Fig. 4-4 shows that the transmission behavior of S_{31} and S_{32} is identical. This only holds for perfectly matched output ports. The simulated input matching is better than −20 dB. Another essential aspect to be considered for this circuit to work properly, is the

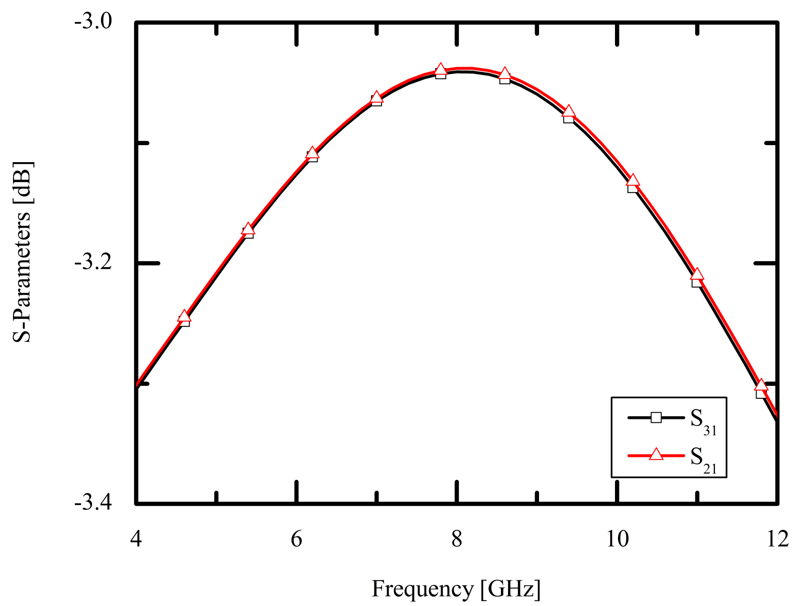

Figure 4-4: *Transmission characteristics of the Wilkinson power divider.*

isolation of the split ports. The graph in Fig. 4-3 displays the input matching as well as the isolation of the output ports. The isolation is also better than −20 dB in proximity to the center frequency of 7 GHz. These properties render the circuit suitable for providing signals identical in phase and magnitude while ensuring sufficient isolation and input matching to 50 Ω. A similar design methodology was applied for the hybrid ring coupler, explained in the following.

As the Wilkinson, the hybrid ring coupler is based on line wave transformers in parallel, in order to provide matching at all ports simultaneously. Fig. 4-5a illustrates the basic function of the hybrid ring coupler.

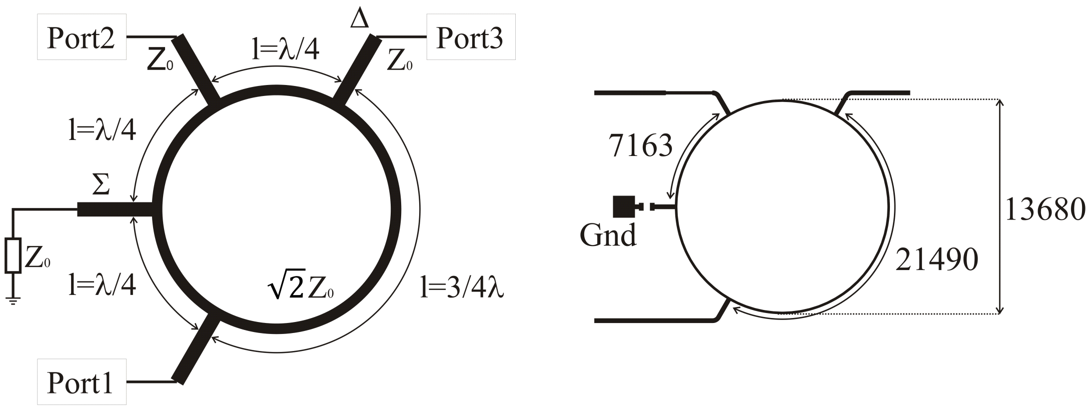

(a) *Schematic.* (b) *Layout (true to scale, units in* μm*).*

Figure 4-5: *Hybrid ring coupler.*

The port numeration starts from the input ports, indicating the mode of operation in the final application, where Port 1 and Port 2 will be used as input and Port 3 as the output port. To obtain an input impedance of Z_0 at all ports, the inner ring needs to exhibit a

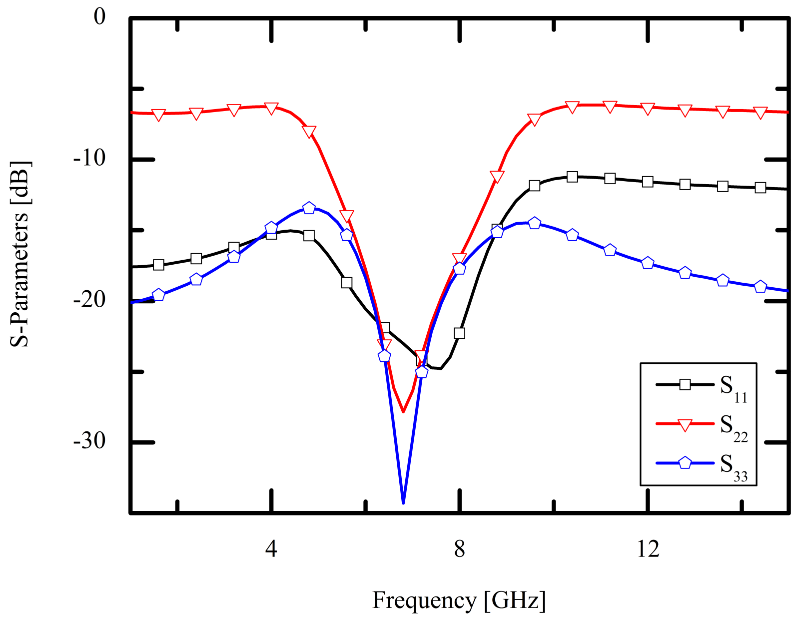

Figure 4-6: *Simulated matching and isolation of the respective hybrid ports.*

characteristic impedance of $\sqrt{2}Z_0$. In the target application, the sum port designated with Σ, is terminated with a resistor of Z_0. In that constellation and given that it is operated at the designed center frequency, the hybrid ring coupler derives the difference of the input signals fed to Port 1 and Port 2 and provides the result at its output Port 3, also referred to as Δ port. This behavior is valid for an ideal zero-loss hybrid ring coupler driven at its center frequency. In that case, the circuitry shown in Fig. 4-5a can be characterized using even- and odd mode analysis [55], [84] leading to the following scattering matrix.

$$S = -j/\sqrt{2}\begin{bmatrix} 0 & 0 & -1 \\ 0 & 0 & 1 \\ -1 & 1 & 0 \end{bmatrix} \tag{4-3}$$

The matrix shows that in the discussed ideal case, Port 1 and Port 2 are completely isolated from each other. To investigate the real behavior of the hybrid ring coupler, it has been characterized using MoM simulations. The start value for the line length (Lambda fourth) at the design frequency was obtained by MoM simulations of the single microstrip. Subsequently, the necessary perimeter of the hybrid ring coupler was calculated to obtain the desired circuit function. Later, the complete coupler was EM simulated for optimization and compensation of parasitic effects contributed by joints of wires and solder pads for SMD elements. The resulting final structure is depicted in Fig. 4-5b. The MoM simulation results are represented by the graphs depicted in Figs. 4-6 and 4-7. As shown in Fig. 4-6, the matching at all three ports used as input and output is about −25 dB around 7 GHz. The insertion losses from the input ports to the output, displayed in Fig. 4-7, are very close to the ideal value of −3 dB at the center frequency, thanks to a very low loss tangent of the Rogers material and a high conductivity of the copper.

The presented couplers are part of the final design structure that is schematically displayed in Fig. 4-1. The Wilkinson drives the parallel lines used as sensor and reference and the hybrid ring coupler evaluates their different propagation properties. This leads to the final layout of the microwave interferometer depicted in Fig. 4-8.

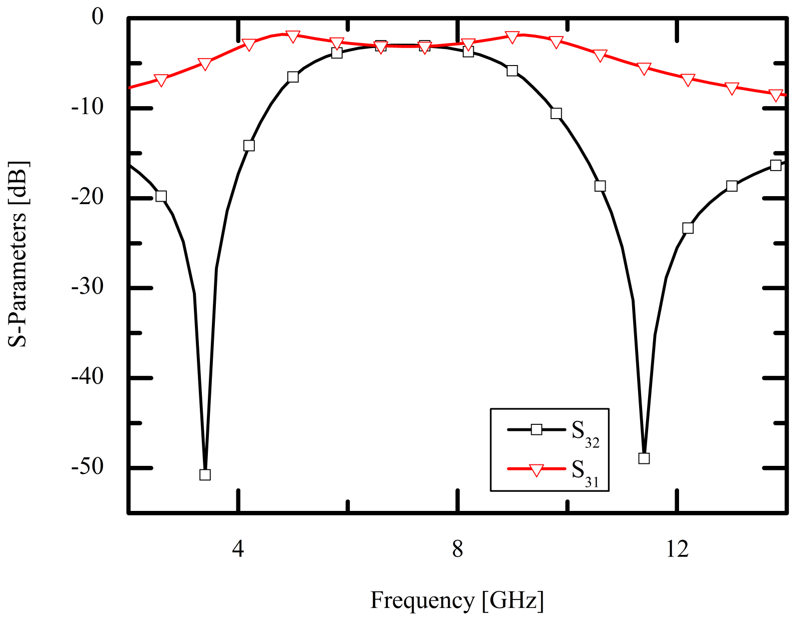

Figure 4-7: *Simulated transmission of the respective hybrid ports.*

For measurement purposes, the PCB needs to be equipped with SMA connectors, being suitable for frequencies up to 18 GHz. In the presented design, edge mount connectors are applied and their footprint is displayed in Fig. 4-8 at the in and output, respectively. To investigate their influence onto matching and transmission, the displayed design has been simulated for both constellations with SMA connectors and without. The input reflection as well as the transmission is depicted in Fig. 4-9.

The input matching S_{11} is around -25 dB in the frequency range of interest, when the influence of SMA connectors is neglected. The simulations depicted in Fig. 4-9 show that this value is shifted to an increased ratio due to the impact of SMA connectors. The transmission S_{21} is lower than -40 dB, indicating a high path symmetry of the reference and the measurement path. The ideal value is much lower, because under ideal circumstances, the magnitude of both signals - the reference and the measurement signal - are identical, leading to a value of S_{21} of minus infinity. Higher symmetry can enhance the

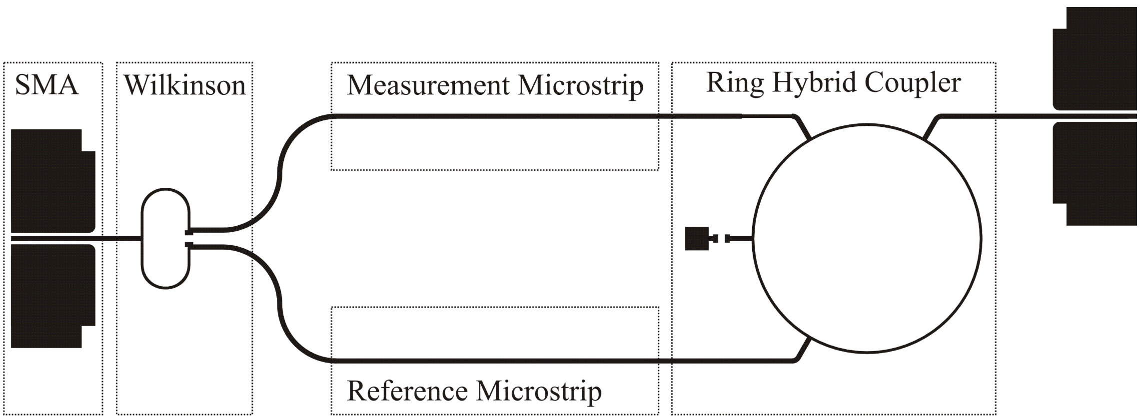

Figure 4-8: *Layout of the microwave interferometer.*

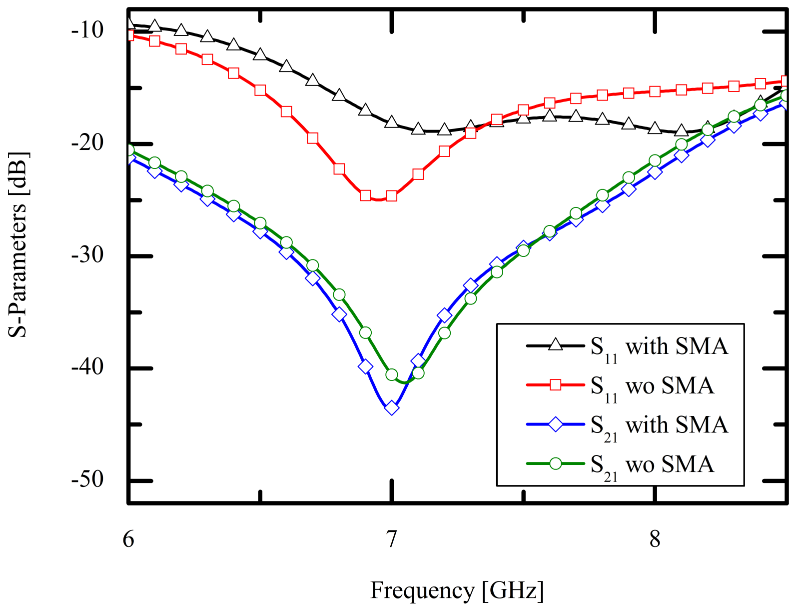

Figure 4-9: *Simulated S-parameters of the microwave interferometer with and without SMA connectors.*

performance of the circuitry - section 4.3 demonstrates a strategy to achieve that.

The most important property of the hybrid ring coupler is the correlation of phase difference of the two input signals and the frequency shift of the S_{21} minimum in the overall transfer function of the interferometer. To simulate the response of the hybrid ring coupler to a phase imbalance of its input signals, ideal phase shifting elements have been inserted in the measurement and the reference path of the interferometer. Fig. 4-10 displays the simulated results for a phase difference from $-10°$ to $10°$. The characteristic behavior

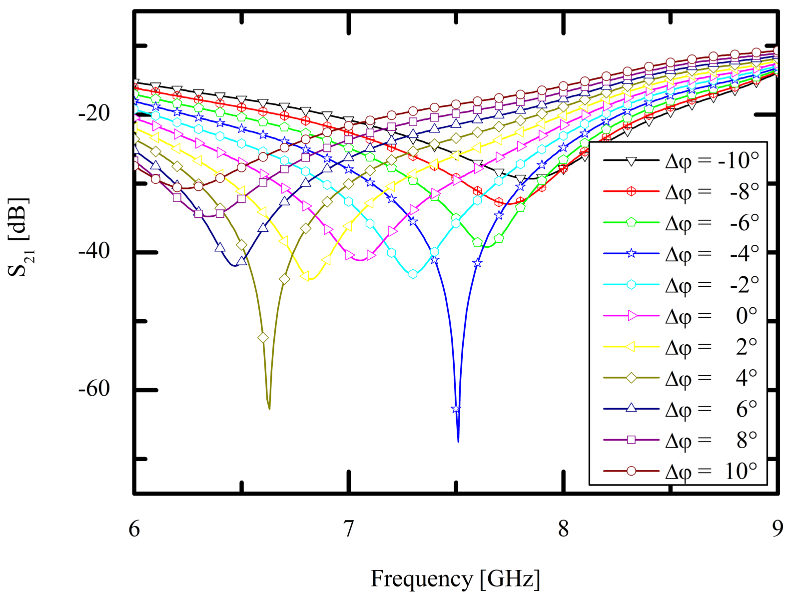

Figure 4-10: *Simulated performance of the microwave interferometer for phase differences below* 10°.

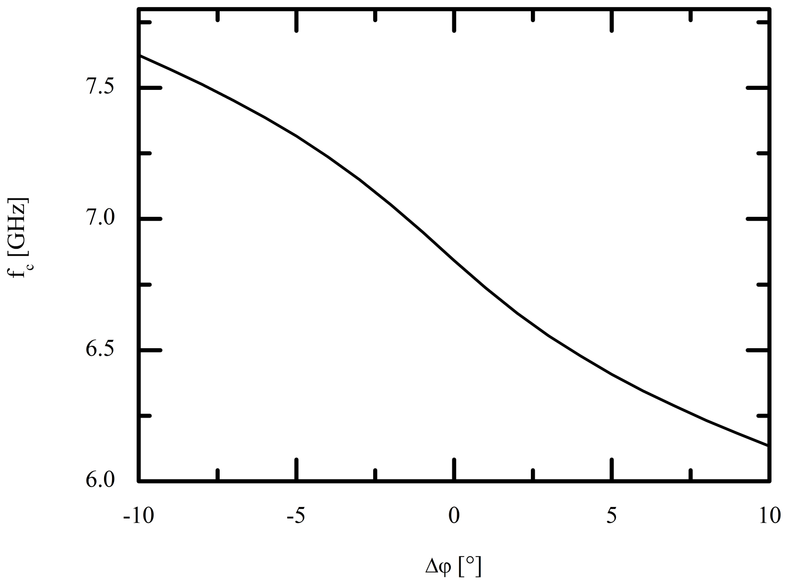

Figure 4-11: *Simulated shift of the notch frequency for phase differences below* 10°.

observed here was investigated and explained in section 3.3. By tuning the phase, it is possible to adjust the notch frequency and to realize both, optimum phase and amplitude conditions at the same time. The much deeper notch power level and the higher quality factor are a valuable feature when power measurements are applied to derive the notch position in terms of resolution and accuracy. In Fig. 4-10, the highest Q-factors are obtained for a phase shift of $\Delta\varphi = \pm 4°$. Increasing the resolution of the simulated phase sweep, even deeper notch levels and higher Q-factors are achievable. The minimum level observed for both simulations and measurements is below -100 dB.

The results depicted in 4-10 were evaluated to investigate the phase frequency characteristics of the hybrid ring coupler. The extracted frequency shift versus phase difference is plotted in Fig. 4-11. The graph shows that the highest change in frequency is obtained at the center position for a phase shift of zero. It demonstrates that the best point of operation for the interferometer is at an initial phase shift of zero, to achieve the highest possible effect in terms of frequency shift. On the downside, there is a lower Q-factor at that exact point due to amplitude imbalances, making a different point of operation with a higher Q-factor favorable for better read-out capabilities.

Chapter 5 will demonstrate that the relevant phase range in the intended application is below 2°. It can be inferred from Fig. 4-11, that for this range the phase frequency correlation can be considered to be linear. The maximum error using a linear fitting function was determined to be 6.64 MHz, what amounts to 0.059 %. The slope of the linear function is $\Delta f/\Delta\varphi = -103.9\,\text{MHz}/°$. This also means that in the relevant phase range for target samples, a higher quality factor, obtained by phase calibration, is not affecting the sensitivity $\Delta f_c/\Delta\varphi$ of the interferometer since the sensitivity can be considered constant. However, such a high quality factor is very important for accurate notch frequency detection since the output power range, the measured parameter, is significantly increased. This raises the resolution of the interferometer.

Furthermore, since the explained concept is based on a phase frequency relation, the sensor sensitivity is depending on the absolute operational frequency of the hybrid ring cou-

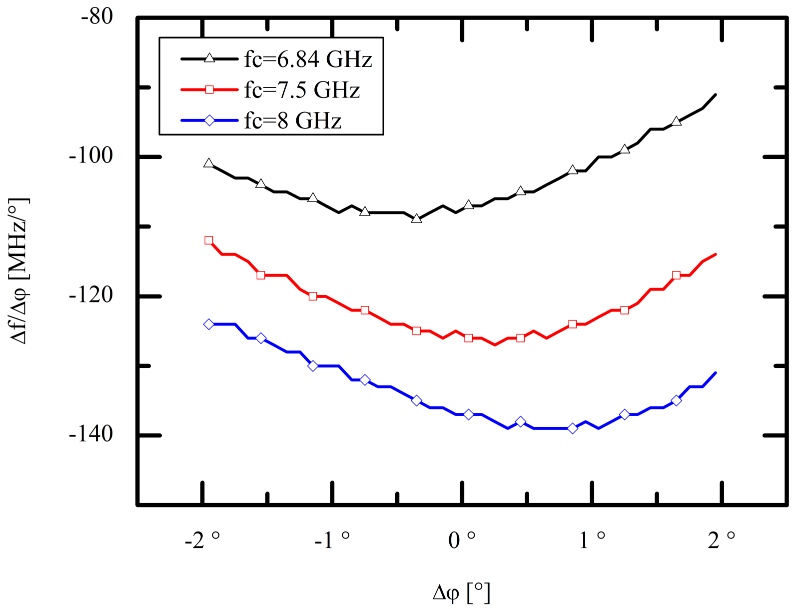

Figure 4-12: *Simulated sensitivity of the hybrid ring coupler for different operational frequencies.*

pler, since it is the component conducting the phase frequency conversion. To investigate the frequency dependency, the hybrid ring coupler has been scaled and EM simulated for different frequencies of operation. The extracted sensitivities for three different hybrid ring coupler versions working at different frequencies are depicted in Fig. 4-12. The simulation results show that the maximum sensitivity of a hybrid ring coupler working at 6.8 GHz is increased from -109 MHz/° to -139 MHz/° by scaling it to work at 8 GHz. This is a very important feature of that device. Along with investigations that will be presented in chapter 5, this is the main reason for scaling and implementing the interferometer approach at millimeter-wave frequencies. The development of the millimeter-wave interferometer will be presented in chapter 6.

In addition to scaling, there are further techniques to increase the sensitivity of the hybrid ring coupler. The transfer functions of the coupler depicted in Fig. 4-5 have two cross points as explained earlier. This is due to the different path lengths from Port 1 to Port 3 compared to Port 2 to Port 3, provoking a different transmission magnitude due to loss, impairing the symmetrical transfer behavior. To increase the sensitivity of the sensor, the different path losses need to be compensated for. Inherently, the longer line between Port 2 and Port 3 has higher loss. If that loss is compensated for or introduced into the other path as well, it can be achieved to attain a single intersection of the two graphs from 4-7 at the center frequency by shifting S_{31} downwards.

In [76], a method was introduced, where the different sections of the hybrid ring coupler feature diverse metal thicknesses. There, two liftoff process steps are performed and different masks come into operation. To limit the effort, a different strategy was pursued in the presented approach. To introduce loss in the upper path, the lead to Port 1 of the coupler, a distinct section of that transmission line was tapered as indicated in Fig. 4-13. The original line width for a 50 Ω line is 300 µm for the deployed layer configuration. EM simulations using the MoM approach led to an optimum overall sensor sensitivity when

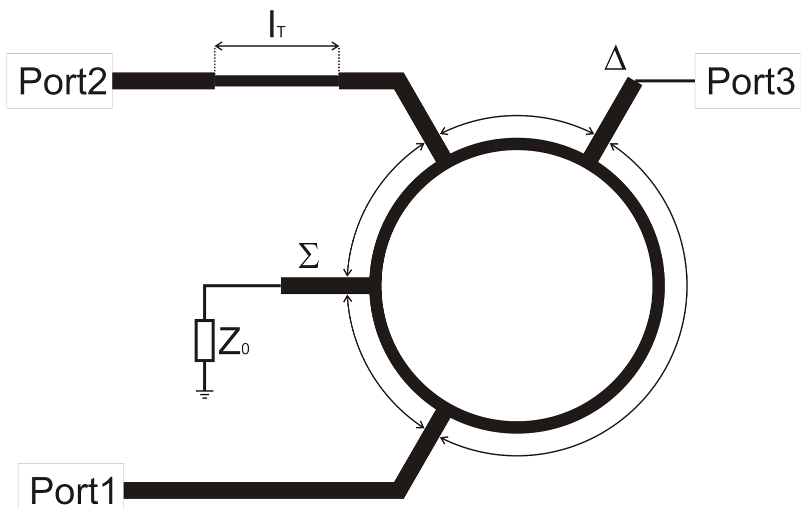

Figure 4-13: *Modified hybrid ring coupler setup with tapered line section.*

a 2 mm long piece of line with a width of 180 μm is inserted into the measurement path, as indicated in Fig. 4-13. The simulated performance of the sensor achieved with this modification was demonstrated in [7].

The impedance change of this modification causes a certain amount of reflections in the upper signal path. Still, the input matching of the complete interferometer is not affected by this since the precedent Wilkinson splitter contains a 100 Ω resistor for isolation [85] and balance. The designed structure has been fabricated on a PCB and the complete measurement setup is explained in the following subsection.

4.2 Experimental Setup

The sensor concept was implemented in the 7 GHz range to characterize the permittivity of fluids confined in Teflon capillaries serving as a microfluidic channel. This channel was pressed on top of the PCB with the help of customized polyvinyl chloride (PVC) jaws. The interferometer, which is a completely passive circuitry, needs to be evaluated by performing S-parameter measurements to gain information about the MUT's dielectric properties. Therefore, SMA connectors were mounted onto the PCB to gain measurement access. The fabricated PCB is displayed in Fig. 4-14. On the right side in Fig. 4-14, the PCB layer stack is displayed. The stack is composed of an FR4 base material to support the ultra thin Rogers material in a lamination construction using a pre-impregnated material (prepreg) as interposer layer. The copper was structured with the help of a rapid PCB prototyping laser machine. The utilized SMD components have a 0402 type package to feature sufficient RF performance. S-parameter measurements were performed with a vector network analyzer for frequencies up to 8.5 GHz after short-open-load-thru (SOLT) calibration applying an electronic calibration module. The measurement results will be presented in section 4.3.

Previously in this chapter, the phase tuning approach to enhance the interferometer's performance has been discussed. The following subsection shows a convenient approach of proving both the superior performance of a phase-tuned device and the microstrip sensing

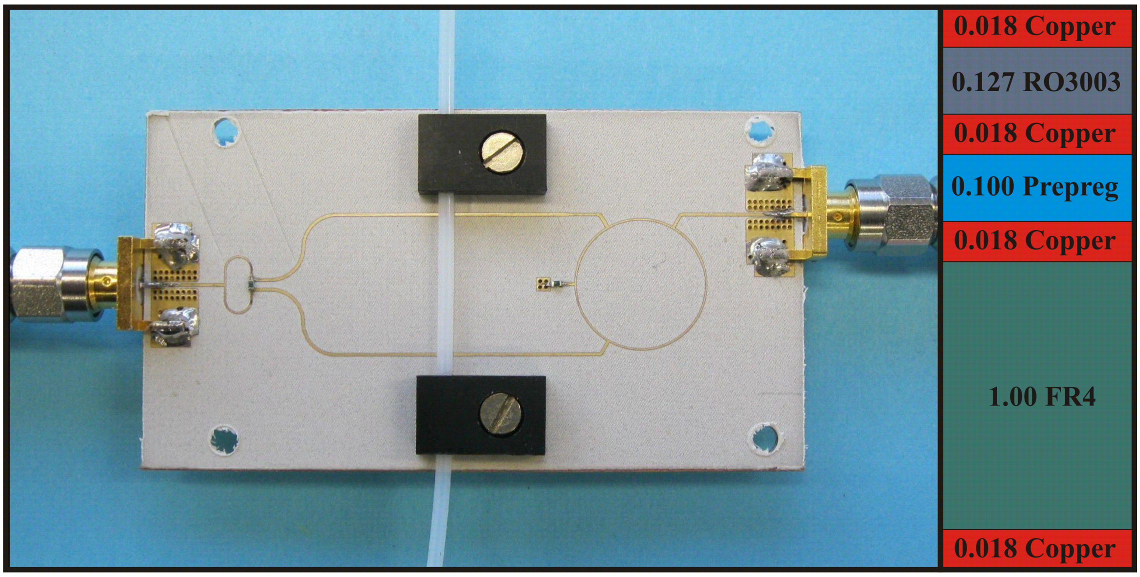

Figure 4-14: *Printed circuit board with microfluidic channel and SMA connectors and layer stack (units in* µm*).*

of overlay materials.

In section 2.4 it has been presented that a microstrip line's propagation behavior is affected by a material placed on top of it. The discussion in 3.3 about interferometers revealed that this concept is well suited for phase calibration techniques. To obtain a direct and easy method to change the length of the material covering the microstrip, a stepped object depicted in Fig. 4-15 made of synthetic resin bonded paper was fabricated enabling 5 discrete phase states. The first step has a length of 1.6 mm and each of the following steps

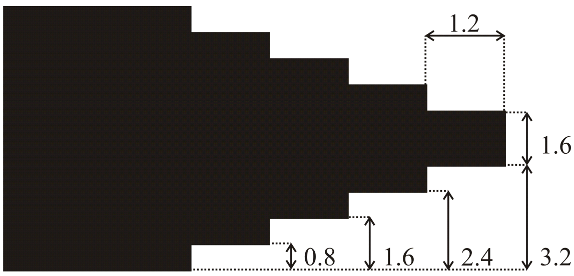

Figure 4-15: *Stepped object for phase manipulation of waves on microstrip lines.*

is 1.6 mm longer than the previous one. The width of each step is 1.2 mm, which is around 10 times the substrate thickness to avoid fringing effects. By adjusting the steps covering the microstrip, the length of the overlaying material and with it the signal phase can be varied. That way, the center frequency of the interferometer can be adjusted.

The sketched object was mounted on top of the bottom microstrip line of the interferometer and pressed on top of the PCB using a standard screw at a distance of 4.8 mm to the strip line to assure that the propagation behavior of the line is not manipulated by the metal screw. The resulting PCB is shown in Fig. 4-16. This very simple approach was used to gain a first proof of concept for phase tuning at microwave frequencies.

In practice, a very accurate positioning of the stepped object is necessary to achieve re-

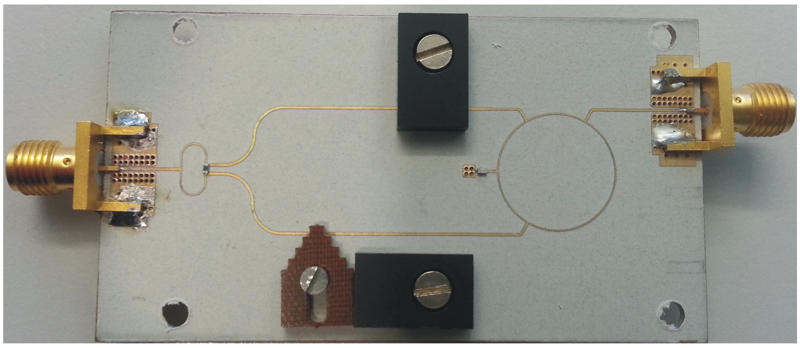

Figure 4-16: *Sensor for experimental phase calibration.*

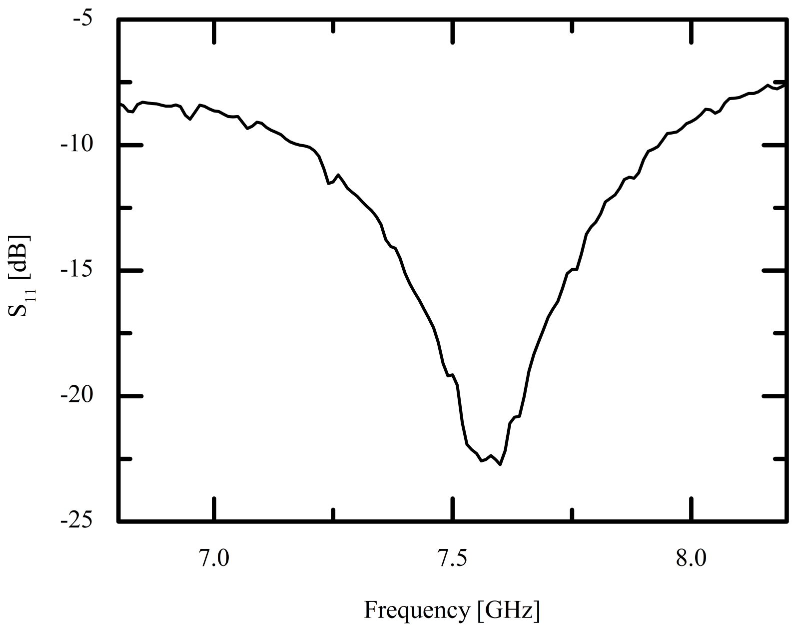

Figure 4-17: *Measurement of reflection S_{11} of the interferometer PCB.*

producible, discrete states of the propagated signal phase. In the presented experiment, the object was placed and adjusted by hand to find the position for minimal transmission S_{21} which is inherently associated with the highest possible Q-factor. Since the purpose was the proof of concept, it was abstained from further experiments with optimized positioning methods.

The results of both, the first design and the improved version of the microwave interferometer exhibiting a tapered section for loss compensation and phase tuning capability are presented in the following subsection.

4.3 Experimental Results

To investigate the performance of the interferometer experimentally, the sensor depicted in Fig. 4-14 was characterized by measuring S-parameters with a vector network analyzer. The input reflection represented by parameter S_{11} is shown in Fig. 4-17. The frequency for minimum reflection of -22 dBm is approximately at 7.6 GHz. Since the sensor's feature in focus is a high Q-factor and with that its sensitivity, the input matching was not a critical aspect and thus not further optimized. Additionally, the S_{21} minimum changes for different samples under test so that good matching needs to be provided for the complete frequency band of interest. Very good matching is still achieved at 7.44 GHz, the frequency for minimum transmission without exposing a sample to the sensor, with S_{11} =−16.5 dB.

As explained previously in this chapter, the S_{21} minimum does shift with samples of different ε_r. Therefore, the sensor was exposed to different fluids within the microfluidic channel while monitoring the transmission. In the first experiment, a yeast culture was grown in glucose as nutrient medium and measured in different stages. Because of a different biomass - a different number and density of cells - the permittivity of the sample changes. This can be quantified by applying the Rayleigh equation for dielectric properties of disperse mixtures assuming a spherical shaped disperse phase [86]. In the presented experiment, an emphasis has been put on creating a sample that changes its dielectric constant over time. Fig. 4-18 displays the measured transmission over frequency for different stages of cultivation with time as a parameter.

As it is shown, a difference of 125 MHz of the notch is obtained after 20 h of cultivation. After that duration, considering a cell doubling time of 90 min [87], one can assume no further increase in number of cells for the regarded volumes. With a progressed cultivation, the center frequency shifts down to lower frequencies, indicating a higher ε_r. One of the reasons for that is a higher number of yeast cells in the sample, having a higher real part of the dielectric constant compared to glucose. A drawback of the presented experiment is that the yeast glucose solution was kept in the microfluidic channel without extra preparation or cell extraction. That means that a dynamic growth progress was recorded and the measured behavior is an accumulation of several effects related to metabolic processes, for example the fermentation of ethanol as well as a varying cell concentration. Another side product emerging in a yeast cultivation progress is nitrogen [88]. The result is a much higher change in permittivity leading to the bigger frequency shift in the S_{21}

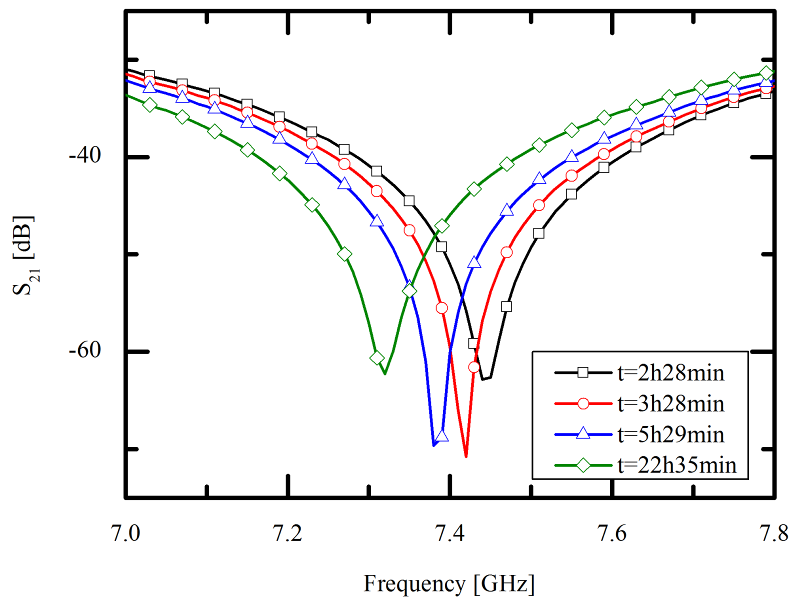

Figure 4-18: *Transmission S_{21} of the interferometer PCB with yeast.*

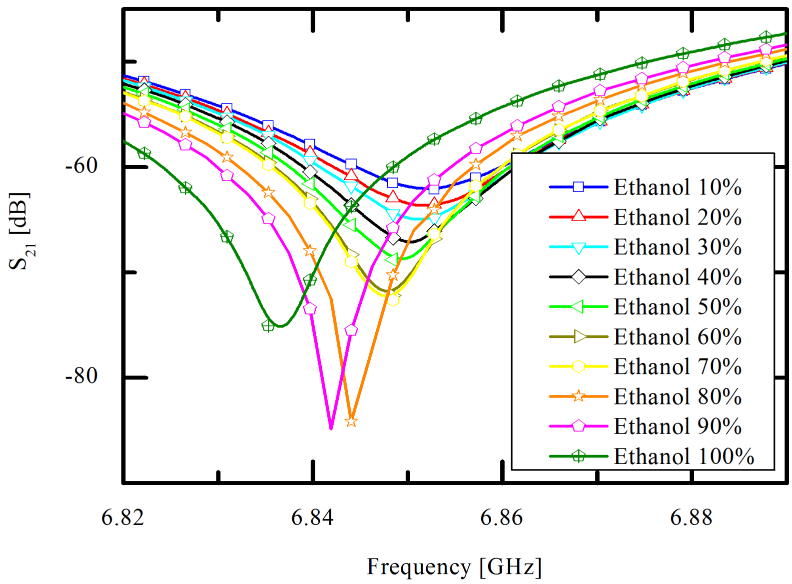

Figure 4-19: *Transmission S_{21} of the interferometer PCB for 10 to 100 percent ethanol sample.*

notch as depicted in Fig. 4-18.

To study the impact of the optimization techniques explained before, the sensor setup from Fig. 4-16 was used for the following experiments. As a reference liquid an ethanol-water-mixture was used, since its dielectric properties are often studied in literature and well documented [89]. Moreover, it can be adjusted by using a different composition of water and ethanol fractions. The liquid was exposed to the sensor in a microfluidic channel that was mounted on top of the PCB as depicted in Fig 4-14. For the demonstrated experiments, a polytetrafluoroethylene (PTFE) tube with an inner diameter of 0.5 mm was used to confine the liquids under test. The sample volume that is relevant for the measurements is around 570 nL since this is the volume covering the microstrip with a sufficient margin without causing fringing effects. For the considered tube, this volume fills the tube for a length of 2.84 mm. The calibration object displayed in Fig. 4-15 was used to calibrate the sensor. The calibration process was conducted using one particular sample for a reference measurement before characterizing the other dielectric samples. The PTFE channel contains the liquid under test that is intended to be investigated. Fig. 4-19 shows the measured transmission S_{21} for 10-100 % ethanol in water. Calibration of the interferometer was carried out while pure ethanol was positioned in the microfluidic channel. Fig. 4-19 displays that the frequency of the S_{21} notch is shifted down with increasing volume percent of ethanol within the ethanol-water mixture. This means the frequency shift of the notch gives information about the concentration of ethanol in the mixture. To evaluate the measured behavior, the center frequency was plotted versus the respective ethanol concentration. The result is displayed in Fig. 4-20. The graph shows a constant center frequency for some of the ethanol concentration steps. This stems from a limited resolution of the S-parameter measurement results depicted in Fig. 4-19. It is important to state that the change of the notch frequency increases with increasing ethanol concentration. This is due to the fact that the calibration procedure was applied for a 100 % ethanol sample and with increasing concentration the sensor state approaches

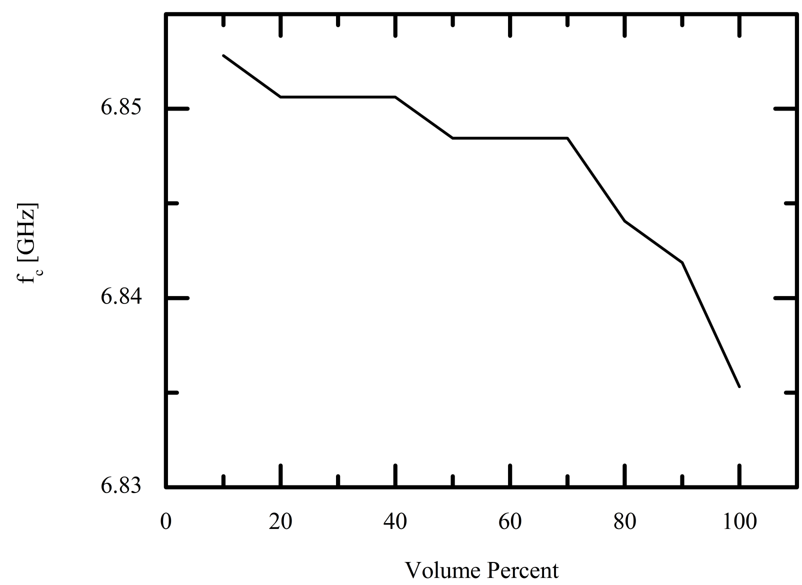

Figure 4-20: *Center frequency of transmission S_{21} versus volume fraction of ethanol.*

the reference state. As it is shown in Fig. 4-20, the highest sensitivity is as expected close to that state. In [90] and [91], values for the real part of the permittivity of water-ethanol mixtures are published. Calculations based on these values show that the sensor exhibits an overall frequency shift of 18 MHz for a change of 48 in the dielectric constant.

Comparing the results obtained with the calibrated and uncalibrated sensor from Figs. 4-18 and 4-19, it is observed that the matching of the reference and the measurement path is increased by 10 dB, indicated by the lower notch power level. This is increasing the potential resolution achievable with the presented approach. The design was adapted to test this phase calibration approach by introducing a commercial phase shifter, which can be tuned continuously by changing an analog voltage. Another change that has been made concerns the sensor line itself. In [76], the sensitivity of line sensors based on their field distribution when screening a sample under test, has been investigated with the result, that a coplanar wave guide shows the highest sensitivity against dielectric changes in the cover material. This is stemming from the fact that for a CPW line, the field penetrates a higher volume of the investigated sample. The PCB that was designed to confirm that effect is depicted in Fig. 4-21. The layout of the passive components is identical to the initial version. Changes compared to the previous PCB are that sensing lines are implemented as CPW lines and the Hittite phase shifters featuring operational frequencies from 2-20 GHz and an insertion loss of 4 dB. Furthermore, continuous phase tuning up to 180° is enabled. The sensor was measured and the phase shifters have been adjusted to achieve optimum path matching of the reference and measurement path, which is reflected in the minimum S_{21} notch. The result for that state is depicted in Fig. 4-22. It shows that the minimum S_{21} notch is now shifted down to power levels of below -100 dB. This was achieved by tuning the S_{21} center frequency to higher values, where the amplitudes of both paths, upper and lower arm of the hybrid ring coupler, are equal hence leading to lower possible S_{21} levels as explained in section 3.4. Comparing the center frequency of minimum transmission to the value obtained from S_{21} simulations displayed in Fig. 4-7, it is observed that the simulated value is exactly hit with the experimental setup. The

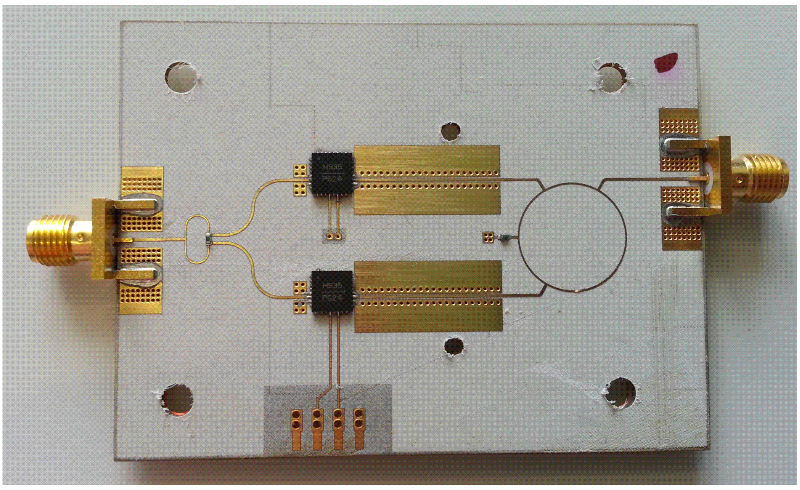

Figure 4-21: *Improved Sensor PCB with phase shifters and CPW sensing lines.*

insertion of phase shifters does not affect the hybrid ring coupler's performance, meaning that the position of the absolute minimum in the frequency band stays the same. The phase shifters enable tuning the interferometer to that particular point to exploit the highest Q and minimum S21 available from the given hybrid ring coupler. The minimum position of 7.5 GHz was simulated and the measured value is 7.4 GHz, which is a difference of 1.3 %. The measurements with the PCB depicted in Fig. 4-21 showed that the Q-factor of the interferometer could be improved tremendously. The quality factor of S_{21} in Fig. 4-21 is about 15 000. Without phase shifters, a Q of maximum 500 could be achieved.

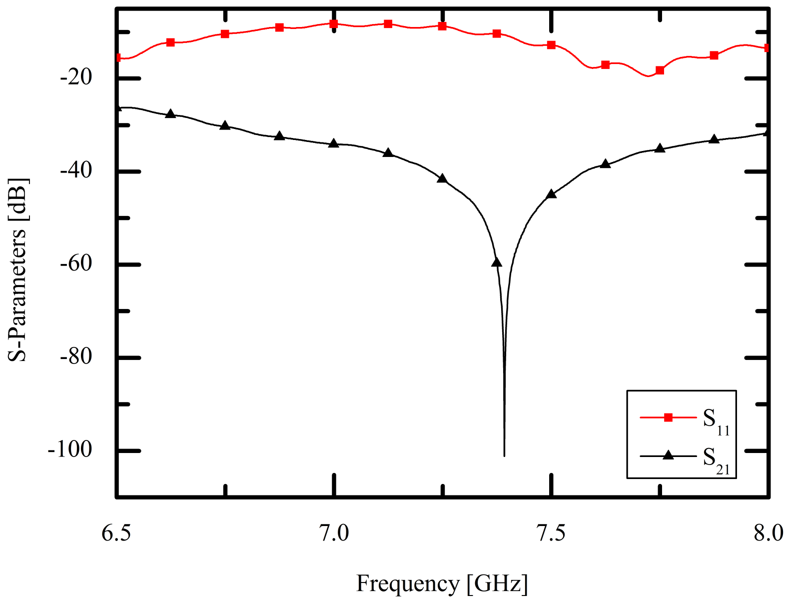

Figure 4-22: *S-parameter measurements of the improved interferometer PCB.*

4.4 Summary

This chapter demonstrated that with the help of microstrip line sensors, dielectric samples can be efficiently characterized by combining the microstrip sensing approach discussed in section 2.4 and the interferometer read-out concept. The passive microwave circuits were developed in several iterations starting from line characteristics obtained analytically using ADS LineCalc. Optimization procedures based on EM simulations were applied resulting in passive microwave circuits and finally in a microwave interferometer working around 7 GHz. The design was implemented on an RF Rogers 3003 material to proof the theoretical investigations from previous chapters experimentally. For that purpose, experiments with a yeast culture confined in a microfluidic channel were performed to investigate a sample fluid with varying dielectric properties over time. For further investigations of the interferometer, calibration liquids were applied. S-parameter measurements could demonstrate the sensor's response to different dielectric samples. The symmetrical transmission behavior of the reference and the measurement microstrip lines could be improved by more than 10 dB using the proposed phase-tuning method by covering a distinct length of the microstrip with a dielectric overlay. This is improving the potential resolution depending on the read-out method. A second approach for sensitivity enhancement was presented, where the path length difference of the sensing and the measurement path was compensated by tapering a part of the line. Using that technique, the propagation of both the reference and the measurement path could be equalized in terms of amplitude, resulting in a much steeper overall S_{21} notch.

To provide continuous tuning of the microstrip phase, a third approach using Hittite phase shifters was implemented and measured. A minimum S_{21} below -100 dB was experimentally recorded. Additionally, the simulated and calculated result, that a much lower absolute minimum can be achieved for a frequency close to the center frequency, was confirmed by measurements. At that particular frequency, both branches of the hybrid ring coupler feature the same insertion loss so that a perfect matching of reference and measurement path leads to the very deep notch level. Further simulations could show that the sensor sensitivity is inherently increased by scaling the circuitry to higher frequencies of operation. The collective results demonstrated in this chapter are motivating the implementation of millimeter-wave interferometers featuring phase calibration for dielectric characterization of biomedical samples. The design and testing of an on-chip interferometer will be presented in chapter 6. Before, further investigations of dielectric sample characterization at very high frequencies in the millimeter-wave range up to terahertz signals will be presented in chapter 5.

5 Millimeter-Wave Permittivity Measurements

In biomedical applications, the dimensions of the developed systems are usually crucial and miniaturization is highly desired. From an IC design point of view, the dimensions can be reduced by scaling the structure using higher frequencies within the millimeter-wave band, since most of the passive circuits' dimensions are depending on the wave-length. The problem of using high frequency signals is the increased attenuation and decreased penetration depth into liquid samples [75, 92, 93] so that the advantage or applicability of millimeter-waves to screen bio samples needs to be thoroughly investigated. Before starting a high frequency design, further investigations using existing laboratory equipment are conducted to obtain a proof of concept and investigate the theoretical potential of the high frequency bands. Using a continuous wave terahertz interferometer from Toptica [94], which is based on the interferometer principle, it is possible to generate signals at frequencies between 60 GHz and 1800 GHz. These are transmitted through MUTs. The interferometer device enables observing the signal attenuation and phase of both, reflected and transmitted waves. Section 5.1 discusses the theory of dispersion of bio-material. Afterwards, the principle function of the interferometer is presented in section 5.2. Experiments for proof of concept have been conducted and will be demonstrated in section 5.3. In section 5.4, processes at 120 GHz are explored with an on-chip biosensor. Section 5.5 gives conclusions and finally, section 5.6 sums up this chapter.

5.1 Theory

Considering the target applications mentioned in chapter 1 for the circuits addressed in this thesis, it is very important to investigate the dielectric behavior of water, since water is the main ingredient in bio materials of interest. The permittivity of water shows dispersive behavior over frequency that has been vastly studied in literature [95–97]. The most common model to describe this effect is the Cole-Cole plot [98,99]. It is an extended model of the Debye dispersion. Investigations on the accuracy of this model can be found [62, 100] in literature. Results attest for a high accuracy of the model showing low deviations from measured permittivity. The equations describing the complex dielectric constant, split into the real and imaginary part as follows:

$$\varepsilon' = \varepsilon_\infty + (\varepsilon_S - \varepsilon_\infty)\frac{1 + (\omega\tau)^{(1-\alpha)}\sin(\alpha\pi/2)}{1 + 2(\omega\tau)^{(1-\alpha)}\sin(\alpha\pi/2) + (\omega\tau)^{2(1-\alpha)}} \tag{5-1}$$

and

$$\varepsilon'' = \frac{(\varepsilon_S - \varepsilon_\infty)(\omega\tau)^{(1-\alpha)}\cos(\alpha\pi/2)}{1 + 2(\omega\tau)^{(1-\alpha)}\sin(\alpha\pi/2) + (\omega\tau)^{2(1-\alpha)}} \tag{5-2}$$

Here, ε_S is the static dielectric constant, ε_∞ the dielectric constant for very high frequencies where molecules can not follow an external electrical field anymore and no energy is dissipated inside the dielectric anymore. The exponent parameter α with a value range from 0 to 1, is a fitting parameter for different spectral shapes. When α is zero, the

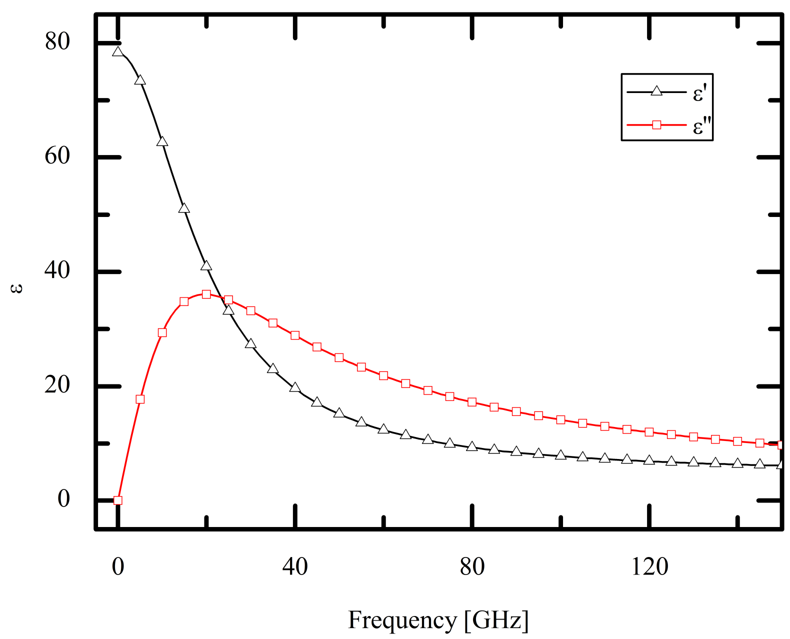

Figure 5-1: *Cole-Cole plot: Real and imaginary part of water permittivity.*

Cole-Cole equations reduce to the Debye model. ω is the angular frequency and τ a time constant representing the relaxation. Identifying the required parameters from literature, the equation was applied to obtain the graph in Fig. 5-1. The static dielectric constant of water was studied by Malmberg and Maryott [101] for different temperatures. The plot in 5-1 is valid for a temperature of 25° resulting in a static dielectric constant of 78.3. The best fitting parameter $\alpha = 0.014$ was obtained from [62]. Fig. 5-1 shows that the imaginary part of the dielectric constant reaches a maximum around 20 GHz, meaning that the highest dielectric losses are occurring for signals at that frequency. The real part is monotonically decreasing with frequency. One advantage of operating at very high frequencies is that the material characteristics become more stable and the dispersion is reaching the high frequency permittivity limit.

Since one objective of this thesis is the characterization of cultivation stadiums based on the cell number in a certain carrier solution, the contribution of cells to the overall permittivity of a liquid is studied and modeled. The methodology starts with the calculation of the permittivity of single cells based on a two-shell model [102–104]. The parameter values needed for the two-shell model including shell capacitance and conductivity of the cytoplasmic membrane for yeast cells, was obtained from [105]. The dispersion of that permittivity is again modeled using a Cole-Cole estimation. The static dielectric constant of glucose solutions, relevant for the yeast experiments that will be discussed in this chapter, are close to the value of pure water [106]. Based on research published by Maxwell [107] and Wagner [26], the permittivity of a binary mixture containing spherical elements, in this case yeast cells, is calculated using the following equation:

$$\varepsilon_{sus} = \varepsilon_c \frac{(1 + 2C_V)\varepsilon_y + 2(1 - C_V)\varepsilon_c}{(1 - C_V)\varepsilon_y + (2 + 2C_V)\varepsilon_c} \tag{5-3}$$

In (5-3), ε_c is the permittivity of the carrier liquid, ε_y the one of yeast and C_V denotes the volume concentration of yeast inside the carrier liquid, which is here a glucose water

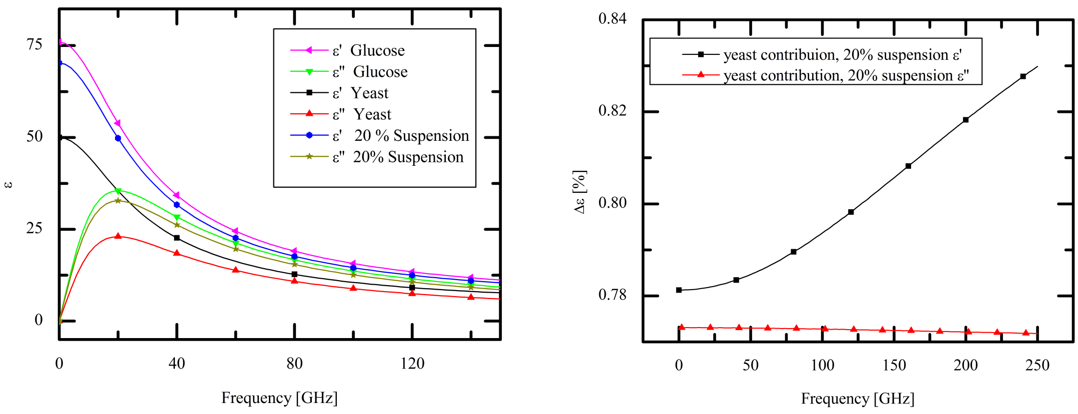

(a) *Dielectric constant of 20% glucose suspension and its ingredients.* (b) *Relative impact of yeast onto overall dielectric constant.*

Figure 5-2: *Calculated dielectric properties of yeast glucose suspensions.*

solution. All permittivity parameters are complex, frequency dependent values, in order to calculate both the permittivity over frequency and the theoretical relative impact of cells onto the overall permittivity from those results. Fig. 5-2 depicts two figures, one displaying the dielectric constants of a 20 % yeast glucose suspension and the other showing the impact of a 20 % solution of yeast in glucose derived by applying the explained procedure. It is demonstrated that the relative impact of the cells is increased with frequency. Along with potentially ultra compact integrated devices, this motivates the implementation of cell counters at millimeter-wave frequencies. Further experiments will be presented within this chapter to confirm that theory. The band 121 GHz-122 GHz is of particular interest, since it is one of the industrial, scientific and medical (ISM) bands, reserved internationally for applications which are not associated with telecommunication.

5.2 Continuous-Wave Interferometer

The basic principle of the interferometer is depicted in Fig. 5-3. The source of it is a twin distributed feedback laser (DFB), tunable by temperature manipulation. The laser sources exhibit a center wavelength of 855 nm and a maximum output power of 130 mW. The wavelength of the beam generated by the device is depending on the temperature almost linearly. The two laser sources are tuned independently to intentionally create a frequency offset between the two signals. Accurate frequency tuning of each laser is achieved by combining 855 nm DFB diode technology and precise interferometric frequency control using a low- finesse Fabry–Pérot etalon in a feedback loop to stabilize the laser frequency. This allows to precisely adjust frequency values within the diode's tuning range, with high resolution of about 1 MHz [108]. The signals of both lasers are superimposed by fiber-optic beam combination, split up equally and fed to one receiving and another transmitting photomixer. The devices are consisting of low temperature grown (LTG) GaAs finger photomixers on a 350 µm semi-insulating GaAs substrate, a 100 nm GaAs buffer layer, and a 400 nm $Al_{0.4}Ga_{0.6}As$ layer [108]. The mixer is providing a signal at its output exhibiting a frequency that is the difference of the two laser signals. It radiates by using a

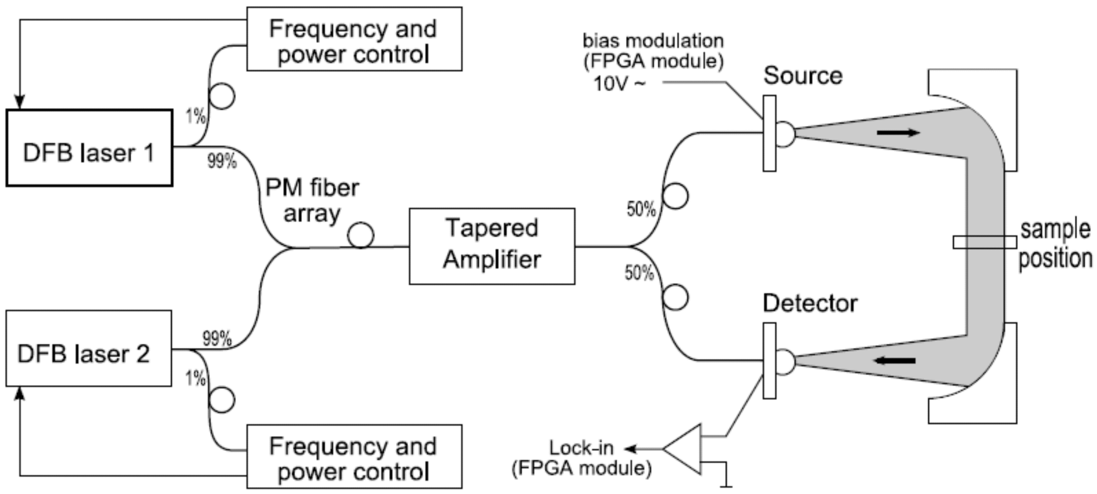

Figure 5-3: *Continuous wave terahertz interferometer principle [94].*

log-periodic antenna coupling the terahertz signal into free space applying a silicon lens. It is followed by a parabolic mirror with a focal length of 75 mm collimating the emitted terahertz beam. Signal routing is accomplished using polarization-maintaining (PM). The two photomixers are part of the interferometer, that is used to redirect the beam following a certain trajectory leading from the transmitter to the receiver. For high precision signal detection, a lock-in technique is applied, where the signal is modulated at the transmitter and demodulated at the receiver, using a lock-in amplifier. This allows to detect signals even at high noise levels [109]. The measured parameter is the output photo current of the receiving photo mixer. It can be described by the following equation:

$$I_{PH} \propto E_{THz} \cos \Delta\varphi = E_{THz} \cos (2\pi \Delta L f / c) \tag{5-4}$$

E_{THz} is the amplitude of the terahertz electric field, f the terahertz frequency, c the speed of light in vacuum and ΔL the path difference between transmitted and received signal of the interferometer, resulting in a phase shift $\Delta\varphi$. The path difference can be expressed as follows:

$$\Delta L = L_S + L_{THz} - L_D \tag{5-5}$$

It is the difference between the optical path L_D traveled by the laser beat to the detector, on the one hand, and the optical path L_S of the laser beat to the terahertz source plus the terahertz path L_{THz} from the source to the detector, on the other. [94] provides a detailed description. The two parameters obtained by these measurements giving information about materials that are penetrated by the terahertz beam, are the amplitude of the photocurrent and the interference pattern. To clarify the relevant parameters, Fig 5-4 shows an example of a measured photocurrent presented in [94]. Both amplitude and phase information can be derived. The period $\Delta\nu$ of the interference pattern depends on the optical path difference ΔL. In the presented example $\Delta\nu = 1.5$ GHz and $\Delta L = 0.2$ m. The water absorption line around 557 GHz suppresses the terahertz signal, which is also reflected in the measured photocurrent depicted in Fig. 5-4. The amplitude carries information about the attenuation caused by loss mechanisms inside the material. It can be obtained by calculating the envelope of the measured photocurrent.

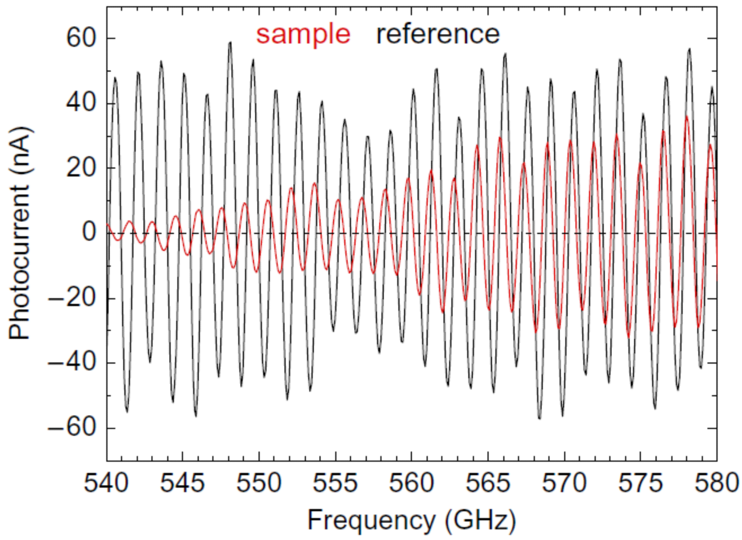

Figure 5-4: *Example terahertz photocurrent with and without lactose sample [94].*

The optical path difference determines the interference pattern and the maximums are equally spaced in frequency with the order m for a constant phase velocity according to the following equation:

$$\nu_{max,m} = m\frac{c}{\Delta L} \tag{5-6}$$

When a material under investigation is inserted into the terahertz beam, the electrical path length is changed, effecting ΔL. Hence, the refractive index of the material can be extracted by evaluating the interference pattern, comparing it to a reference material, which is usually air. This requires the exact knowledge of the interferometer geometry and dimensions. The following equation expresses the described relations:

$$(n - n_{air})d = \left(\frac{\nu_{max,m}^{ref}}{\nu_{max,m}^{sample}} - 1\right)\Delta L^{ref} \tag{5-7}$$

In the equation, d is the sample thickness, $\nu_{max,m}^{ref}$ and $\nu_{max,m}^{sample}$ are the respective frequencies of the maximums of order m of the reference and the sample obtained by measurements. n is the refractive index.

To fully characterize the sample under test, it is also necessary to measure the transmission, compare it to a reference and calculate the amount of energy absorbed by the respective material. Comparing the envelope of two measurements, sample and reference, the transmittance is obtained by applying the following equation:

$$T = \frac{I_{ph}^{sample}}{I_{ph}^{ref}} \tag{5-8}$$

It is utilized for experimental determination of the attenuation of a material under test by comparing the measured photo current with and without sample. The following deductions shall illustrate the method of permittivity calculation based on the measured refractive index and the transmittance. When the transmittance and the refractive index are known by measurements and calculations presented previously in this section, the following set of equations is fully determined and is employable to attain the complex dielectric constant as follows:

$$T = \frac{(1 - R)^2 \exp(-\alpha d)}{1 - R\exp(-\alpha d)^2 + 4R\exp(-\alpha d) sin^2(n\omega c/d)} \tag{5-9}$$

Here, the absorption α is defined as follows:

$$\alpha = 2k\omega/c \tag{5-10}$$

The reflectance R can be calculated to be:

$$R = \frac{(n - 1)^2 + k^2}{(n + 1)^2 + k^2} \tag{5-11}$$

Equations (5-9), (5-10) and (5-11) are providing the basis for calculating the extinction coefficient k. Along with the determined refractive index, ε_1 and ε_2 are obtained with the following relations.

$$\varepsilon' = n^2 - k^2 \tag{5-12}$$

$$\varepsilon'' = 2nk \tag{5-13}$$

The precision and feasibility of that procedure, along with the results, were evaluated in [94] for the example of α-lactose monohydrate. The following section presents the experiments relevant to this work that have been pursued with the interferometer.

5.3 CW Experiments

One of the target applications of the electrical interferometers designed in this thesis is the characterization of the cultivation stadium of microorganisms. The increased number of cells in a culture sample is reflected by the average permittivity of the medium and can thus be detected by radio frequency and terahertz spectroscopy. The following investigations were conducted to study the feasibility of permittivity indicated culture stadium analysis.

5.3.1 Experimental Setup

The main element in the experimental setup is the Toptica continuous wave interferometer, see Fig. 5-5 for a picture of the interferometer device. The challenge was to bring the sample under investigation into the terahertz beam and allow it to transmit through. The opening at the bottom in Fig. 5-5 is the access point, where samples can be inserted. Stemming from the method presented in [110], where the samples are stored and processed in PTFE pipes, a 1.5 mm in diameter PTFE tube was chosen to contain the liquid

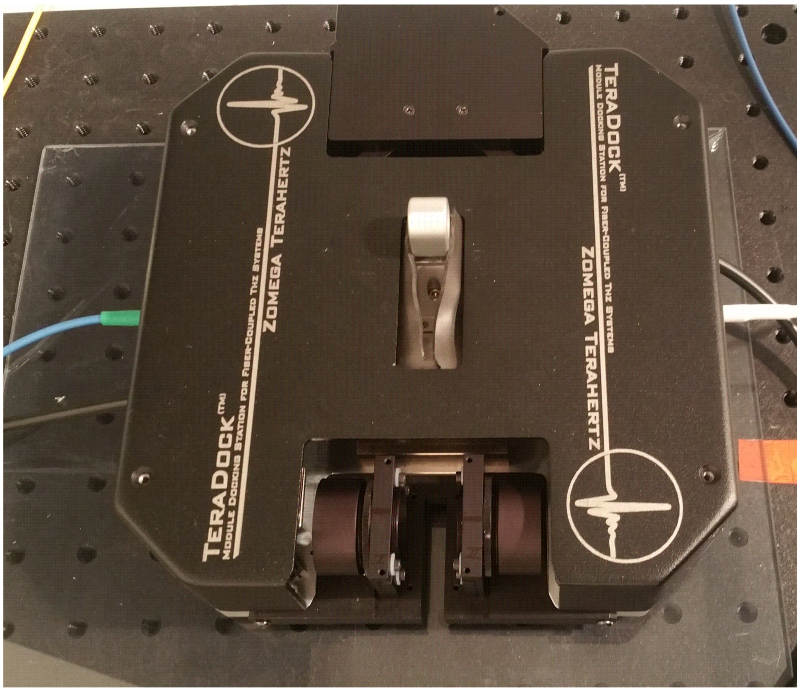

Figure 5-5: *Picture of the continuous wave interferometer.*

sample. As a test case, different kinds of baker's yeast have been chosen, making cell growth procedures easy and handling convenient. A sample holder for this tube was constructed. It is depicted in Fig. 5-6. It fits the interferometer opening depicted in Fig. 5-5. Along with the components described in 5.3.1 it was used for millimeter-wave to terahertz measurements. The results are presented in the following section.

5.3.2 Measurement Results

First measurement results, displayed in Fig. 5-7, show the phase versus time of cultivation of a sample yeast culture for 3 chosen frequencies. The measured characteristics deviate

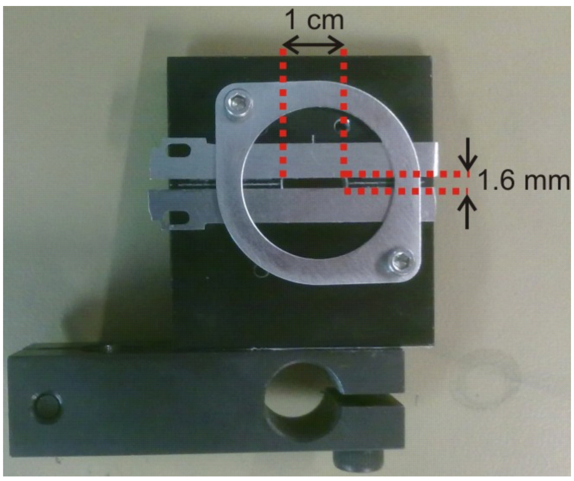

Figure 5-6: *Sample holder for PTFE tubes, mountable on an optical board.*

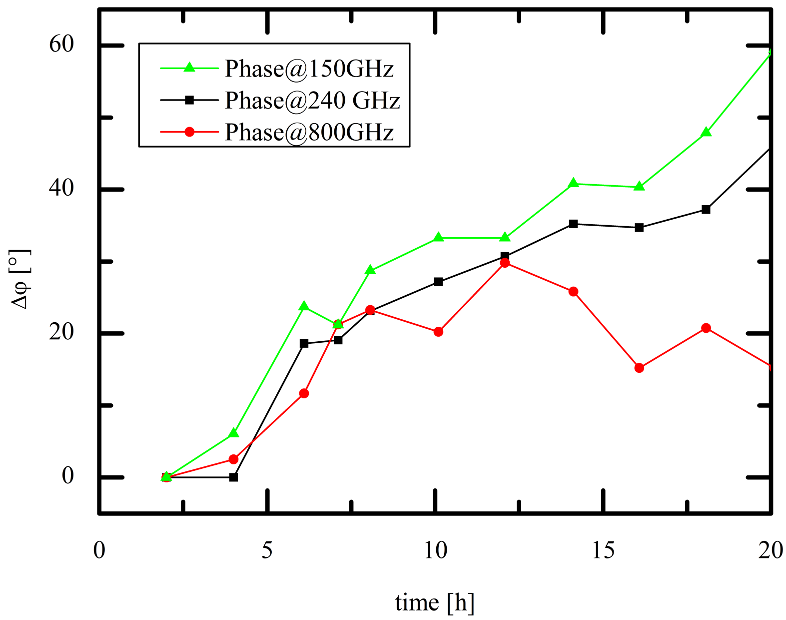

Figure 5-7: *Signal phase versus cultivation time.*

from the expected behavior, since a higher frequency should inherently show a higher phase change with permittivity variation. When the reference sample for phase determination is chosen to be air, the expected dependency of the phase frequency correlation is calculated as follows:

$$\Delta\varphi = \varphi_S - \varphi_{ref} = f\frac{d_{in}}{c}(\sqrt{\varepsilon_s} - \sqrt{\varepsilon_{ref}}) \tag{5-14}$$

It describes the phase change $\Delta\varphi$ with respect to the sample length d_{in} and the relative permittivities of the reference medium ε_{ref}, usually air, and the MUT ε_s. c is the speed of light in vacuum and f the frequency. Fig. 5-8 shows the relevant parameters for (5-14). The parameter α denotes the attenuation constant for the respective material, β the phase constant and λ the phase length inside the medium. The dimensions are given by d_{Tube}, the wall thickness of the tube and the inner diameter d_{in}. According to

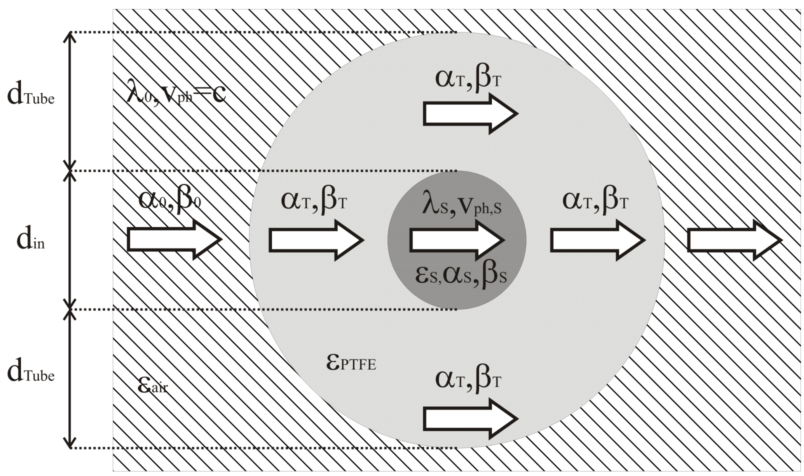

Figure 5-8: *Propagation scenario for a sample in the terahertz beam.*

(5-14), the impact on the phase should be proportional to the frequency of operation, when dispersion is neglected. The conclusion that is drawn from these investigations is that a major part of the radiated energy is passing by the sample under investigation through the wall of the PTFE tube, leaving the influence of the sample significantly reduced. Figure 5-8 sketches the discussed scenario. The dielectric properties of the PTFE wall remain constant over frequency, so that a simple unwanted offset is added decreasing the sensitivity. Losses caused by the liquid inside the tube are increased with frequency, enforcing that effect further. Measurements showed that the phase progression monitored with the interferometer was decreased for an increase in frequency, as depicted in Fig. 5-7. To avoid that issue, an aperture was applied, to allow only transmission through the sample and reflect all other radiation besides the sample. Its dimensions and shape is illustrated in Fig. 5-9. The subsequent results have been obtained with the discussed

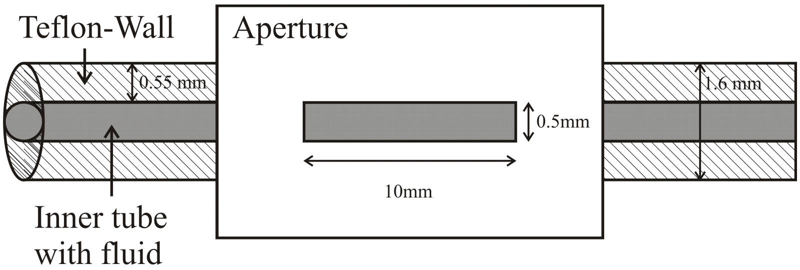

Figure 5-9: *Aperture for shielding the PTFE wall.*

experimental setup.

After propagating through the sample, the signal is detected by a photomixer and a lock-in detector so that the measured parameter is a photo current. Fig. 5-10 presents the measured envelope of the output photo current for different samples: tetradecane, glucose, air and a yeast glucose suspension after 16 h of cultivation. The highest transmission was detected for the samples tetradecane and air. This was expected, since they feature the

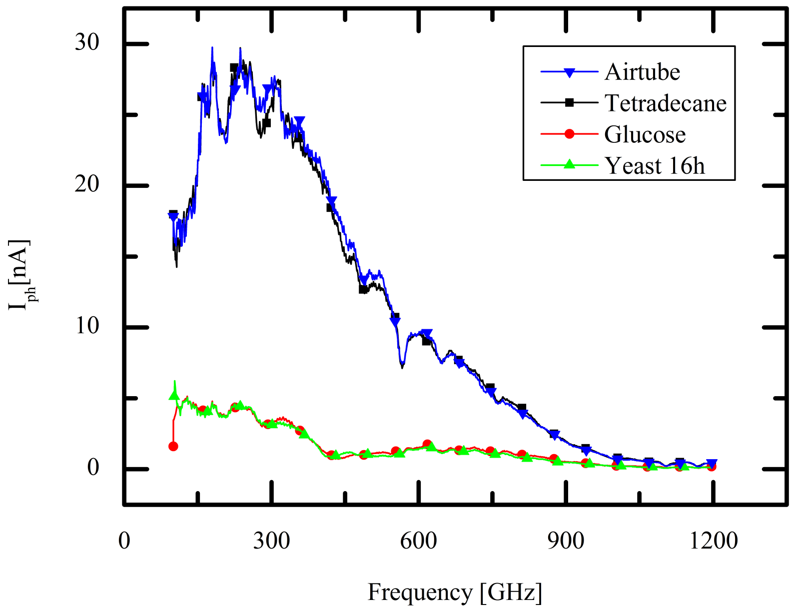

Figure 5-10: *Envelope of the photo current obtained with the terahertz interferometer.*

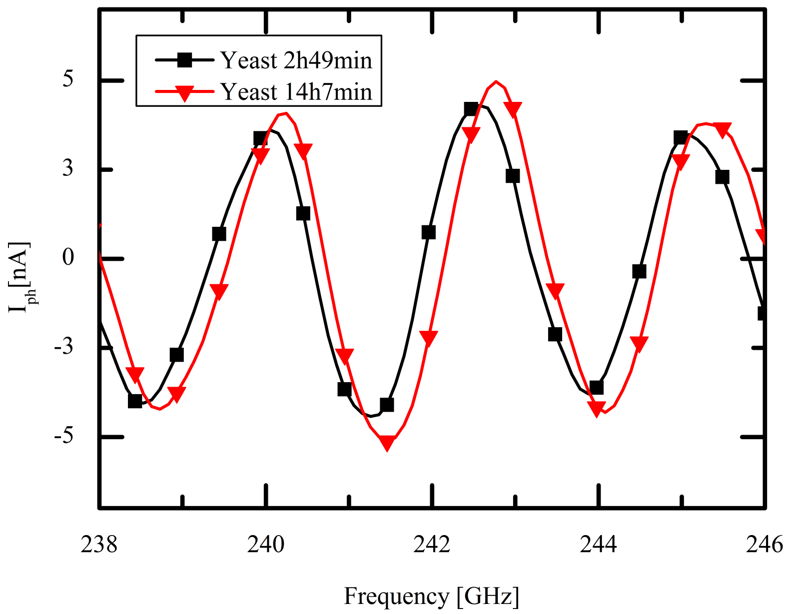

Figure 5-11: *Raw data of the photo current obtained with the terahertz interferometer.*

lowest dielectric losses compared to aqueous solutions. The results confirm again the assumption that a major part of the radiated power was transmitted through the teflon walls before mounting the aperture since the maximum photocurrent of approximately 30 nA has decreased to 30 % compared to measurements without. Fig. 5-10 clarifies that glucose and yeast can be reliably differentiated from air and tetradecane. However, the evaluation of the amplitude does not allow differentiating between glucose and yeast, the most relevant components in our sample. The results indicate that the dielectric loss in suspensions of glucose and yeast cells does not change significantly based on the cell number so that the imaginary part of the dielectric sample is changed only slightly. The results were evaluated further to experiment on the real part of the liquids under test, in particular yeast cultures in different stadiums of cultivation. It requires the signal phase to be extracted from the measurement results. The photo current for a yeast-glucose suspension for 3 and 14 hours cultivation time is depicted in Fig. 5-11. The phase has been extracted from those measurement results and Fig. 5-12 shows the phase change of the photo current versus cultivation time. It was derived from the zero-crossings of the signal depicted in Fig. 5-11. One can see that a phase difference of almost 35° is reached after 14 h cultivation time, allowing a reliable characterization of cultivation progression.

Further evaluation of conducted experiments revealed that a high sensitivity at frequencies beyond 100 GHz of $\Delta\varphi/t_c = 2.6\,°/\mathrm{h}$ is possible to achieve. Along with the advantage of potentially compact sensor structures, this makes an exploitation of those particular frequencies highly attractive for bio sensing applications. Furthermore, in terms of license issues and frequency regulations, ISM bands are very attractive for sensing applications at millimeter-wave frequencies. The following section presents experiments in the 120 GHz ISM band.

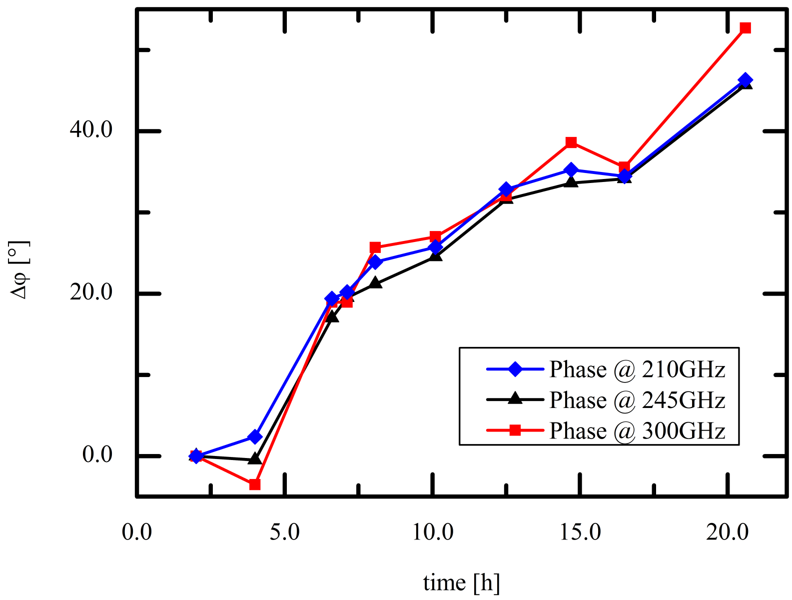

Figure 5-12: *Phase of the photo current extracted from zero crossings in the frequency domain.*

5.4 Investigation of 120 GHz Dielectric Measurements

Further experiments to explore specifically the band around 120 GHz were conducted with an on-chip dielectric sensing system using a transducer structure for dielectric measurements. The design of the transducer IC was not part of this thesis. The following sections present the experimental setup and the obtained measurement results

5.4.1 Experimental Setup

The passive sensor element is a coplanar stripline (CPS) bandpass filter [111] consisting of a combination of short-ended T-stubs placed inside a CPS transmission line. The high quality factor of this bandpass filter is achieved by the combined effects of using edge-coupled lines and removing the substrate beneath the transducer by silicon backside etching. The latter eliminates the loss contributions caused by substrate beneath the lines. At the edges of the design, some energy is still coupled to the remaining substrate around the device so that fringing effects are still present. Still, the overall effect of substrate loss is significantly reduced, which is reflected in the Q-factor. The silicon substrate beneath the transducer was etched to form a rectangular shaped hole up to the dielectric layer beneath the metal stack. The dimensions of the filter, line width and spacing, are designed for optimum transfer characteristics considering quasi TEM mode waves and to achieve a differential impedance of 100 Ω. Fig. 5-13 shows a photo of the resulting layout.

For on-chip characterization of dielectric samples, the following setup was applied. The sensor chip, sketched in Fig. 5-14, contains a 120 GHz push-push VCO with a buffer, the 120 GHz transducer, and a square law power detector. The oscillator core of the VCO consists of two sub-oscillators in common-collector topology [112]. The 120 GHz

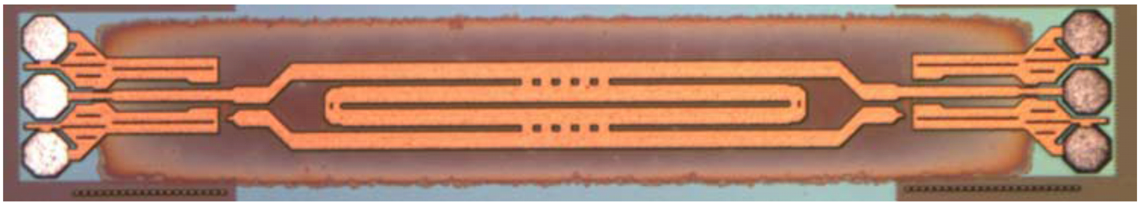

Figure 5-13: *Photograph of the single-ended 120 GHz transducer chip. [16].*

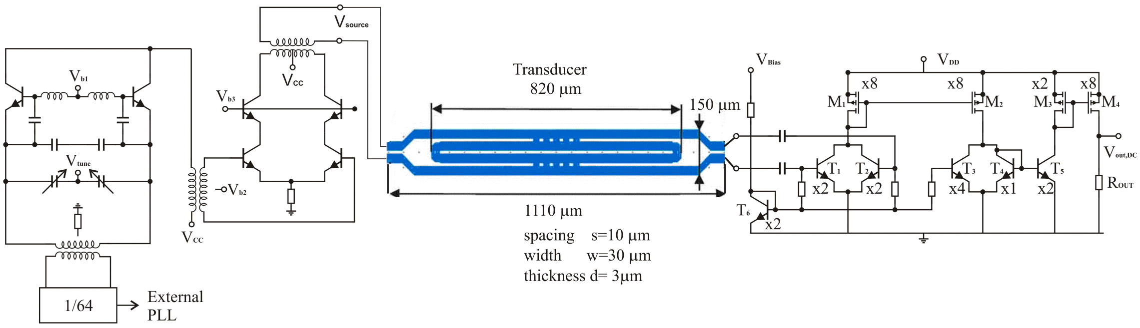

Figure 5-14: *Schematic of 120 GHz biosensor [16].*

signal of the VCO is fed to the transducer using transformer coupling and a buffer stage, providing the required matching to the transducer. The tuning of the VCO ranges from 117 GHz to 127 GHz. The output power of the transducer is sampled using the power detector, which provides a DC output proportional to the differential output signal power of the transducer. The power detector input is matched to the transducer using microstrip line segments. Fig. 5-13 shows the chip photo of the CPS transducer including pads for single-ended S-parameter measurements. Fig. 5-14 presents the schematic of the 120 GHz biosensor. To enable external PLL stabilizing, an on-chip 1/32 frequency divider for the fundamental signal of the VCO is integrated and the divided signal is routed to output pads. The results obtained using the described architecture will be discussed in section 5.4.2.

Additional experiments with the transducer chip have been conducted as part of this thesis to investigate the permittivity related transfer function of the chip. To confine the test liquids, a quartz capillary was chosen with an ultra thin wall of approximately 10 µm and an inner diameter of 500 µm. The capillaries were positioned on top of the chip and the thin walls allow for the samples to be in close proximity to the sensor. Fig. 5-15a depicts the explained setting and Fig. 5-15b displays a zoom in on the capillary on top of the chip. The figure displays three dies mounted on a PCB. Two of them carry a capillary and one doesn't. The chip without a capillary is serving as a reference, the next one has an empty capillary on top, also serving as a second reference and the third chip is intended for permittivity measurements of liquids. The capillary is attached to a PTFE tube, which is part of a microfluidic system, for example the segmented flow system presented in [110]. Both of the chip sets presented in this section have been used for permittivity detection using dielectric samples. The results are presented in the following.

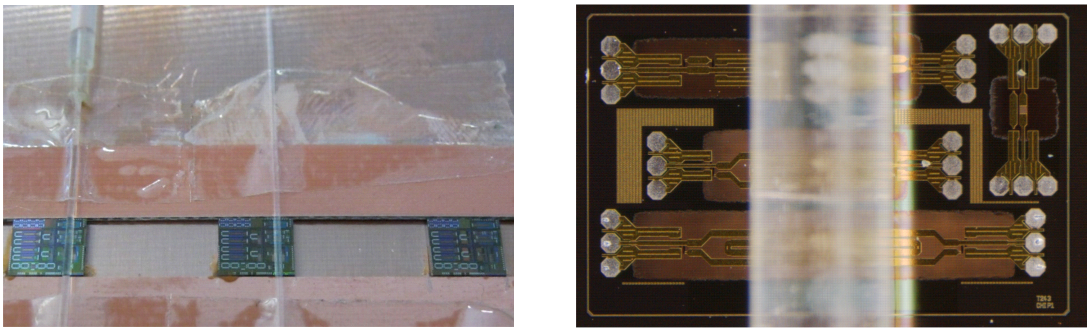

(a) *Photograph of chips with quartz capillaries.* (b) *Zoom.*

Figure 5-15: *120 GHz transducer experiments.*

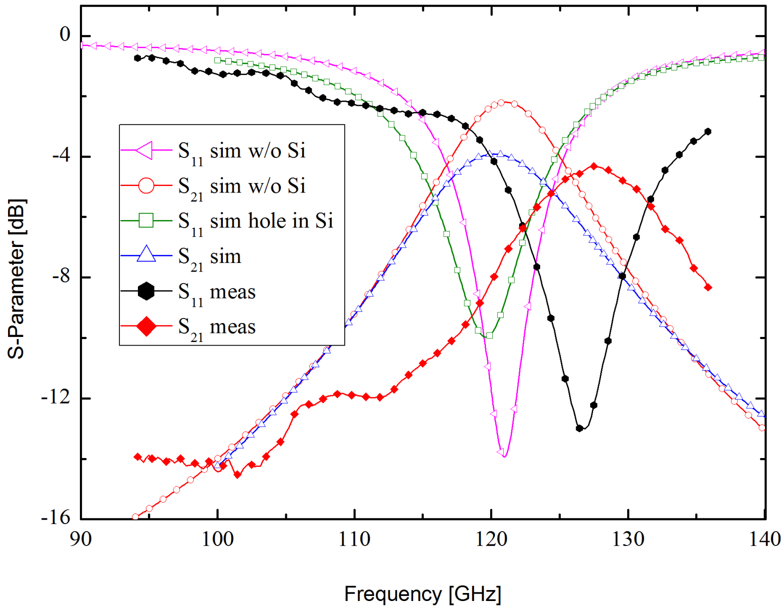

Figure 5-16: *S-parameter measurements of 120 GHz biosensor [16].*

5.4.2 Experimental Results

The S-parameters obtained from the transducer chip and conducted by Schmalz et alius [16] are displayed in Fig. 5-16. On-wafer measurements are compared to FEM simulation results, which demonstrate the effect of removing the silicon substrate using localized back side etching (LBE) available in the manufacturing technology. Simulations depicted in 5-16 proof the intended increase in the quality factor of the transducer. On-wafer measurements showed that the center frequency of the device is at 130 GHz, hence, close to the simulated value of 120 GHz. The measured quality factor is 11.

The transducer chip was applied for investigation of yeast glucose solutions in a microfluidic channel, the setup depicted in Fig. 5-15. The measurements were performed on a probe station using RF probes to contact the pads displayed in Fig. 5-15b. The yeast culture was started by leaven yeast with the glucose carrier solution. After two hours, a sample was sucked into the microfluidic channel on top of the bio sensor. S-parameter measurements have been performed every 60 minutes over 22 hours. Fig. 5-17 shows the transmission S_{21} for three different cultivation stadiums. The center frequency of trans-

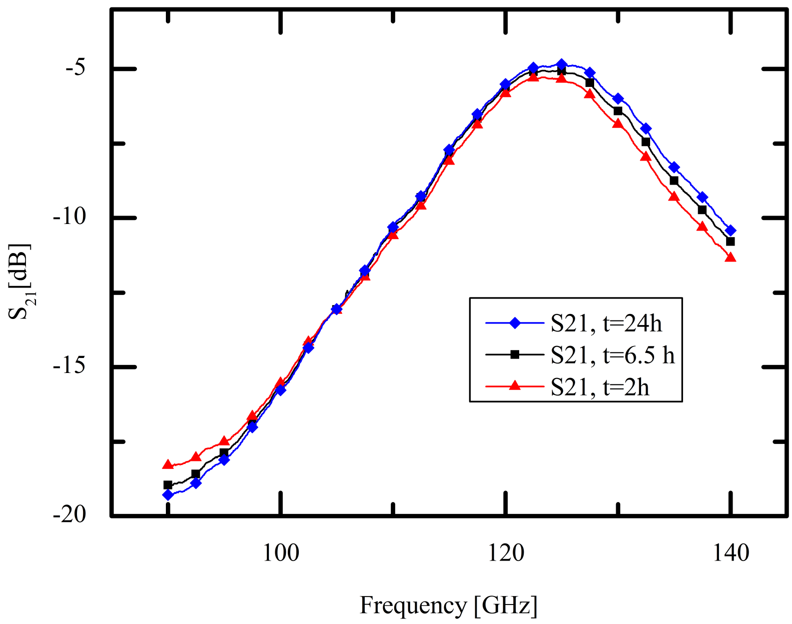

Figure 5-17: *S-parameter measurements with the transducer and yeast glucose solution.*

mission is shifted from 124.05 GHz to 124.98 GHz within 22 hours of cultivation. This shift of 930 MHz is not happening linearly over time, since the cultivation progress is traversing different phases. To investigate this behavior, S-parameters for several cultivation times have been recorded and evaluated. Fig. 5-18 shows a zoom on the right falling edge of S_{21}. Those results show the mentioned characteristics, saying that the cultivation process saturates after a particular duration. It is reflected in the lower frequency shift for cultivation durations towards the end of the experiment. The center frequency was extracted from the measured S-parameters. The results are depicted in Fig. 5-19. The graph

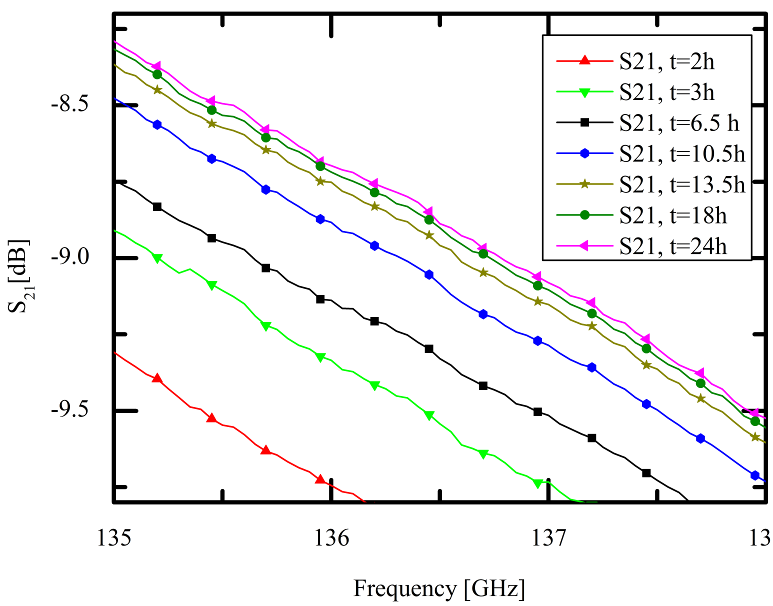

Figure 5-18: *S-parameter measurements with transducer and yeast glucose solution zoomed in.*

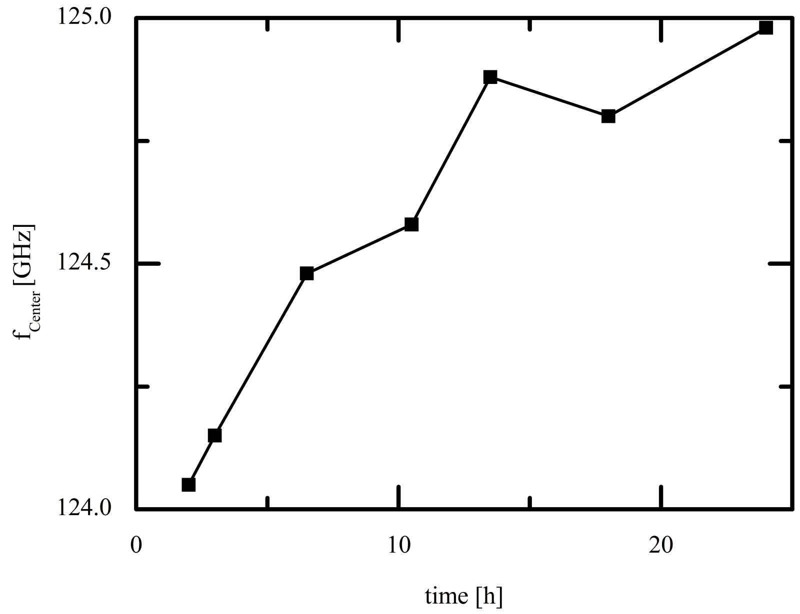

Figure 5-19: *Center frequency versus cultivation time extracted from S-parameters.*

clearly points out that saturation effect. The different cultivation phases have been studied in [113] confirming the qualitative shape observed by millimeter-wave monitoring.

Knowing the performance of the standalone transducer is important for evaluating the measurement results obtained with the on-chip power detector. Results measured with the chip set depicted in 5-14, are displayed in Fig. 5-20. The presented measurements compare the system response with an attached dielectric sample to the empty sensor response. Fig. 5-20 shows the detector signal versus the tuning voltage of the VCO and the VCO frequency as a function of the tuning voltage. The impact of the dielectric sample is reflected in a change of the detector signal which is approximately 80 mV at the higher end of the tuning range. This result demonstrates that the fields generated by integrated

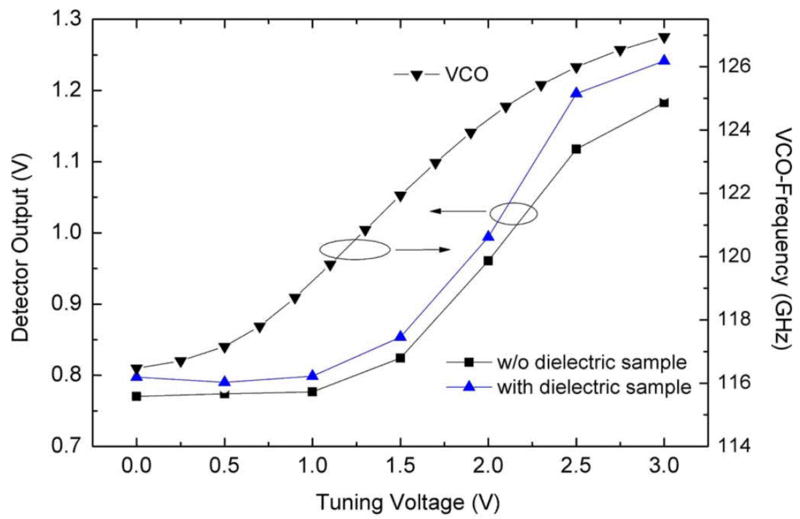

Figure 5-20: *Detector output versus tuning voltage, and the VCO frequency versus tuning voltage of the 120 GHz biosensor [16].*

planar filter structures exhibit a penetration depth into dielectric materials that is sufficiently high to detect and characterize small volumes of samples with high selectivity and sensitivity even at 120 GHz.

5.5 Conclusion

The review of different permittivity characterization methods showed that these are all able to identify the dielectric sample without contact or labels of any kind. The common objective of those methods is the high frequency of operation in the millimeter-wave range or higher. The presented experiments prove that permittivity measurements are suitable at very high frequencies and that the penetration depth is sufficiently high for screening dielectric samples under investigation. One important takeaway is that the phase of a signal screening the respective samples is also a very relevant parameter for monitoring changes in cell solutions in terms of cell number but also for detecting other dielectric samples of interest. The experiments along with the theoretical studies presented lead to the conclusion that a 120 GHz phase sensitive device is the method of choice for permittivity based bio material characterization. The design will be presented in chapter 6.

5.6 Summary

This chapter discussed the application of high frequencies in the millimeter-wave range for characterization of bio material. At first, a theoretical inspection of the processes in the addressed substances was conducted. By combination of different mathematical models provided by the cited publications, a method was developed identifying relevant parameters to perform cultivation monitoring at high frequencies. Investigations have been presented using a continuous wave interferometer to execute experiments from millimeter-wave to terahertz frequencies. These measurements showed that the CW system detects a phase change of approximately $\Delta\varphi/t_c = 2.6\,°/\mathrm{h}$ for a particular yeast culture as the MUT. This result has been confirmed for several frequencies, three of which are reported in Fig. 5-12. Furthermore, those investigations showed that, using the presented technique, a characterization of yeast cell cultivation can be accomplished by sensing the signal phase, which is related to the real part of the permittivity. A discussion of the mathematical theory dealing with transmission and reflection based permittivity detection described the relation between the measured parameters and the correlated refractive index and extinction coefficient. Additional confirmation to particularly address frequencies in the ISM band allocated at 120 GHz was achieved by applying on-chip systems for material screening of two different samples: a yeast culture inside a quartz capillary and a second dielectric sample directly placed on the surface of the CPS sensor. The presented measurement results showed the intended shift in the center frequency according to simulations and evaluation of the implemented models.

6 Millimeter-Wave Interferometer

The strategy pursued in this thesis to develop a miniaturized dielectric sensor consists of the implementation of an interferometer at very high frequencies in the millimeter-wave domain. Along with the scaling of circuits to smaller dimensions, this entails several other advantages, as explained in chapter 5. Still, the implementation of circuits at such high frequencies poses challenging demands to the fabrication technology. The chosen 130 nm SiGe BiCMOS process is well suited to meet those demands, as detailed in chapter 1. In chapter 4 it was demonstrated, that the sensor topology can be realized using microstrip lines and additional passive circuit components to establish the interferometer operation. To obtain reasonable sized passive circuits rendering the implementation of an interferometer on chip feasible, the operational frequency was allocated around 120 GHz. This frequency constitutes a tradeoff between circuit dimensions, penetration depth into MUTs and design complexity. The interferometer can be improved by inserting the function of phase manipulation to calibrate the device. This was discussed in section 4.2 and experimentally proven. The following sections will point out additional advantages of using phase-altering techniques within the interferometer which are practicable at high frequencies using integrated, controllable circuits. The remaining part of this chapter is arranged as follows: Section 6.1 details the function of the interferometer system intended for integration on chip. At first, the basic components are briefly described followed by the detailed explanation of the available operation modes featured by the resulting chip set. Section 6.2 outlines technological parameters of the SiGe technology, the foundation of the developed hardware. The single circuits, their functionality and development is presented in section 6.3. The experimental setup that was utilized to obtain the measurement results presented in section 6.5 is demonstrated in section 6.4. Finally, section 6.6 summarizes the development and specification of the integrated millimeter-wave interferometer.

6.1 Concept

The concept presented here is based on the parallel sensing approach described in section 2.4 using two microstrip lines. The MUT is placed on top of one microstrip, resulting in the sensing setup explained in section 2.4 and sketched in Fig. 2-15. The second microstrip line remains unmodified, serving as a reference. The phase and amplitude differences between a signal conducted by a covered microstrip compared to a not covered one carries information about the effective dielectric constant of the resulting microstrip line. The effective dielectric constant is depending on, among other geometrical parameters, the sample material on top of the microstrip. In section 2.4 it was discussed that the real part of the permittivity of a sample can be obtained from phase characterization of microstrip line signals. These relations are exploited in an electrical interferometer as described in chapter 4. Realizing the interferometer concept on chip renders integration of several other features feasible.

The components building the system are schematically displayed in Fig. 6-1. The signal

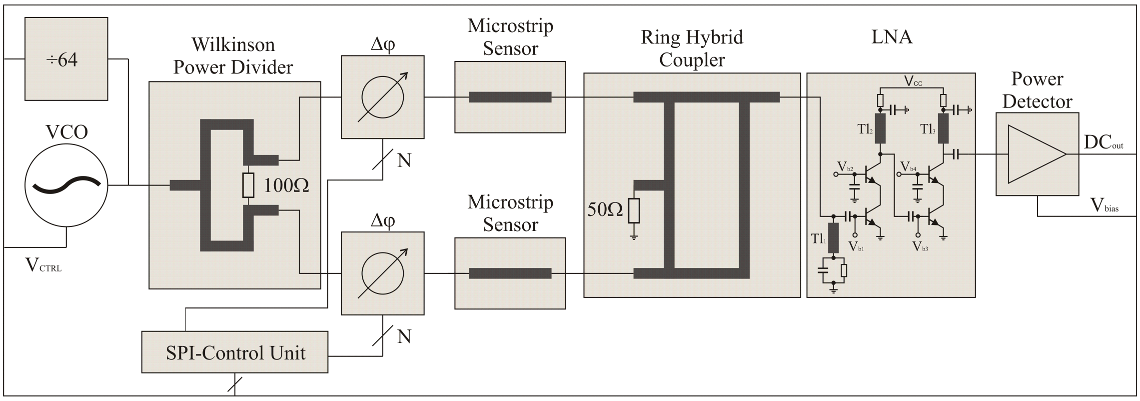

Figure 6-1: *Concept of the electrical interferometer: On-chip components.*

source is a VCO, consisting of two sub-oscillators in common-collector topology and was presented in [112]. The 120 GHz signal from the VCO is fed to a buffer circuit and subsequently to a Wilkinson power splitter to provide two equal radio frequency signals. The following transmission lines are realized as slow wave structures used to provide the feature of phase manipulation. Each line is adjustable linearly in phase and provides 256 states exhibiting a particular phase shift. The detailed function of the SWTL is discussed in section 6.3.3. Each SWTL leads to a simple microstrip line, one as sensing element and on the other branch as reference element. The propagated wave of the sensing line is affected by the MUT permittivity resulting in a phase and an amplitude difference of the two signals as explained in section 2.4. The hybrid ring coupler that follows, translates that phase difference into a frequency shift of the transfer function minimum, as explained in section 3.3. The output power of the hybrid ring coupler is amplified by a low noise amplifier (LNA) and a power detector transforms that power into a DC voltage value. The amplifier is implemented as an LNA because very small power levels must be detected and distinguished from the present noise floor. The signal source, the LNA and the power detector could be reused from previous designs and matched to the remaining components. The design of those components was not part of this thesis.

The general idea behind the setup illustrated in Fig. 6-1 can be explained with the help of simulation results, taking the core components of the interferometer into account. These are the Wilkinson divider, the SWTL, the microstrip sensing lines and the hybrid ring coupler. In that constellation, the transfer function resembles a notch filter's S_{21} shape with a center frequency tunable by phase manipulation. This is demonstrated by the simulation results depicted in Fig. 6-2. The transfer function is displayed for four different cases, starting from the initial point for an unloaded sensor represented by the black curve with a center frequency at 120 GHz. A sample that is placed on the sensing line, can have two effects. Either it is simply altering the propagation phase of the sensing line, so that the S_{21} center frequency is shifted leading to the blue curve. In that case, the power level change accompanying the frequency shift is simply evoked by the frequency dependent characteristics of the hybrid ring coupler. Or, on second account, it changes both, the propagation phase and attenuation of the microstrip line, which is represented by the green curve. The attenuation difference between sensing and reference line additionally elevates the S_{21} transfer function to higher power levels. In that case, circumstances are more complex, since the attenuation also influences the phase frequency relation, what

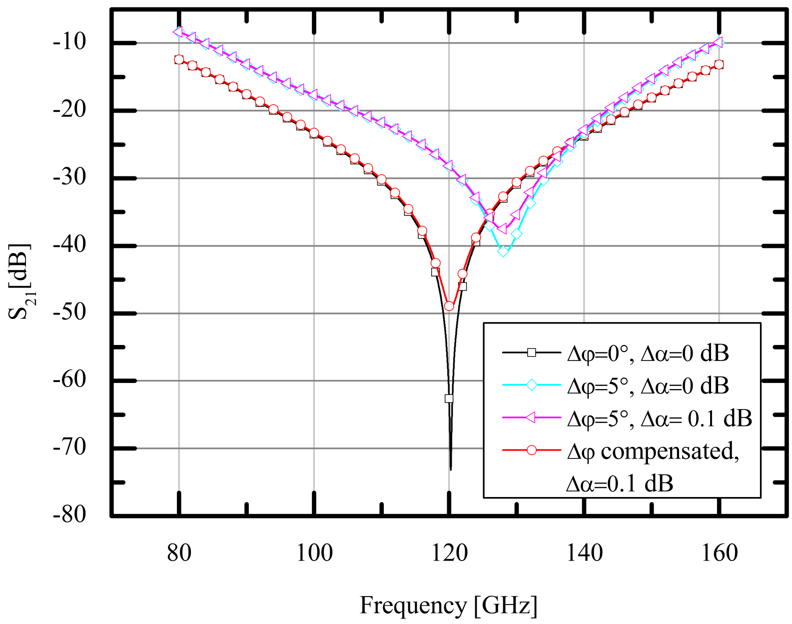

Figure 6-2: *Simulated transmission S_{21} of the interferometer.*

was investigated and demonstrated in section 3.3. This leads to slightly different center frequencies of the blue and the green curve even though the phase shift is the same for both cases.

A solution for that issue is to equip the interferometer with phase shifters. The reference line's phase is adjusted to push back the transfer function to its original center frequency of 120 GHz. The described case is also illustrated in Fig. 6-2, the red curve. In this state, both phase shifts are the same, the one evoked by a sample and the one adjusted using the phase shifter. Still, the attenuation difference remains visible, reflected by the power level difference of the red and the black curve. Despite the fact that attenuation effects the amount of frequency shift that is caused by a certain phase shift evoked by a sample on top of the sensing line, it doesn't effect the phase amount necessary to restore the initial center frequency. This owes to the circumstance that the attenuation can't manipulate the frequency shift directly. It simply can change the intensity of the frequency shift evoked by a phase shift on the sensing line. This is a powerful strategy for determining phase shifts without the impact of attenuation interfering the results. The compensation of the phase has the advantage, that no simulation or other models are needed to map phase and frequency shift. The phase is determined by balancing reference and measurement microstrip line. When a sample exhibits a significant conductivity, rendering the attenuation effect relevant to some extent, the attenuation can be extracted from the power level difference remaining after phase compensation (red and black curve in Fig. 6-2). However, this requires the utilization of models to relate the changed line attenuation to the overall power level shift of the S_{21} transfer function.

To investigate the impact of attenuation in the measurement path caused by the MUT, further simulations have been carried out. The phase shift was adjusted to a constant value and the attenuation was swept. Figure 6-3 displays the results for an exemplary phase shift of 2° in a linear scale and in dB. Attenuation caused by the sample is labled $\Delta\alpha$ since the remaining parts of the measurement path ideally are identical to the reference path and

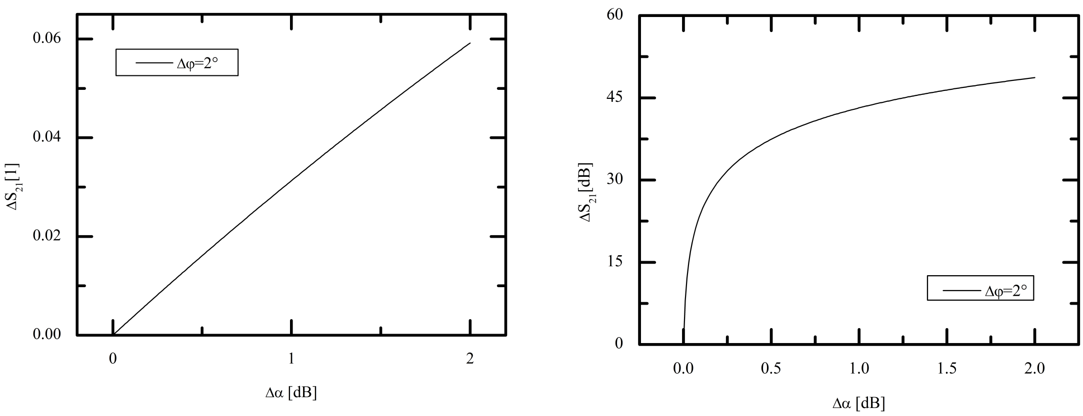

(a) S_{21} *minimum power level shift at 120 GHz.* (b) S_{21} *minimum power level shift in dB.*

Figure 6-3: *Simulated effect of attenuation differences on the transmission* S_{21}.

thus exhibit the same insertion loss. The x-axis is in dB for both figures. From Fig. 6-3a it becomes clear that a logarithmic change of the attenuation causes a linear change in the power level of the S_{21} notch. Figure 6-3b shows the same results in dB. Using this relation obtained from a circuit model, it is possible to estimate the attenuation evoked by an MUT from the interferometer transfer function S_{21}. However, results strongly depend on the model accuracy.

Experiments presented in section 5.3 showed that the phase is a well suited indicator to learn about the composition of a sample of interest. Hence, in target applications, it is suitable to rely on the accurate phase compensation technique rather than estimations derived with the help of models.

The design topology provides a high flexibility in terms of operation modes. Three modes are considered in this thesis and will be described in the following:

1. In the first mode discussed here, a frequency sweep is carried out, where the VCO is tuned by an external PLL within the boundaries of its tuning range, to obtain the frequency response of the interferometer. The center frequency can be extracted from the results. When placing an MUT on top of the sensing line, the center frequency is shifted to higher or lower frequencies. In the discussed case, the upper microstrip line displayed in Fig. 6-1 is exposed to the MUT and the lower line remains free and serves as the reference. Since the reference medium is air, the MUT permittivity is higher than the one of the reference medium. According to equation (3-7) derived in section 3.3 that means a sample can only shift the center frequency up in the spectrum. The transmission versus frequency is recorded and post processing is applied to extract the center frequency from the obtained data. Together with either an analytical model or an EM based model, the center frequency can be related to the phase shift, evoked by the MUT. The real part of the permittivity is extracted from the phase as explained in section 2.4. If required, the imaginary part can subsequently be derived taking the notch power level into account.

2. The second mode is operating the interferometer at a single, fixed frequency. This produces a single voltage value at the output of the power detector for a singular sample. This procedure requires an extensive parameter analysis tuning the phase

and recording the interferometers frequency response in advance to set up a look-up table. The knowledge about the frequency response for different phase conditions allows to link up one frequency response from the data set with the measured output voltage value. The center frequency and the associated phase shift can also be derived for each frequency response in advance and stored in the look-up table, so that the single voltage value can directly be related to the phase shift and, after further calculations, to the sample permittivity. The extraction of the permittivity depends on the particular channel geometry so that the exact knowledge of the dimensions is mandatory for accurate results.

3. The third mode makes use of phase balancing while the power detector output voltage is monitored. The measurement procedure contains three iterative steps. At first, the minimum output power within the interferometer's tuning range needs to be determined and adjusted. The initial center frequency must be stored and serves as the reference value. Subsequently, the sensor is exposed to the sample and thus changing the frequency response of the interferometer. Using a fixed frequency, the original center frequency, this is indicated by an increased output voltage. As the third step in this mode, the phase of the reference line is adjusted to restore the initial voltage, the reference value recorded in step one. A successive frequency sweep is carried out to confirm that the original center frequency is restored. If that is not the case, the sample features a noticeable conductivity causing attenuation. Iterative adjustment of the phase shifters followed by frequency sweeps are now necessary to restore the original center frequency of S_{21}. This assures that the phase shift on both lines, the reference and the sensing line, are the same, so that the phase shift stemming from the MUT is compensated for. In that state, the attenuation can be extracted from the power level difference of the S_{21} minimums of the reference, the black curve, and of the measurements, the red curve in Fig. 6-2.

The act of balancing is similar to the impedance measurement with a Wheatstone bridge. The digital phase state of the reference line provides direct information on the phase shift and with that in turn, as in mode one and mode two, about the sample permittivity. This requires the proper knowledge of the phase states that can be adjusted by the slow wave phase shifter. Therefore, the slow wave line must also be implemented in a standalone test structure on a chip. This will be presented in section 6.3.3. It allows to determine the phase states of that structure experimentally and to validate the simulation models. This mode can be implemented by performing a loop operation using an external controlling unit determining the proper phase switching state and automated permittivity monitoring becomes feasible [1].

A second variant of this mode further improves the accuracy of measurement results. Both phase shifters are preadjusted to create a phase shift which is half of the maximum phase shift the lines are capable of. When the sample is put on the sensor affecting the signal phase, this can be compensated for on the same line, the sensing line rather than the reference line. The error that is caused by asymmetrical propagation characteristics of reference and sensing path, which is investigated later on in this chapter, can be avoided by applying that method. However, the detectable range of permittivity is divided in half. For the decision on the chosen operation mode for the presented system, the pros and cons of the different modes are evaluated in the following discussion.

Mode 1: Pros

- Recording the scalar transfer function $|S_{21}|$ over frequency provides all the available information: the center frequency, the quality factor and the power level in the available tuning range
- The effect of temperature can be considered by proper evaluation of this data
- The access to the entire transfer characteristics of the device reduces the probability of unnoticed malfunction

Cons

- Performing the frequency sweep is slow compared to capturing a single voltage value since the external PLL needs to settle for each frequency step
- Post processing of the data is time and power consuming
- Extraction of the phase from the center frequency by comparison to EM or analytical models produces a certain error due to inaccurate models
- Combined effect of attenuation and phase changes causes evaluation error, so that this mode is only applicable for material with a negligible imaginary dielectric constant. Through calibration before measuring, measurements are also feasible for a noticeable but fixed imaginary dielectric constant.

Mode 2: Pros

- The fastest of the three measurement procedures
- Working at a fixed frequency avoids dispersion-related errors

Cons

- Post processing of the data is time and power consuming
- Extraction of the phase from the center frequency by comparison to EM or analytical models produces a certain error due to inaccurate models
- only suitable to detect samples with a fixed imaginary part. Results are inconclusive otherwise

Mode 3: Pros

- A minimal number of frequency sweeps is a tradeoff between accuracy and measurement duration. The number depends on the attenuation altering the phase-frequency characteristics of the interferometer.
- The calculation of the phase from a frequency shift is redundant since the phase can directly be determined by the described compensation technique. Errors stemming from attenuation changes are eliminated.
- After the compensation step is over, the comparison takes place at the same, original center frequency, so that dispersion-related errors are avoided.

Cons

- Performing phase compensation takes several iterations and hence a little more time than measuring a single value

- The phase resolution is limited which devolves upon the phase measurement accuracy and is causing error through quantization. A tradeoff between resolution and chip complexity is done, since each phase state requires two switch circuits per SWTL.
- The phase shift induced by the SWTL must either be measured from a test chip or extracted from calibration measurements, where the transfer function is recorded for all of the 256 phase shifting states. The former produces an error according to measurement accuracy limitations and process variations from chip to chip. The latter has the same error from inaccurate models as Mode 1 and 2.

The drawback of manufacturing fluctuations in the last operation mode can be alleviated by calibration using fluids with a known permittivity. Ethanol water solutions can be utilized to calibrate the sensor in the beginning. The permittivity can be varied by changing the ethanol concentration in water and the corresponding voltage is stored. Still, the conductivity of this type of samples is noticeable so that the attenuation is varied as well and needs to be considered while calibrating. This procedure is beneficial and enables higher accuracy no matter which operation mode is applied and needs to be done for each chip before measurements.

In the following section, the SiGe BiCMOS technology utilized for circuit implementation is presented.

6.2 130 nm SiGe BiCMOS Process

The technology for circuit implementation is a 130 nm BiCMOS SiGe:C process and is based on technology presented in [114] and [115]. The available bipolar transistors in this process were optimized as demonstrated in [116] leading to high speed HBTs featuring an $f_t/f_{max}/BV_{CEO}$ of 300 GHz/500 GHz/1.65 V. The main process parameters are listed up in table 6-1. One figure of merit to specify the performance of a process is to measure the

Parameter	high-speed HBT	High-voltage HBT
A_E	$0.12\,\mu\text{m}^2 \times 0.48\,\mu\text{m}^2$	$0.18\,\mu\text{m}^2 \times 1.02\,\mu\text{m}^2$
Peak f_T	300 GHz	45 GHz
Peak f_{max}	500 GHz	120 GHz
BV_{CEO}	1.65 V	3.6 V
BV_{CBO}	4.9 V	16 V
β	900	900
1.2 V core NMOS V_{th}	0.5 V	
1.2 V core PMOS V_{th}	0.47 V	
MIM Capacitor	$1.5\,\text{fF}/\mu\text{m}^2$	
P^+ poly resistor	$250\,\Omega/\square$	

Table 6-1: *SG13G2 process parameters.*

ring oscillator gate delay. For the chosen technology 2 ps have been demonstrated. Figure 6-4 shows the backend metal stack. The figure displays 5 thin layers (M1-M5) and two thick layers (TM1 and TM2) with a thickness of 2 µm and 3 µm, for the implementation of

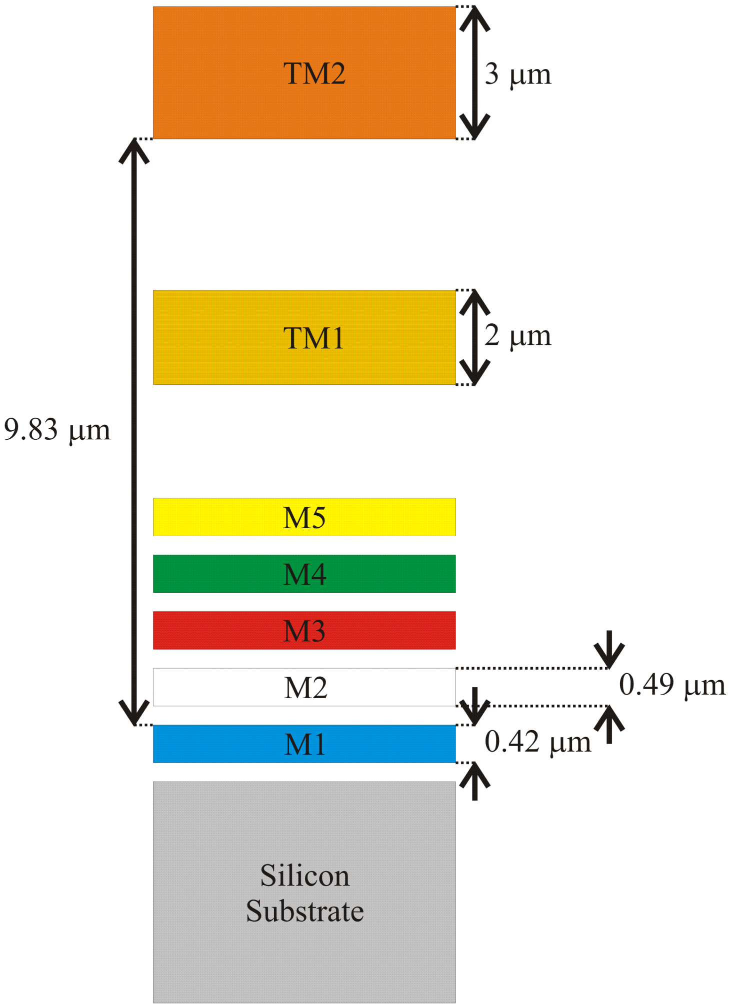

Figure 6-4: *Metal stack of the SiGe process (true to scale).*

low-resistivity connections and hence high-quality passives. 130 nm gate length CMOS devices with thin and thick gate oxide for 1.2 V and 3.3 V core voltage are available.

The mentioned parameters are crucial for design considerations for the single circuits and components described in the following section.

6.3 Circuit Components

6.3.1 Passive Components

Two key components forming the core interferometer are the Wilkinson divider and the hybrid ring coupler. Their design is based on a classic setup using microstrip transmission lines. Both elements have been designed using method of moments (MOM) simulations. The proper design procedure from analytic line width calculation to EM simulation of the resulting overall layout was done as proposed in section 4.1 at the designated frequency of 120 GHz. The Wilkinson divider layout is sketched in Fig. 6-5. The microstrip lines are comprised of conductors in metal layer TM2 and a ground layer in metal M1. These layers have, as depicted in Fig. 6-4, a distance of 9.83 µm. For that constellation, the

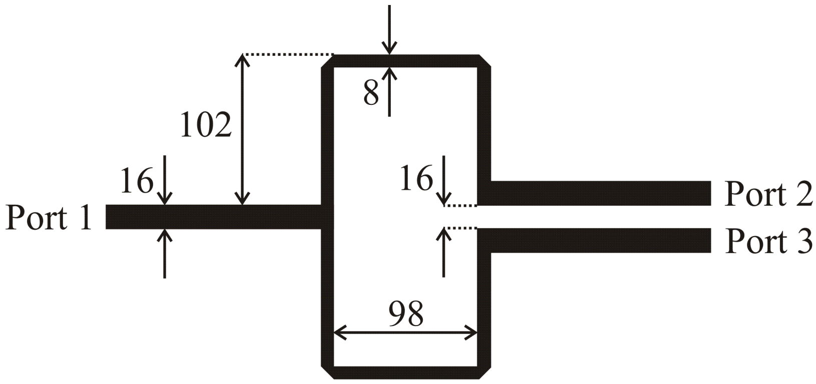

Figure 6-5: *Layout of the on-chip Wilkinson divider (true to scale, units in* µm*).*

line width calculated with LineCalc and subsequently confirmed by EM simulations is 16 µm for 50 Ω lines and 8 µm for 70.71 Ω lines. The contacts for the 100 Ω on-chip resistor that is part of the Wilkinson are positioned at the end of the $\lambda/4$-branches in Fig. 6-5. The contacts of resistors available in this technology are in metal 1 (M1) so that the contact must be established with a via stack from top metal 2 (TM2) to metal 1. The resistor is a P^+ poly type resistor, comprising unsalicided, p-doped gate polysilicon. The design was characterized with EM simulations leading to the results displayed in Fig. 6-6. Those results demonstrate that the circuit is not optimized for 120 GHz operation. The resulting center frequency of operation is much higher, in the range of 135 GHz. Since the Wilkinson divider is a broadband element, it was decided to prefer minimum size over optimum matching at design frequency of 120 GHz. Compared to the frequency optimized divider it saves 30 % of space and the performance is comparable.

The hybrid ring coupler layout is depicted in Fig. 6-7. Since its function is also based on 50 Ω and 70.71 Ω lines, the same line widths were also used here. The dimensions

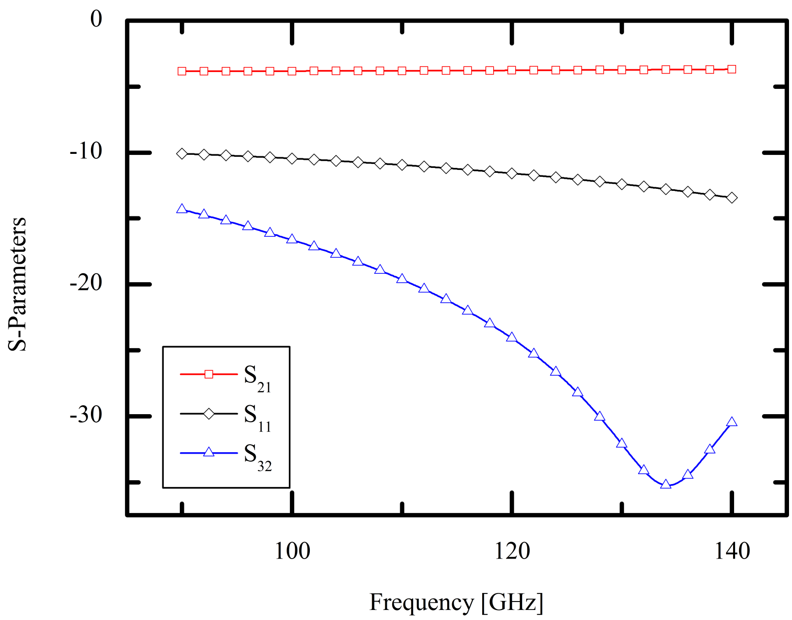

Figure 6-6: *EM Simulation results of the Wilkinson divider.*

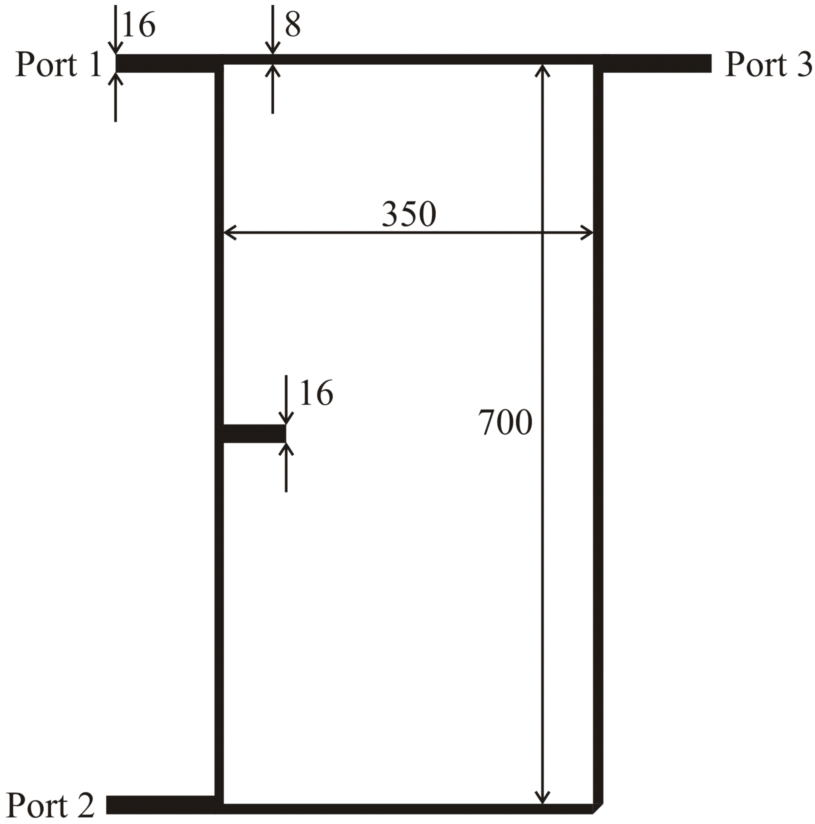

Figure 6-7: *Layout of the on-chip hybrid ring coupler (true to scale, units in* µm*).*

are designated in Fig. 6-7. The basic function of this coupler type was discussed in section 4.1. In Fig. 6-7 the input ports are the ones on the left. The port in the center on the left side is the sum port which needs to be terminated using a 50 Ω resistor. The port on the right is the output port. The hybrid ring coupler is the element determining the center frequency of the complete interferometer. Hence, the dimensions needed to be optimized using EM simulations in several iterations until the center frequency is achieved with sufficient accuracy. The final simulation results obtained with the dimensions shown in Fig. 6-7 are depicted in Figs. 6-8a and 6-8b. The input reflections for both input

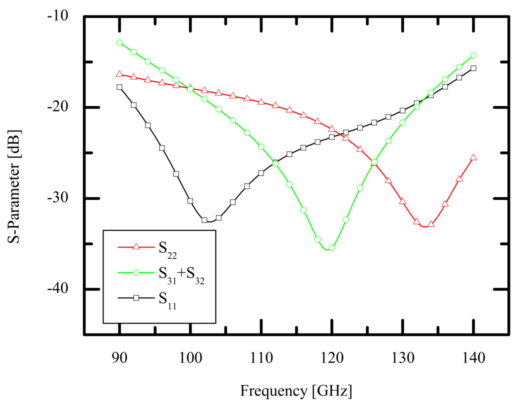

(a) S_{11}, S_{22} *and vector sum of* S_{31} *and* S_{32}.

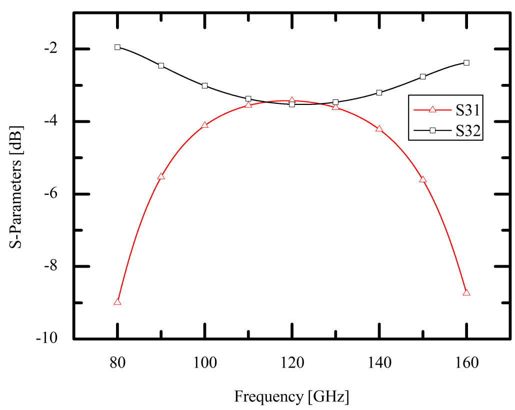

(b) *Transmissions* S_{31} *and* S_{32}.

Figure 6-8: *Simulated S-parameters of the hybrid ring coupler.*

ports are lower than −22 dB at 120 GHz. The vector sum of both transmission signals S_{31} and S_{32} is indicating the function in the final setup as an interferometer, since both inputs will be excited with in-phase signals which have the same amplitude in the ideal case. The minimum S_{21} is at 119.4 GHz and has a power level of approximately −36 dB. This value is a figure of merit for the symmetry of S_{31} and S_{32}. Figure 6-8b shows a plot of both transfer functions versus frequency. The graphs exhibit a certain level difference at the center frequency. The simulated value is 0.25 dB. This difference is deteriorating the performance of the interferometer by lowering its quality factor. The difference is stemming from a path length difference from port 1 to port 3 compared to port 2 to port 3 introducing losses owing to a finite conductivity of the microstrip lines and dielectric properties of the substrate. The attenuation constant can be derived using LineCalc. This leads to an effective attenuation of 0.44 dB/mm. The path length difference can be taken from the layout that is displayed in Fig. 6-7 and amounts to 716 µm. The theoretical value for the difference in transmission for the signals S_{31} and S_{32} is 0.31 dB, thus close to the EM simulated result of 0.25 dB. In section 4.1 this issue was addressed by tapering one path to introduce losses also in the shorter path. In the final millimeter-wave interferometer, this issue is alleviated by the feature of phase calibration which is improving the quality factor and hence the performance. This will be discussed later in this chapter. The next subsection presents the on-chip source that is applied for exciting the interferometer.

6.3.2 Source

The core of the 120 GHz signal source is a 120 GHz VCO. The basic schematic is depicted in Fig. 6-9. The applied push push principle makes use of two common-collector

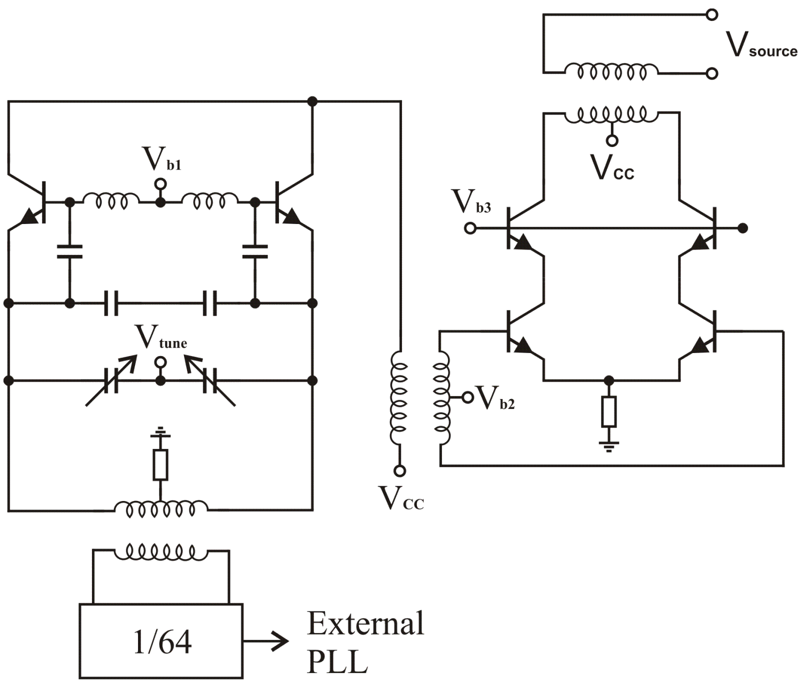

Figure 6-9: *Voltage controlled oscillator and buffer amplifier as 120 GHz source.*

sub-oscillators operated at the same frequency in odd mode. Driving the active devices in a highly nonlinear region, the generation of harmonics is enforced. Odd mode operation assures a phase difference between both oscillator signals in multiples of $n \cdot \pi$ for the n^{th} harmonic. Hence, the fundamental signal as well as odd harmonics are canceled out, when the superposition of both signals occurs. This allows the devices to operate at high frequencies and an improved phase noise performance is achieved [117]. The VCO presented in [16] was used for the millimeter-wave interferometer. The fundamental signal frequency is 60 GHz. The fundamental signal is coupled out with a transformer and subsequently routed to a divider chain. This way, the fundamental signal can be stabilized using an external PLL, as indicated in Fig. 6-9. Stabilizing the fundamental frequency, the divider chain can be reduced by one divide-by-2 block compared to the operation with a fundamental 120 GHz VCO. Here, the divider chain results in a divide-by-64 circuitry, which is providing the output signal for the PLL in the range of 950 MHz. The second harmonic signal is coupled to a buffer amplifier with the help of a second transformer. The buffer feeds the 120 GHz signal to the input of the Wilkinson divider. The VCO has a tuning range from 117 GHz to 125 GHz and provides approximately 7 dBm of output power along with the buffer amplifier. The further active building blocks of the design were designed with respect to that value regarding power level planning. Another key element of the interferometer is the SWTL phase shifter. Design considerations and the final design are presented in the following subsection.

6.3.3 Slow-Wave Phase Shifter

In chapter 4 it was demonstrated that the interferometer approach can be improved by including phase shifters for calibration. In order to benefit from a phase shifter, it is crucial to maintain the propagation characteristics as well as reflection behavior over all phase states. This is important since the measurement line is compared to a reference line in the interferometer and both lines can feature a different phase state. Still, input and propagation characteristics need to be as similar as possible for this method to work accurately. Higher symmetry provides a higher potential quality factor and hence higher read-out accuracy. Most phase shifting techniques show significant variations in insertion loss for different phase shifts. The chosen topology, the slow wave line, can be designed to avoid that. The second aspect that led to the choice of this phase shifter topology was attributed to the necessity for highly linear phase shift behavior and well known phase states. This is required to relate the phase to the switching state, since this can not be monitored within the interferometer. It needs to be characterized in a standalone test chip, that will be presented later on.

The basic setup of the SWTL is presented in Fig. 6-10. A microstrip transmission line forms the basis of that circuit. The dimensions were calculated and subsequently optimized using EM simulations to achieve a characteristic impedance of 50 Ω. Fig. 6-10 contains also the metal layers relevant for this design and their position within the metal stack. The transmission line carrying the wave is in the top metal layer and the associated ground plain in the bottom one. The medium in between is silicon dioxide. This structure has a particular effective permittivity that can be derived as explained in section 2.4. As depicted in Fig. 6-10, the structure contains also metal strips between the center conductor and the ground plane. The metal strips are connected to circuits using HBT

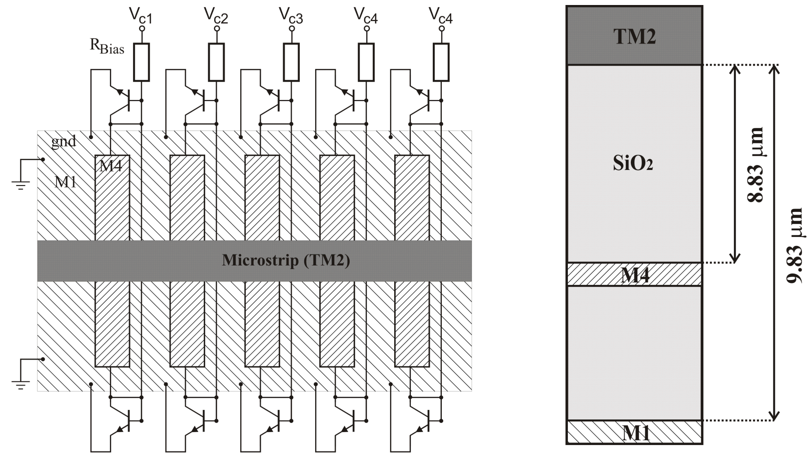

Figure 6-10: *Concept of the slow wave transmission line and metal stack.*

based switches, one at each side of the center conductor to ensure a symmetrical field distribution. The switches are voltage controlled and can either connect the metal strip to the ground plain or leave them unconnected in a floating condition. In the latter case, the HBT diode simply is not supplied with a voltage, so that no low ohmic path for the RF signal is provided. The metal strips change the effective permittivity of the substrate according to their switching state. This is called artificial dielectric.

The resulting transmission line can be described as a composition of line sections exhibiting a different characteristic impedance stemming from a different effective permittivity. This is schematically displayed in Fig. 6-11. The alternating impedance leads to an over-

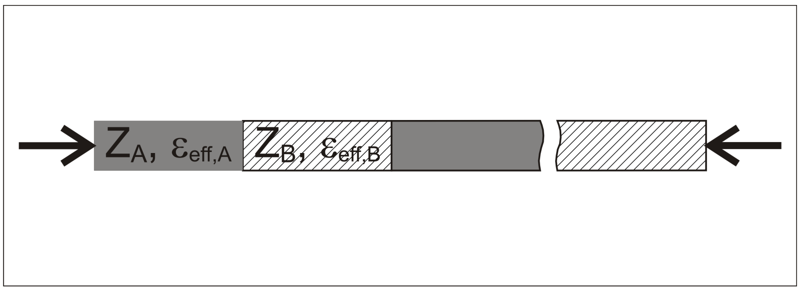

Figure 6-11: *Slow wave transmission line equivalent diagram.*

all impedance $Z_0 = \sqrt{Z_A Z_B}$ [118]. In the presented approach, the impedance Z_B of the second line component is controllable, by using the HBT switch. Furthermore, it depends on the RF characteristics of the HBT circuit. Hence, the analytical investigation of the line was only used for a preliminary design to be optimized applying EM simulations. One of the main design considerations was to introduce phase shift without altering the other characteristics of the line, like insertion loss and input reflection. In the early design phase it was learned from EM simulations that the usage of a metal layer higher than metal 4 changes the impedance of the line significantly and with it its losses.

The second restriction that was revealed by simulations is that the strip width w_S may not exceed the spacing S because otherwise a massive change in the characteristice impedance occurs. Introducing metal strips in a respective layer is changing the ground reference. It can be seen as creating a virtual ground layer between metal 1, the original ground layer, and the metal strip layer. Using a metal strip with the biggest distance to metal 1, the maximum achievable effect in terms of characteristic impedance tuning is achieved. As a tradeoff between maintaining the propagation characteristics and evoking a sufficiently high phase change, metal 4 was chosen for metal strip implementation. Once the layer of choice is fixed, the SWTL line has two physical degrees of freedom left, which is the spacing S and the width of the strips w_S, both indicated in Fig. 6-10. The spacing as well as the widths of the strips was set to 5 µm. Taking the HBT diodes into account, another parameter, the collector current, emerges. This will be explained later in this chapter. The design steps were carried out as follows:

- Determining the phase range and resolution for target applications
- Defining w_S and S to achieve the target phase shift per strip
- Developing a switch topology and determining the proper dimensions to achieve the desired phase range
- Characterizing the cooperation of the passive transmission line and the active switch

To define the range of phase, it is necessary to set a channel geometry, that will be placed onto the sensing line. Furthermore, the permittivity of potential MUTs needs to be known. The maximum phase shift is evoked for the highest considered permittivity, which is that of fresh water. In [5] it was reported that the parameter of interest is the real part, since it accounts for a phase shift in the propagated signal. The value that can be found in literature [62] for water at room temperature at 120 GHz is approximately $\varepsilon_r' = 7$. Considering a 30 % margin for the design, the maximum value was considered to be 10. The widest microfluidic channel that is intended to be used with the interferometer will cover 1 mm of the SWTL so that the maximum phase shift that is expected to be caused by the sample can be calculated with the help of equations derived in section 2.4. The phase shift versus MUT permittivity for a chosen channel geometry was calculated and the results are depicted in Fig. 6-12. A 1 mm part of the sensing line is covered by the material under test. To accommodate a reasonable volume for future applications, this is the maximum channel width that is considered for the development of the interferometer. Along with the maximum real part of a permittivity considered here, this is leading to a calculated phase shift of 1.7°. With a 15 % margin, the SWTL phase shifters were designed for a phase range of 2° to make sure the target samples can be characterized by the developed device.

The line was EM simulated using the method of moments technique. In the first simulation setting, the metal strips were simply connected to a perfect ground or left unconnected in a floating condition. This setup was used for first choices to be made, e.g. strip width and spacing causing an acceptable change in the propagation and reflection characteristics. The difference in phase was derived with respect to the phase of a second, equal SWTL, where all strips were unconnected, to investigate the effect of switching. In the EM setup, each metal strip had two ports, one at each end, acting as the interface for further schematic level simulations with ideal elements. This scenario is sketched in Fig. 6-13.

In ADS momentum there are several options for ports. For connecting the metal strips, "‘TML zero length"’ ports were used. This calibration type removes capacitive effects at the open end of a structure. To excite the center microstrip of the SWTL, TML ports were employed, assuming that the structure is fed through a transmission line. This calibration type removes fringing fields and other open end effects and adds mutual coupling, which is induced by the current flowing on a virtual calibration feed line. This assumption is accurate since the SWTL lines are fed by microstrip leads in the final design. As already mentioned before, the metal strips for permittivity manipulation need to be connected to a switch at each end to guarantee a completely symmetrical EM characteristic. Keeping in mind that these switches need to be digitally controlled later on, it is desirable to trigger both switches with a single control signal, to keep the complexity down. For that reason, DC leads were inserted beneath the metal strips in Metal 2. To account for their EM effects, the simulations were carried out with those connections being part of the layout. They are also displayed in Fig. 6-13.

The switch structure presented before needs to be driven by a CMOS inverter chain since the output current of the SPI interface is limited. The schematic in Fig. 6-14 depicts the circuit used as a buffer. The critical design aspect for the CMOS inverters was that in off-state, the HBT displayed in Fig. 6-14 is turned off by pulling down the base potential to ground so that the transistor blocks the path from the metal strip to ground.

On the other hand, this also provides a path to ground via the NMOS transistor that is pulling down the base node, designated by a gray, dotted arrow in Fig. 6-14. This is why a non symmetrical CMOS stack was designed with different sizes of p-type and n-type MOS transistors. The PMOS transistor needs to provide the collector and base current of the HBT when in on-state, and hence has the maximum available width of 20 µm. When in off-state, there is ideally no current, the base potential simply needs to be low and still, there should be no ground path from the metal strip to ground. Thus, the NMOS transistor has the minimum width of 130 nm. This assures a low base potential and still high resistance to ground. In addition to that, the bias resistor that is used to adjust the current in on-state, is as large as possible for the given standard 1.2 V supply voltage. The off-state resistance from the metal strip to ground is R_{bias} plus R_{on} of the NMOS. The

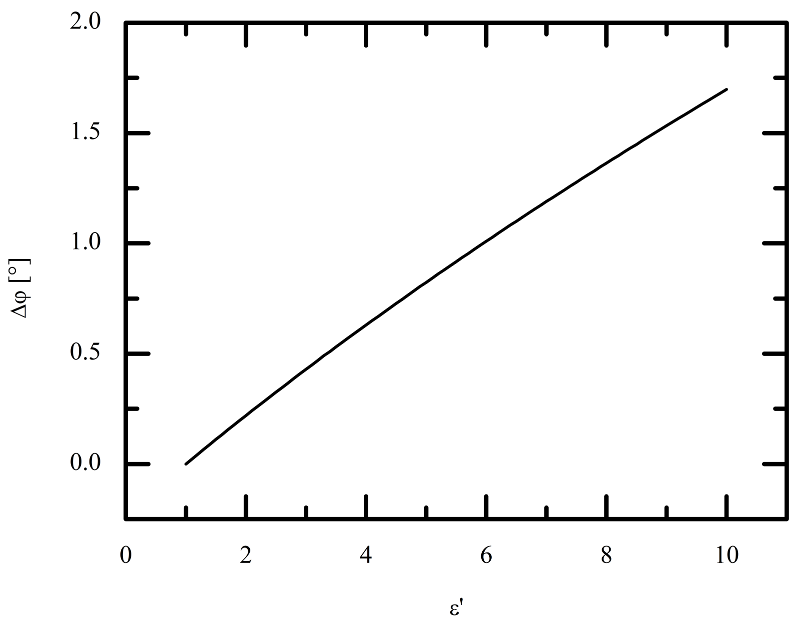

Figure 6-12: *Simulated phase shift versus MUT permittivity.*

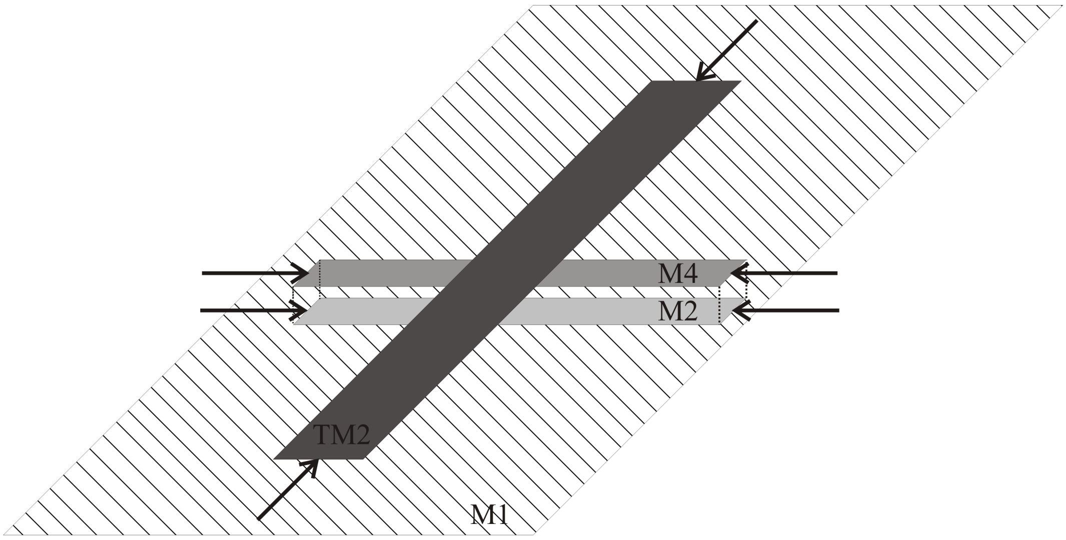

Figure 6-13: *SWTL 3D view.*

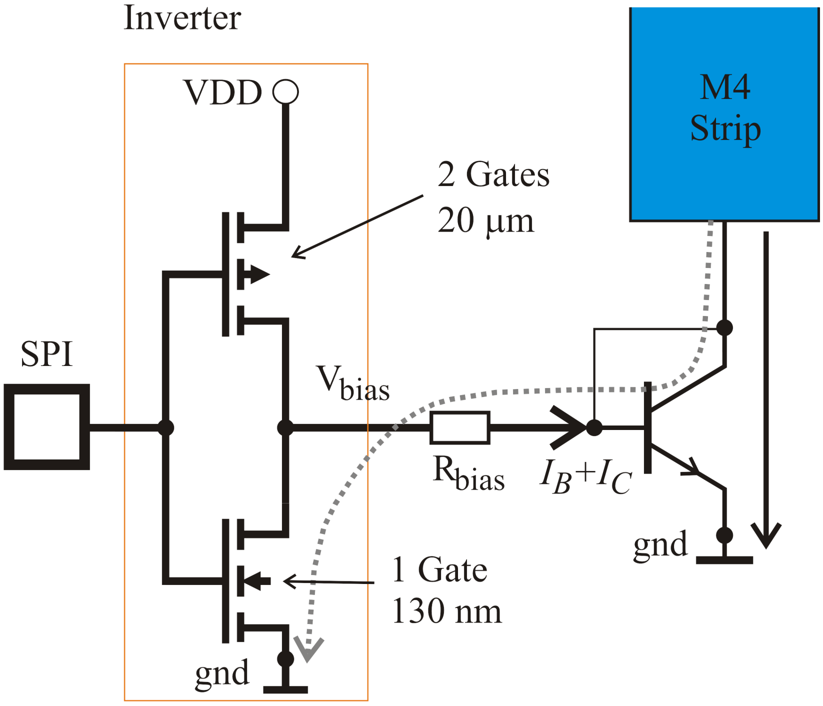

Figure 6-14: *Driver topology.*

collector current of the HBT transistor defines the current gain and the transit frequency. As a result, it affects the RF characteristics of the ground path in on-state. This also determines the phase difference that is evoked by toggling a single switch. The value of R_{bias} was set to adjust a collector current to achieve the desired value of phase shift per switch. The final value was found to be $R_{bias} = 1314\,\Omega$.

Simulations showed, that not only the amount of phase change, but also the linearity of the phase change versus number of metal strips is affected by the quantity of bias current in each switch and was also considered in the dimensioning. The complete setup of the SWTL is sketched in Fig. 6-15. Since it is not practical to switch each strip separately,

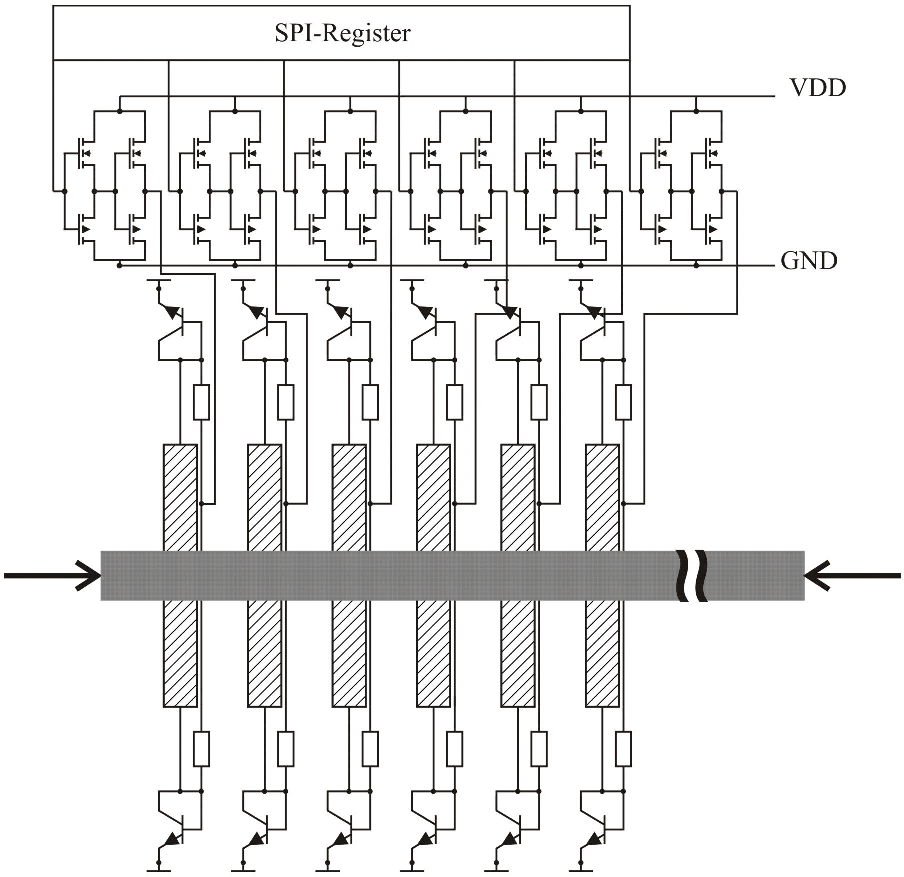

Figure 6-15: *SWTL complete circuitry.*

the strips were connected to each other using thermometer-code. The setup is endowed with 256 metal strips, meaning 256 phase states. These can be controlled using an 8 bit register within an SPI interface on chip for each line. The simulation results with the final line geometries are presented in the following.

To investigate the performance of the SWTLs, MoM simulations were conducted together with the transmission line sensors. The passive components were simulated individually

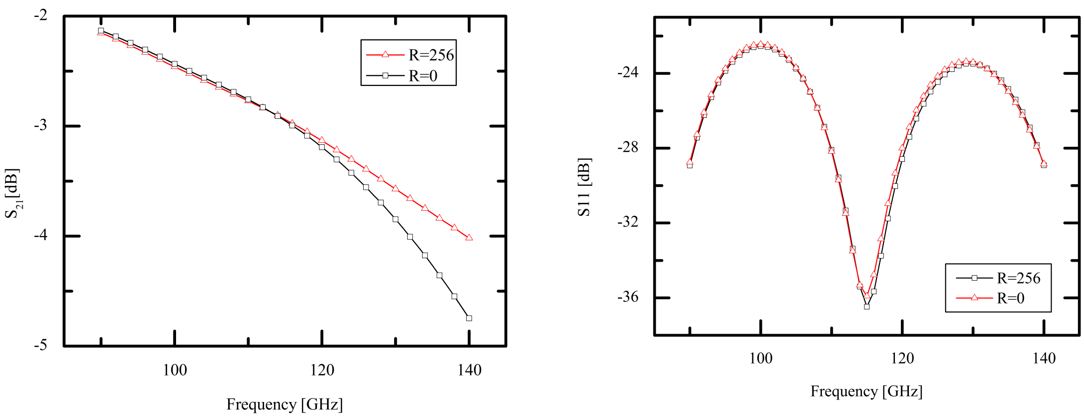

(a) *Transmission* S_{21}.

(b) *Reflection* S_{11}.

Figure 6-16: *Simulated S-parameters of the SWTL.*

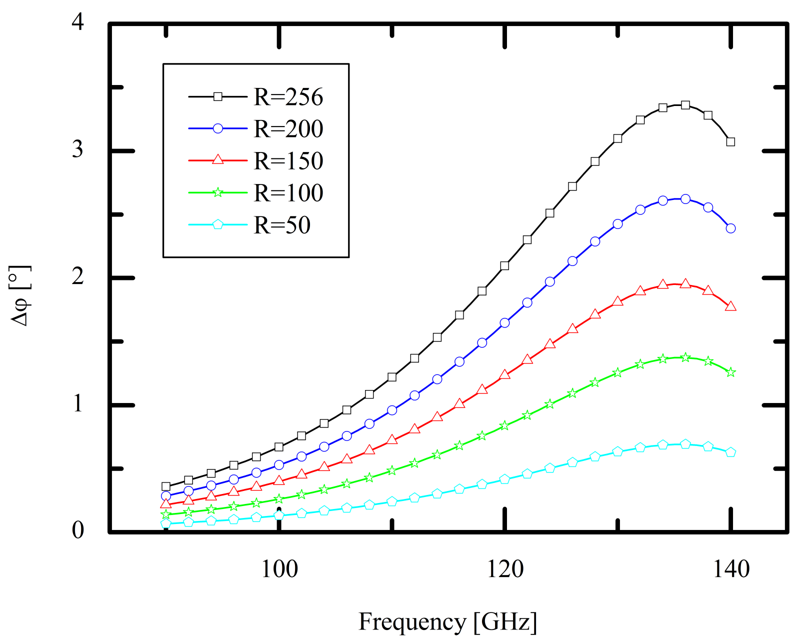

Figure 6-17: *Simulated phase change of the SWTL over frequency.*

and finally all the components were put together in a schematic for simulation of the complete SWTL based on simulated S-parameter data sets. The input reflection and the transmission are depicted in Figs. 6-16a and 6-16b for two switching states, 256 switches and 0 switches. These numbers refer to the metal strips, that are shorted to ground, so that two HBT switches are counted as a single switch and 256 is the number of available phase states in a single SWTL. The number of switches in on-state is expressed by the parameter R, short for register value. These two cases displayed in Figs. 6-16a and 6-16b evoke the highest mismatch of all states in propagation and reflection of the SWTL. It was observed that the highest value for the propagation mismatch is 0.05 dB and for the reflection 0.9 dB. To investigate the phase shift of the line, it was compared to a second SWTL in default state without phase switching. This is also the final type of use for these lines, working in parallel as a reference and a measurement path, as already explained before and illustrated in Fig. 6-1. The resulting phase difference versus frequency is depicted in Fig. 6-17.

To demonstrate the phase variation with respect to the number of metal strips, that are shorted to ground by the HBT, Fig. 6-17 depicts the phase frequency relationship for different switching states ranging from the minimum to the maximum available number of switches. For a fixed frequency, here 120 GHz, the maximum phase shift amounts to $\Delta\varphi = 2.095°$. Fig. 6-18 shows the phase shift versus number of switches in on-state at 120 GHz. The phase resolution is the phase shift for a single switch and was simulated to be $\varphi_{res} = 0.0082°$. The graph depicts the highly linear behavior of the SWTL. This was one crucial criterion for the choice of this structure. The high linearity is attributed to the fact that the phase only scales with the length exhibiting a different $\varepsilon_{r,eff}$ compared to the reference. The physical dimensions can be designed with ultra high accuracy, not only theoretically but also in manufacturing owing to high accuracy lithography procedures. It becomes also clear that those lines can easily be adapted to any desired frequency by simple scaling.

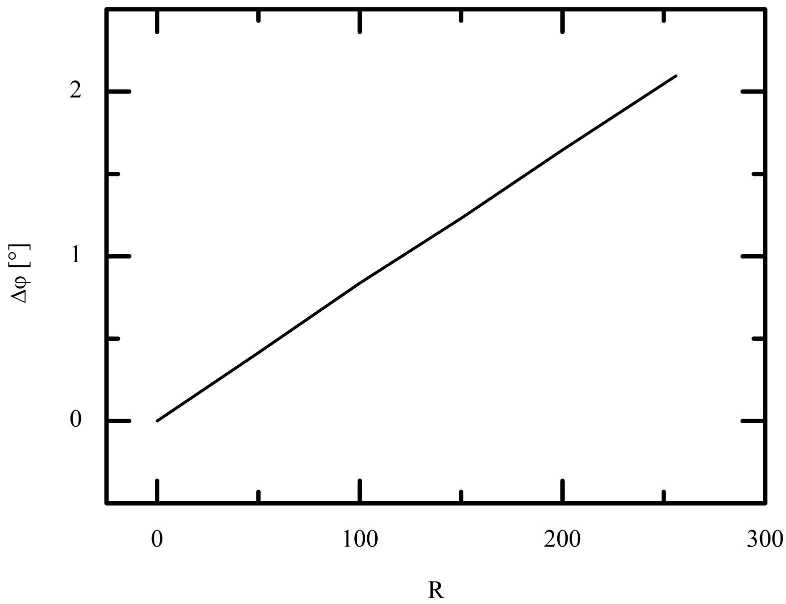

Figure 6-18: *Simulated phase change of the SWTL versus number of switches in on-state (R).*

Further understanding of the SWTL requires to characterize the RF behavior of the HBT switches, since they are the key components for phase manipulation. The transistors are modeled using a vertical bipolar inter-company (VBIC) model. The simulated input impedance of the switch for on and off-state is compared in Figs. 6-19a and 6-19b. It shows that this kind of switch is providing a ground return path in parallel to the metal plane in metal 1 layer that changes its resistance and reactance. In on-state, the switch has an impedance of $Z_{in}|_{f=120\,GHz} = 67.67\,\Omega - j36.12\,\Omega$. In off-state, the impedance is $Z_{in}|_{f=120\,GHz} = 30.71\,\Omega - j106.06\,\Omega$. By altering those properties, the phase constant of the SWTL is manipulated while the attenuation is basically unaffected maintaining the propagation characteristics and assuring symmetrical behavior of both parallel SWTLs, even while operated in different phase states.

For further experiments, a test layout was designed to facilitate S-parameter measure-

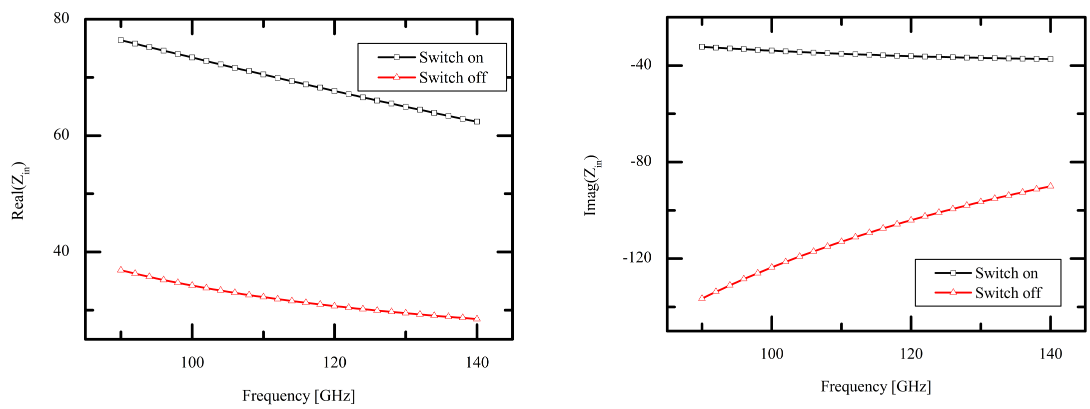

(a) *Real part.* (b) *Imaginary part.*

Figure 6-19: *Simulated input impedance of a single switch.*

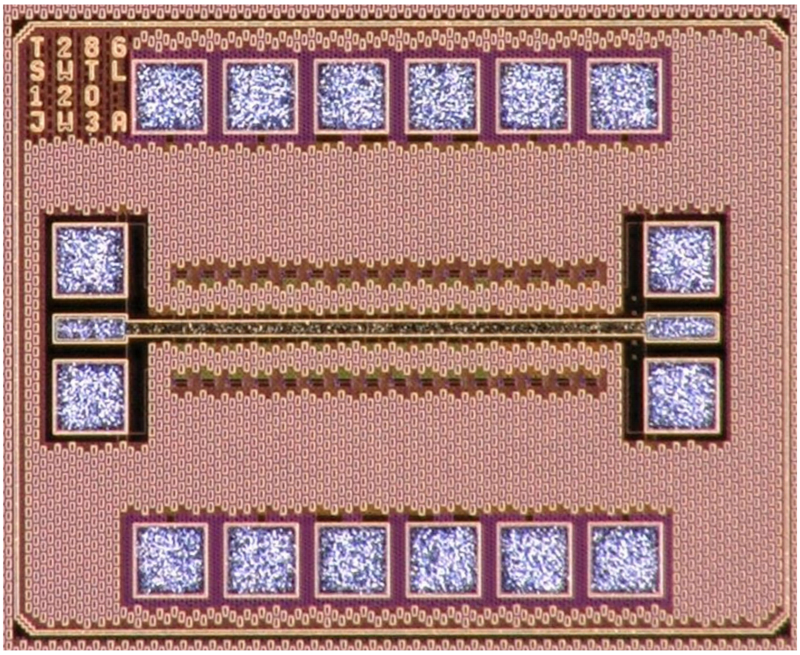

Figure 6-20: *Layout of the SWTL test chip.*

ments. The chip layout is displayed in Fig. 6-20. In the presented design, the strip width as well as the spacing was 15 µm. The basic structure of the demonstrated architecture is a 650 µm long microstrip line, where metal 1 serves as a ground plane to shield the lossy silicon substrate. The microstrip itself is positioned in TM2. Beneath the strip line, 16 strips are placed in metal 4. Metal layer 2 is used for the routing of control signals setting the switches. The pads displayed on the left and the right side in Fig. 6-20 are in ground signal ground (GSG) configuration serving as access point for on-wafer measurements. These measurements were conducted with an Agilent Vector Network Analyzer. In order to keep the number of control pads for these first experiments low, the inner layer metal strips were connected together two by two to the switch and controlled via one DC pad leading to 8 control pads for the whole line. The remaining 4 pads visible in Fig. 6-20 are used for voltage supply and ground connections.

Pull-up resistors, followed by a pair of inverters providing suitable driving capabilities, ensure that by default all switches are turned off. In addition, the first strips, one at each end of the line, were by default connected to ground, in order to ensure a smooth transition interface from the pad to the line. Figures 6-21a and 6-21b display the input reflection S_{11} and transmission S_{21} for the corresponding phase configuration. As it is shown, the circuit exhibits broad band behavior. The maximum return loss is 2 dB and the matching at 115 GHz is −17 dB. The presented SWTL was measured in all available switching states to investigate the phase shift that is induced by toggling a distinct number of switches. The measured scattering parameters were evaluated and the resulting phase is illustrated in Fig. 6-22. The figure shows the phase versus frequency for four different switching states as indicated in the legend. Here, the measurement setup was dimensioned for measurements up to 115 GHz to check the performance. The maximum phase shift that can be achieved with 16 15 µm wide metal stripes is around 1°. Furthermore, it is confirmed by the measurement results depicted in Fig. 6-22 that the phase shifts linearly with a number of switches in on-state owing to an effective length that is altered in its

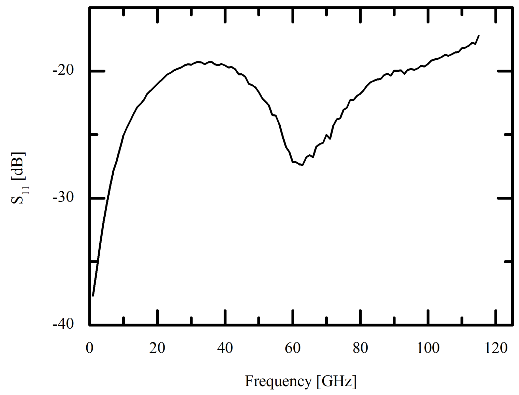

(a) *Reflection S_{11}.*

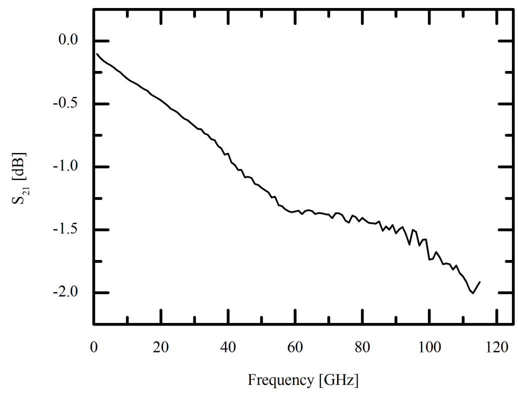

(b) *Transmission S_{21}.*

Figure 6-21: *Measured S-parameters of SWTL test chip.*

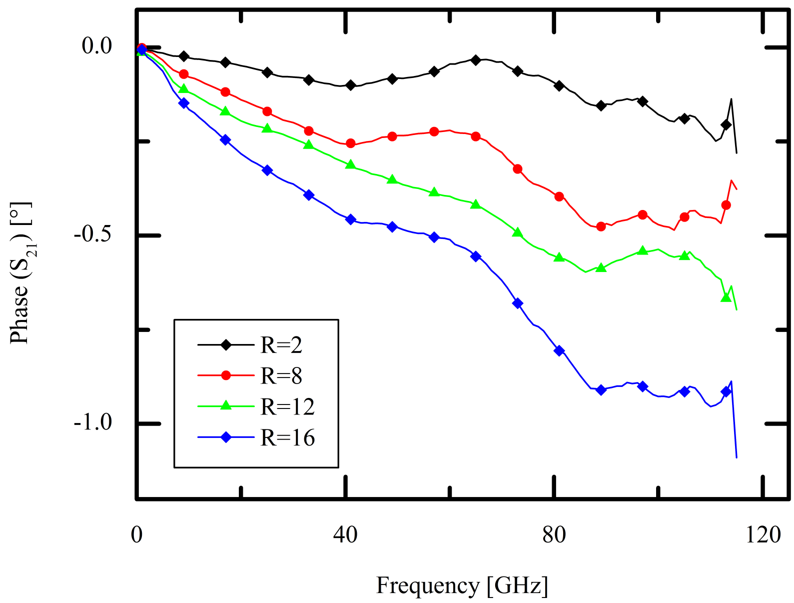

Figure 6-22: *Measured phase of SWTL test chip.*

effective permittivity. The presented results shall proof the assumptions about the SWTL performance made in the beginning of this chapter.

Another crucial aspect for the final SWTL design is a stable performance over all switching states. This is important for the collaboration with the other interferometer components. The SWTL test chip was used to measure the maximum change of input reflections and of the insertion loss for all available switching states of the line. The results, depicted in Fig. 6-23, demonstrate that the input reflections are changing less than 1 dB and the variation in transmission does not exceed 0.15 dB. These values are not achievable with other phase shifting architectures like a switched transmission line type, high-pass/low-pass, reflection-type or vector-summing architecture [119]. The advantages of the SWTL, presented in this section, rendered this topology the preferred phase shifter for the interferometer. The presented results are providing information about the phase difference between the signals in the different switching states, but not an absolute phase delay of the SWTL in the final setup since it is not of interest and therefore not investigated.

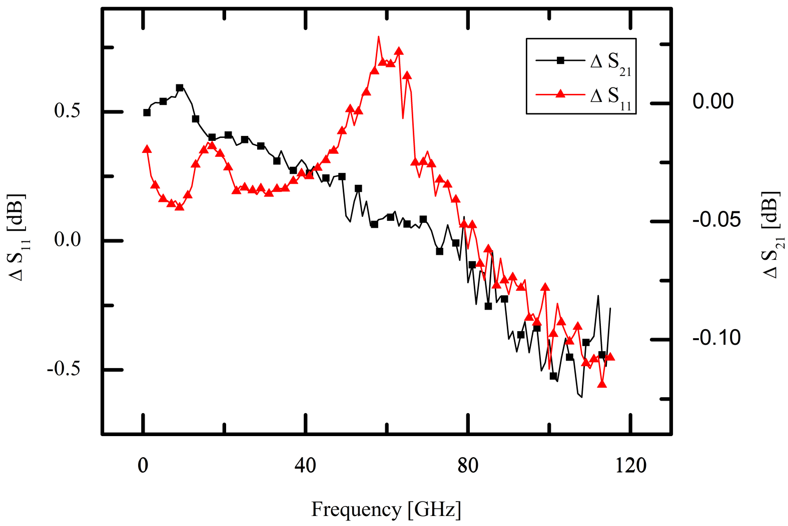

Figure 6-23: *Maximum of the measured S_{11} and S_{21} difference of SWTL test chip for all switching states.*

The effect of the SWTL on the performance of the complete on-chip interferometer is of great importance and is discussed in section 6.5. The scattering parameters of the hybrid ring coupler can be applied to extract the SWTL performance from the overall interferometer measurements and to compare it to the measured results obtained from the test chip. The input reflections and insertion loss of the second test SWTL structures were very similar to the first chip and thus not discussed any further. The maximum changes in the line characteristics were also comparable. However, to be finally able to extract information from sample measurements with the millimeter-wave interferometer, it is required to know the phase shift characteristics of the exact SWTL line that is applied on chip. The test setup that was used for phase measurements is displayed in Fig. 6-24. The upper pads are for power supply and control signals of the switching states. 8 control signals, c_1-c_8, enable 256 switching constellations and hence phase states of the propagated signal. The left pads are pads for RF probe tip accommodation. The complete line is 2.2 mm long and another pair of RF pads is also placed at the end of that line. Thus, transmission measurements become feasible. The maximum available phase shift is achieved when all switches are active so that each strip for dielectric manipulation is pulled to ground. This state is demonstrated by measurement results depicted in Fig. 6-25. The measured phase difference between the two switching state amounts to 2.49°,

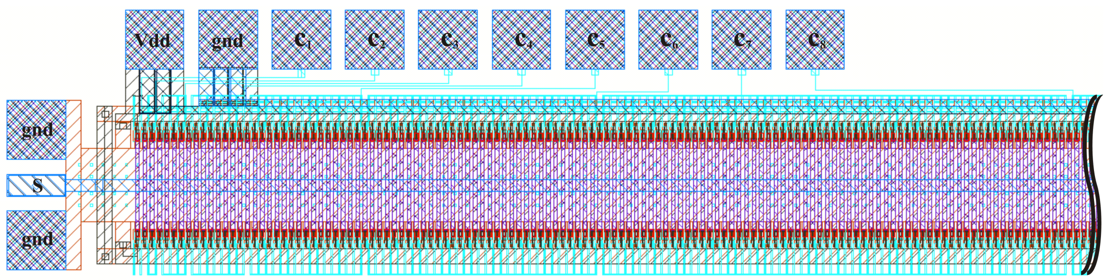

Figure 6-24: *Layout of the final SWTL test chip.*

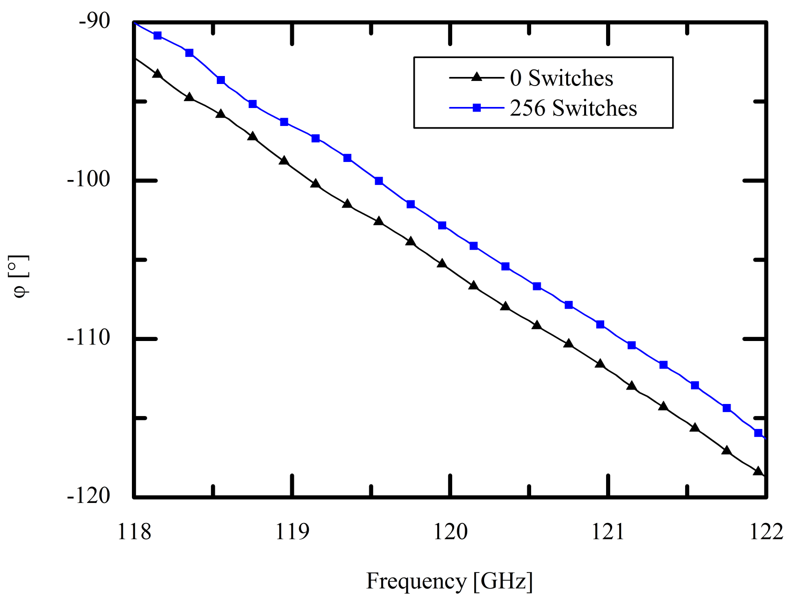

Figure 6-25: *Measured phase from SWTL test chip for two switching states.*

which is the maximum phase shift that can be induced with that particular SWTL. It is 18.9 % higher than expected from simulations. Later in this chapter it is shown how these states can alter the interferometer's quality factor and center frequency.

6.3.4 Low-Noise Amplifier

The complete on-chip interferometer contains a power detector to evaluate the transmitted power and provide a corresponding DC output signal for further processing. In order to achieve a power level at the output suiting the dynamic input range of the power detector, the signal coming from the hybrid ring coupler needs to be amplified. For that purpose, an LNA is inserted. The topology of the LNA is a two-stage cascode circuit as indicated in Fig. 6-26. The circuit topology reported in [120] was adapted and transferred to the technology applied here (SG13G2) featuring higher transistor gain. The cascode topology was chosen to achieve a high gain and good input-output isolation. The input and output matching is realized using transmission lines along with metal-insulator-metal (MIM) capacitors. The amplifier has a gain of about 18 dB working at a 3.3 V supply voltage. This value was obtained measuring the interferometer with and without the LNA. For that purpose, GSG pads are placed in front and behind the LNA on the final chip layout that will be presented in section 6.4. The final circuit following the complete interferometer chain is a power detector. It is described in the following subsection.

6.3.5 Power Detector

The power detector works according to the square law principle based on the nonlinear V-I characteristic function of the HBT transistors that can be described with Schockley's

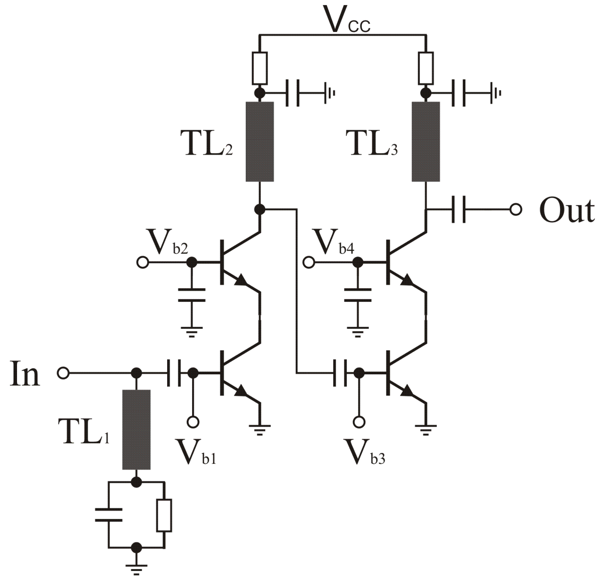

Figure 6-26: *Topology of the two-stage cascode LNA.*

equation.

$$I_C = I_S e^{\frac{V_{BE}}{V_T}} \tag{6-1}$$

V_T is the thermal voltage which is around 26 mV at room temperature, I_S is the reverse saturation current of the base–emitter diode and V_{BE} the base emitter voltage. The circuit topology is shown in Fig. 6-27. L_1 and L_2 compensate the input capacitance to achieve

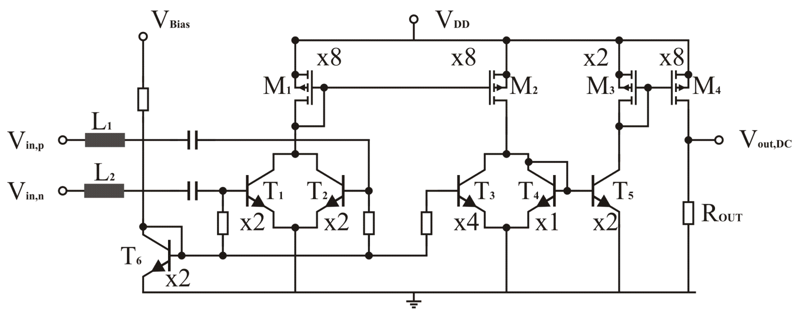

Figure 6-27: *Topology of the power detector and current amplifier.*

input matching. The transistor pair at the input (T_1, T_2) is excited with a differential, sinusoidal RF signal superimposed onto the bias voltage leading to a base emitter voltage of:

$$V_{BE} = V_{BE,bias} + v_{BE} \tag{6-2}$$

The RF signal at each transistor is:

$$v_{BE} = \frac{\hat{v_{RF}}}{2} \cos(\omega t) \tag{6-3}$$

Since the differential input splits up symmetrically to each transistor, the amplitude is $v_{RF}/2$. To understand the function of the power detector, it is necessary to split (6-1) into single terms which is accomplished using the Taylor expansion for an exponential function:

$$e^x = \sum_{n=0}^{\infty} \frac{x^n}{n!} = 1 + x + \frac{x^2}{2} + \cdots \tag{6-4}$$

It can be applied to calculate the sum of the collector currents at the collector node of the transistors T_1 and T_2 in Fig. 6-27 as follows:

$$\begin{aligned} I_{tot} &= i_{c1} + i_{c2} \\ &= 2I_0 + \left(\frac{\hat{v_{RF}}}{2}\right)^2 \frac{I_0}{V_T^2} * \cos^2(\omega t) \\ &= 2I_0 + \hat{v_{RF}}^2 \frac{I_0}{8V_T^2} + \hat{u}^2 \frac{I_0}{8V_T^2} * \cos(2\omega t) \end{aligned} \tag{6-5}$$

It is possible to show that for sufficiently small input signals in the order of −10 dBm and smaller, the sum of both collector currents can be expressed by a quiescent current and an additional DC part proportional to the square of the input signals amplitude neglecting the higher orders of the Taylor expansion. The calculated absolute error using the Taylor expansion for quantifying the DC current evoked by the RF signal is around 100 µA for an input power of −10 dBm. This value is reduced to 31 µA at −30 dBm. For a constant input impedance in the considered frequency band and within the input dynamic range, the sum of the collector currents of T_1 and T_2 displayed in Fig. 6-27 is proportional to the input power. The resulting current can be calculated with the help of (6-5).

The sum of the collector currents is processed using a MOS current mirror (M_1 and M_2) and fed to the next stage composed of three HBT transistors. Transistor T_3 is supposed to withdraw the DC bias current of T_1 and T_2. Therefore, it is equally biased but features double the emitter area of T_1 and T_2. This leaves the DC contribution evoked by the RF signal that is extracted by applying a second current mirror (T_4 and T_5) exhibiting a current gain of 2. Finally, the current is again amplified by a factor of four using another MOS current mirror (M_3 and M_4) and fed to the load resistor R_{OUT} to provide an output voltage which is proportional to the input power.

The detector was also implemented as a standalone test circuit to characterize its transfer function, the DC output voltage versus input power. On-wafer measurements were performed and the results are depicted in Fig. 6-28. The measured conversion function was fitted using a polynomial of the fifth order which is also plotted in Fig. 6-28. The fitting function of the power detector was derived for comparison of S-parameter measurements, conducted on wafer, with the recorded DC output voltage to obtain mutual verification of the results. It is desirable to operate the device in the linear region. This can be accomplished by an adjustable bias voltage as indicated in Fig. 6-27. Depending on the input power level, the bias can be adjusted accordingly for linear output characteristics. The supply voltage impact onto the transfer characteristics were investigated and presented in [16].

However, depending on the transfer function of the passives, it is not always feasible to operate in the linear region of the power detector. It is evident from Fig. 6-2 that the dynamic range to be covered by the detector is high. This further motivates to apply mode

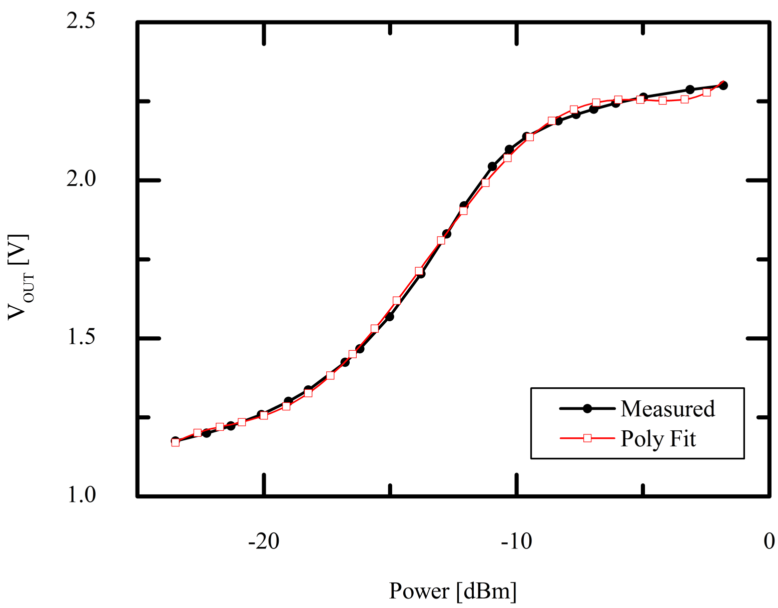

Figure 6-28: *Measurements and* 5*th order polynominal fit of power detector output voltage versus RF input power at* 120 GHz*.*

3, which was introduced in section 6.1, so that linearity of the power detector becomes irrelevant.

The input matching of the detector was accomplished by using simple conductors, $L_1$and L_2 in Fig. 6-27, where width and length were designed to achieve the appropriate inductive behavior since the input of the single detector shows capacitive behavior. The obtained S_{11} by using the proposed method is depicted in Fig. 6-29. The minimum is -12 dB and the matching is better than -8 dB for frequencies above 120 GHz. This final stage is enabling DC readout for the complete on-chip interferometer. The following section presents the setup that was constructed to evaluate the complete interferometer chip experimentally.

6.4 Experimental Setup

The key component of the experimental setup is the chip containing the interferometer, which was developed in the 130 nm SiGe process. A picture of the fabricated chip is depicted in Fig. 6-30. The chip dimensions are 1.2 mm times 6.4 mm. The floor planning is also indicated in the figure. The positioning of the SWTLs, which also defines the location of the microstrip sensing elements, is done for accommodation of the particular microfluidic channel. The intended position is highlighted green in Fig. 6-30. The distance of the lines is 700 µm which is basically determined by the hybrid ring coupler's dimensions. It also defines the sample dimensions within the microfluidic channel to some extent, since one of the lines needs to be covered by a reference liquid and the second one by the MUT. The chip is mounted on an interposer PCB and connected with bond wires. It is placed in a cavity for reduced bond wire lengths. The interposer also contains an SPI connector and connectors to plug it to a second PCB, the motherboard featuring components for PLL operation. The on-chip VCO providing the 120 GHz signal is controlled and stabilized by

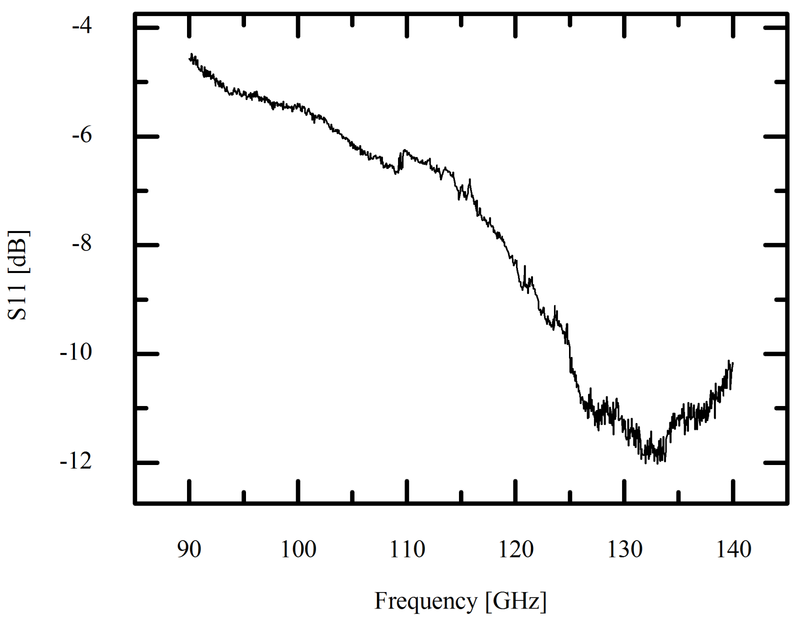

Figure 6-29: *Measured reflection* S_{11} *of power detector.*

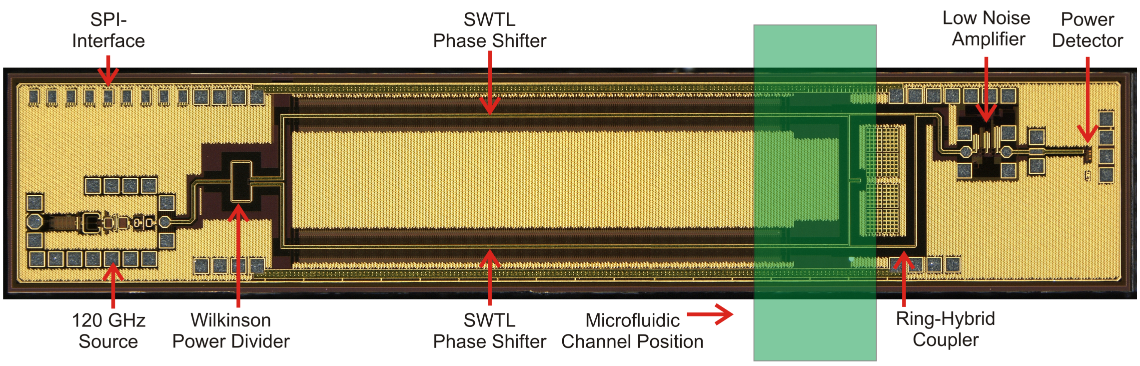

Figure 6-30: *Chip photo of the* 120 GHz *interferometer.*

that. The resulting setup is displayed in Fig. 6-31. The frequency reference signal for the PLL is provided by a signal generator connected through SMA connectors. The frequency of the reference signal is used to tune the RF signal of the VCO. The results obtained with that setup as well as S-parameter measurements are presented in the following section.

6.5 Experimental Results

The PLL motherboard and the external frequency generator were used to perform the frequency sweep. The tuning range of the on-chip VCO allowed for a sweep from 117 GHz to 125 GHz. The results are depicted in Fig. 6-32. The integrated SWTL phase shifters were adjusted by register values R from 0 to 255, resulting in a phase shift of $\Delta\varphi = 2.49°$ at 120 GHz. These values have been determined evaluating the phase measurements displayed in Fig. 6-25.

The passive structures building the core interferomenter behave like a notch filter with a minimum close to 121 GHz, depending on the switching state. For validation, further

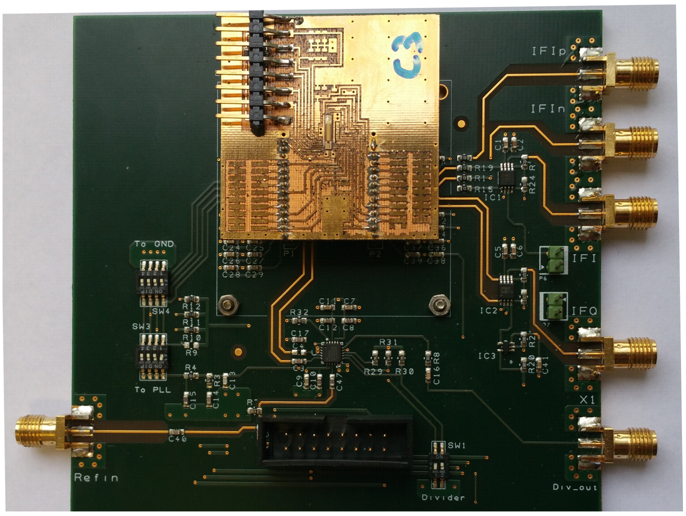

Figure 6-31: *Motherboard, adapter board and interferometer chip.*

S-parameter measurements were conducted. On-wafer probes were attached to the GSG pads in front of the Wilkinson coupler and those behind the LNA, also visible in Fig. 6-30. The measured and simulated transmission is displayed in Fig. 6-33. The simulation results do not include the LNA, since the measurements have been done without power flattening calibration and the absolute power level is not the target parameter. The relevant information here is the notch frequency. Comparing Figs. 6-32 and 6-33, it becomes obvious that the input matching of the power detector has an impact onto the notch shape. Shaping the notch by tuning the phase, a higher Q-factor is achieved and the resulting large dynamic range outweighs the mentioned effect of matching. This is also reflected in the center frequency that was extracted from both measurements and simulations. The results are displayed in Fig. 6-34. The notch frequency obtained from DC measurements

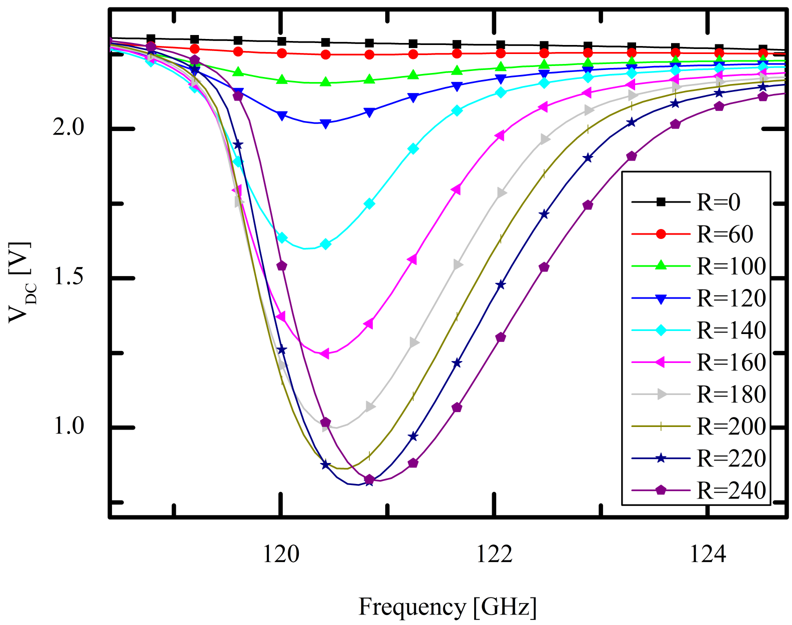

Figure 6-32: *Power detector measurements for different switching states R.*

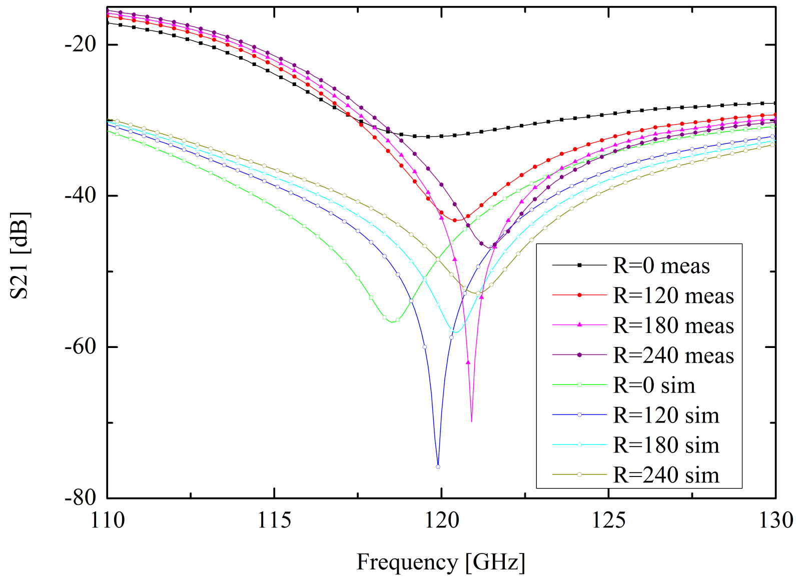

Figure 6-33: *S-parameter measurements and simulations of the interferometer without LNA for different switching states R.*

shows that the mentioned matching effect is compensated for register values higher than 140, implying a 1.37° phase shift induced by the SWTL. Above that, the slope of the curve is approaching the one of the S-parameter-based center frequency detection. It is also in good agreement with simulation results displayed in Fig. 6-34. The sensitivity of the complete system is 763 MHz/°. The corresponding value of the MUT permittivity depends on the respective channel geometry and can be extracted for different channel sizes. The channel geometry is considered to be rectangular and covering a length l_c of the microstrip. The digital output versus the MUTs' permittivities has been calculated for three different channel lengths with the help of (2-23), derived in chapter 2. In (2-23), q_1

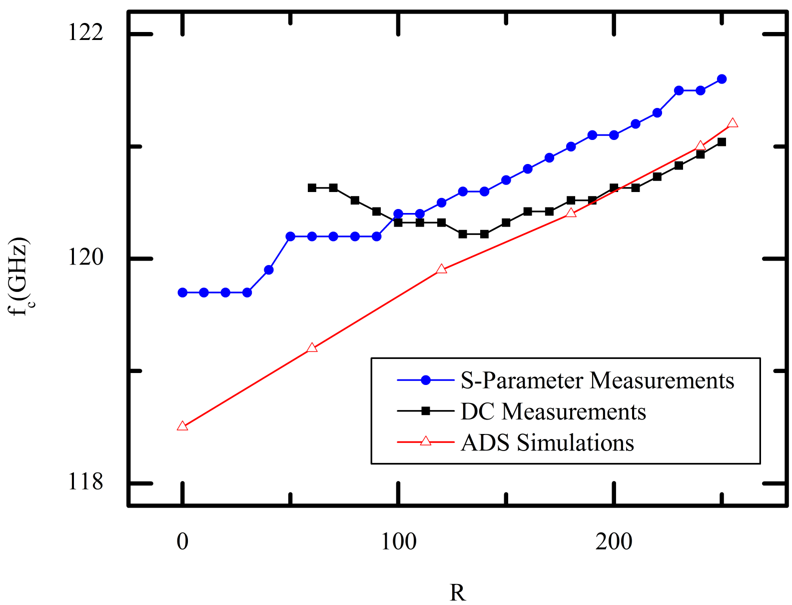

Figure 6-34: *Notch frequency versus number of switches in on-state R.*

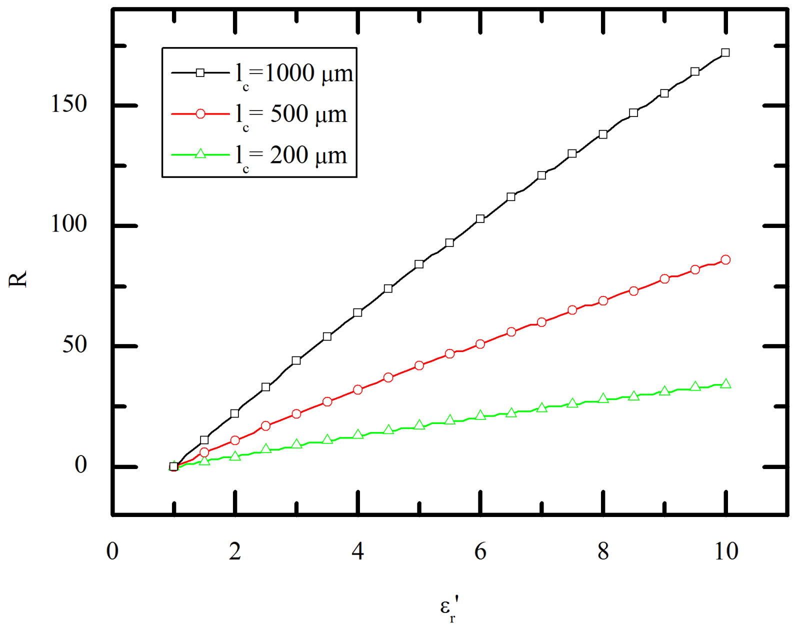

Figure 6-35: *Number of switches in on-state versus ε_r' for different channel lengths l_c.*

Table 6-2: *Table of comparison.*

Ref	Oper. Freq	Resolution	Range	Readout
[73]	125 GHz	0.0125	-	DC
[16]	120 GHz	-	1-8 (sim)	DC
This work	120 GHz	0.052	1-10	DC

and q_2 are filling factors depending on the line geometry which can be calculated using Wheeler's transformation. This provides a closed-form solution to extract a material's permittivity. The effective permittivity ε_{eff} is obtained by direct digital read-out of the phase shift, represented by the switching state R as explained in section 6.1. The result is depicted in Fig. 6-35. The switching state along with the given channel dimensions empower MUT permittivity read out. For a 1 mm wide channel the permittivity resolution is 0.052 and the sensitivity $\Delta R/\Delta\varepsilon = 17$, where R is the number of switches in on-state. These values have been compared to other sensors working in the 120 GHz range as listed in 6-2. The resolution along with the sensitivity can be raised linearly by increasing the channel length at the expense of permittivity range.

6.6 Summary

This chapter presented the development and operation of an electrical on-chip interferometer working at millimeter-wave frequencies. At first, the concept of the on-chip interferometer was demonstrated and discussed with respect to the microwave interferometer PCB from chapter 4. The most prominent differences are the integrated calibration feature and the power detector for data evaluation on chip. The provided chain of integrated components ensures that RF signals are completely handled on chip, so that no RF interface between chip and PCB is required. The integrated circuit components have been demonstrated and discussed. The design and characterization of the 120 GHz switchable microstrip slow-wave transmission lines for phase control have been presented to emphasize the advantages of those circuits which are linearity and stable performance over all switching states.

The remaining active components have also been designed as standalone circuits to characterize their performance experimentally. A microstrip-based permittivity characterization technique was presented along with a numerical strategy to extract material permittivity. The operation modes featured by the interferometer were discussed and the one with the highest accuracy was identified to be based on phase compensation. Applying the proposed technique, dielectric properties of samples can be determined and direct digital read out is enabled. A closed form was derived to extract sample permittivities from phase measurements conducted with the developed device analytically. The resolution and accuracy of the interferometer operated in the mode of choice was discussed and compared to other designs at millimeter-wave frequencies.

From theoretical investigations along with experiments, it can be concluded that the presented system offers a relevant solution for a high-sensitivity dielectric sensor with calibration feature for lab on-chip solutions.

7 Conclusion

7.1 Summary

This thesis presented the development of an ultra sensitive integrated sensor for biomedical purposes. Those applications demand label-free and contactless measurements to avoid contamination of the samples under investigation, as well as deterioration of the sensed parameters. For a suitable spatial resolution as well as miniaturization of sensor systems, high frequency integrated circuits were selected as the best suited technology. Chapter 2 reviewed the different sensing approaches that have been identified from literature studies as potential candidates targeted at the specific objective of this thesis. Before selecting the sensor for implementation, read out circuits and methods were discussed in chapter 3 and their performance in collaboration with the sensing methods were examined. These examinations led to the final choice, the interferometer, as the perfect match with respect to measurement sensitivity and accuracy in the context of biomedical applications. This approach was studied further by conducting experiments at microwave frequencies. The methodology for developing experimental designs was presented in chapter 4. The fabricated PCB was utilized to confirm the findings from theory by measurements with calibration fluids as well as biological cells.

All in all, the objective was to design an ultra compact sensor system for potential lab-on-chip solutions, to avoid bulky and expensive laboratory equipment. For that reason, designs for even higher frequencies in the millimeter-wave range were addressed. Proper investigations of processes at 100 GHz and beyond have been pursued and presented in chapter 5. In the beginning of chapter 5, theory of dielectric matter and dispersive behavior was discussed. Different models to describe relevant samples have been presented and the use of high frequencies for dielectric sample characterization was motivated from theory.

The main result of those investigations were that phase sensitive systems are well suited to characterize dielectric samples also at millimeter-wave frequencies. This was proven by measurements with a continuous wave spectrometer investigating different samples, from tetradecane to yeast cells in glucose as a nutrient solution. To test the feasibility of the targeted SiGe technology, a preexisting 120 GHz sensor was reviewed and used for experiments with yeast in a microfluidic channel. The experiments showed that the chosen technology and the target sensing objective is readily feasible using integrated dielectric sensors in silicon. In summary, those results, theoretical and experimental ones, proved the feasibility of millimeter-wave integrated circuits for screening of dielectric samples. Conclusively, a 120 GHz mixed signal sensor IC was designed and presented in chapter 6.

The technology of choice was briefly discussed and the methodology along with the targeted modes of operation for the interferometer were presented. Finally, on-wafer measurements were compared to results obtained with on-chip detection. The extraction of permittivity values from phase measurements is demonstrated by applying the calculation scheme developed in chapter 2.4. After comparison to other existing millimeter-wave dielectric on-chip sensors which have been published, it is concluded that this work represents a powerful solution for biomedical sensing applications and provides a platform for future lab-on-chip devices.

7.2 Outlook

Experiments with different kinds of yeast cells in a nutrient solution have been conducted at 7 GHz to obtain proof of concept for the interferometer approach as a dielectric sensor for cell detection. Utilizing the microwave interferometer, a simple Teflon tube was feasible as a microfluidic channel and the circuit could be integrated into a microfluidic system by simple PVC joints. Experiments with a 120 GHz transducer, presented in chapter 5.4, showed that even at millimeterwave frequencies it is possible to achieve a suitable penetration depth into liquids inside a capillary to perform dielectric measurements.

The final mixed signal IC was designed for the operation with an integrated microfludic channel. Integrating the microfluidics into the chosen SiGe process as a standard design is still under construction and was not attainable within the scope of this thesis. Still, the function of the developed chipset was thoroughly investigated and demonstrated. The calibration as well as phase compensation could be demonstrated by a built-in test function of the chip. Since both microstrip sensing lines, the sensor and the reference line, are realized as a SWTL phase shifter, the sensing line could be tuned in phase and thus utilized to emulate the phase shift induced by a potential sample under test. Subsequently, the SWTL of the sensing path could be used for phase compensation to determine the respective phase shift which is indicated by the switching state of the reference SWTL. This value is available from a SPI register and it is the feature of direct digital read-out of the phase shift induced by a potential sample under test.

The integration of microfluidic channels in silicon has been demonstrated experimentally along with the transducer circuit discussed in chapter 5.4. The setup is briefly reviewed

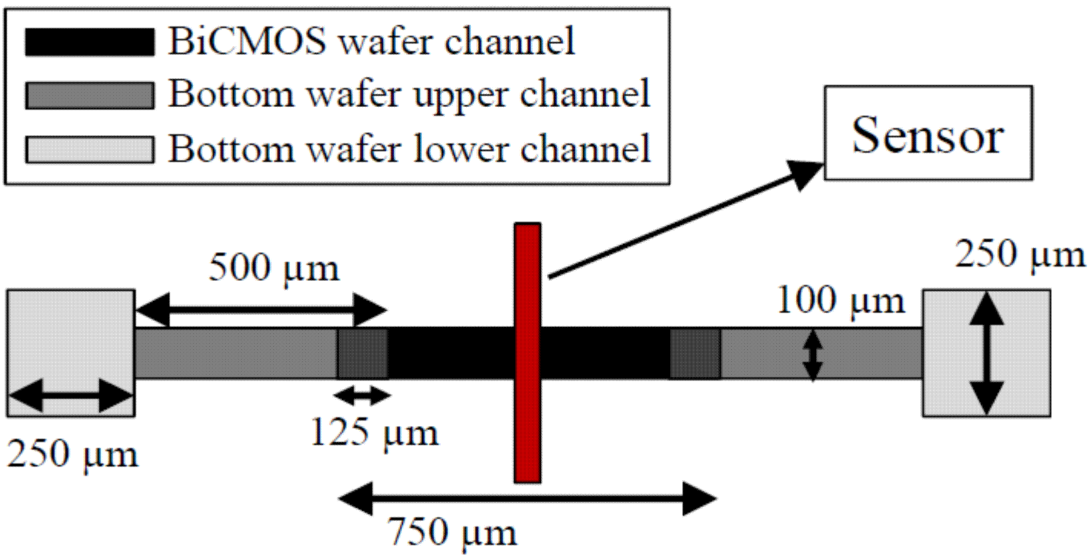

Figure 7-1: *Dimensions of the microfluidic channels for both BiCMOS wafer and bottom wafer [121].*

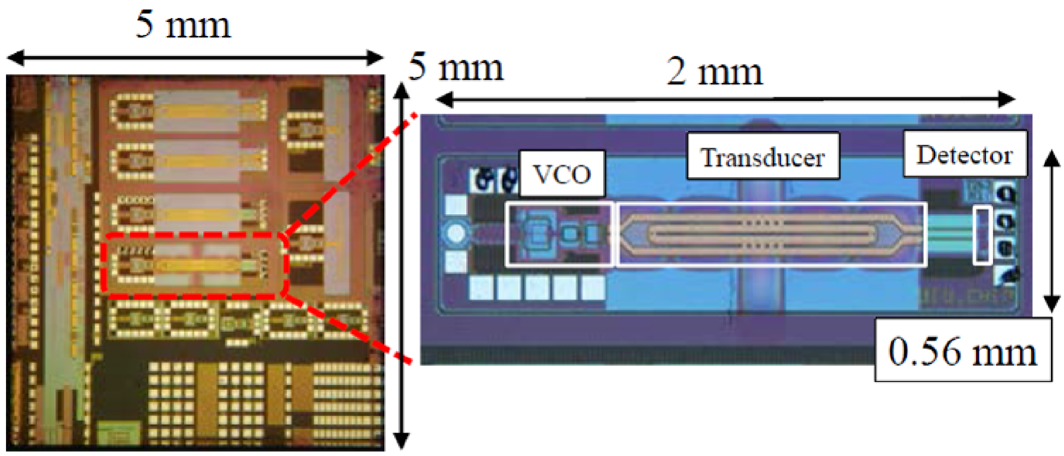

Figure 7-2: *Photograph of (5x5 mm2) test chip (left) with zoom-in of test circuit (right) [121].*

and the technology is demonstrated to prove suitable for a future lab-on-chip system based on the interferometer IC developed in this thesis. Integrated microfluidic channels in the utilized silicon technology along with a millimeter-wave dielectric sensor have been presented in [121]. A schematic view of the principle setup is depicted in Fig. 7-1. It displays the layout and the dimensions of the fabricated microfluidic channels. The dimensions are chosen to achieve a laminar flow with flow rates in target applications. The layout of the final experimental setup for demonstration in [121] is depicted in Fig. 7-2. A photograph of the wafer die is shown in Fig. 7-2 on the left. This size is needed to accommodate the microfluidic components like inlet and outlet. On the right side a zoom onto the transducer layout and the active peripheral components are displayed. In that figure, the channel is visible in the middle of the transducer perpendicular to the direction of wave

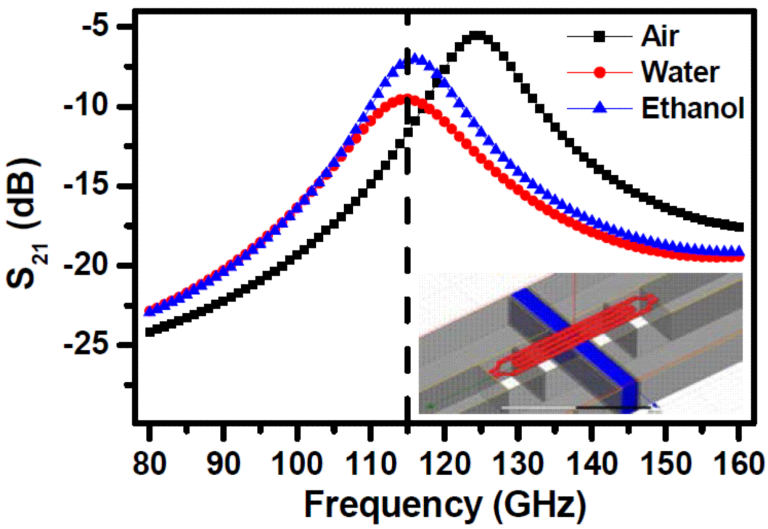

Figure 7-3: *S-parameter simulation results of the transducer using HFSS EM solver. [121].*

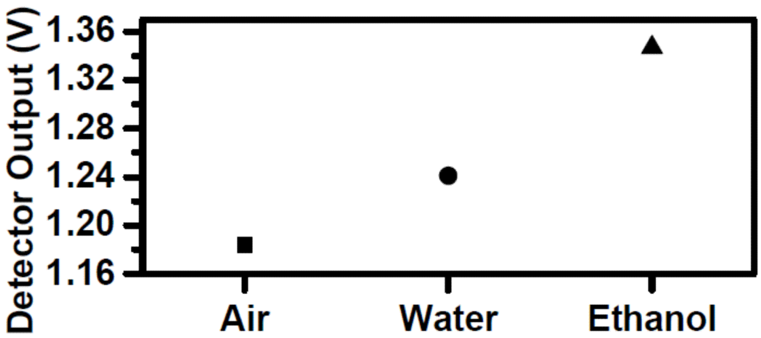

Figure 7-4: *Measurement results of the detector output for the cases of air, water and ethanol [121].*

propagation. The design in Fig. 7-2 was tested measuring several fluids like ethanol and water and compared to a reference measurement with an empty channel, so that only air was inside. The center frequency of the transducer circuit was shifted by the influence of dielectric samples. The effect was recorded using the on-chip power detector. To predict the transducer response to liquids under test, S-parameters have been obtained by HFSS simulations. The results are displayed in Fig. 7-3. The results measured with the chip set are depicted in Fig. 7-4. The change of the detector output, which is 60 mV for water and 160 mV for ethanol with respect to the reference measurement with air, agrees well with the simulation results shown in Fig. 7-3. The investigations and experiments presented proof the feasibility of dielectric sensing at 120 GHz with integrated microfluidics.

The final lab-on-chip sensor will be endowed with the integrated microfluidic channel as demonstrated in [121]. The fabrication process scheme for constructing microfluidic channels is based on wafer-level bonding and structuring. The single parts from the example setup with the transducer are depicted in Fig. 7-5. The process flow is as follows:

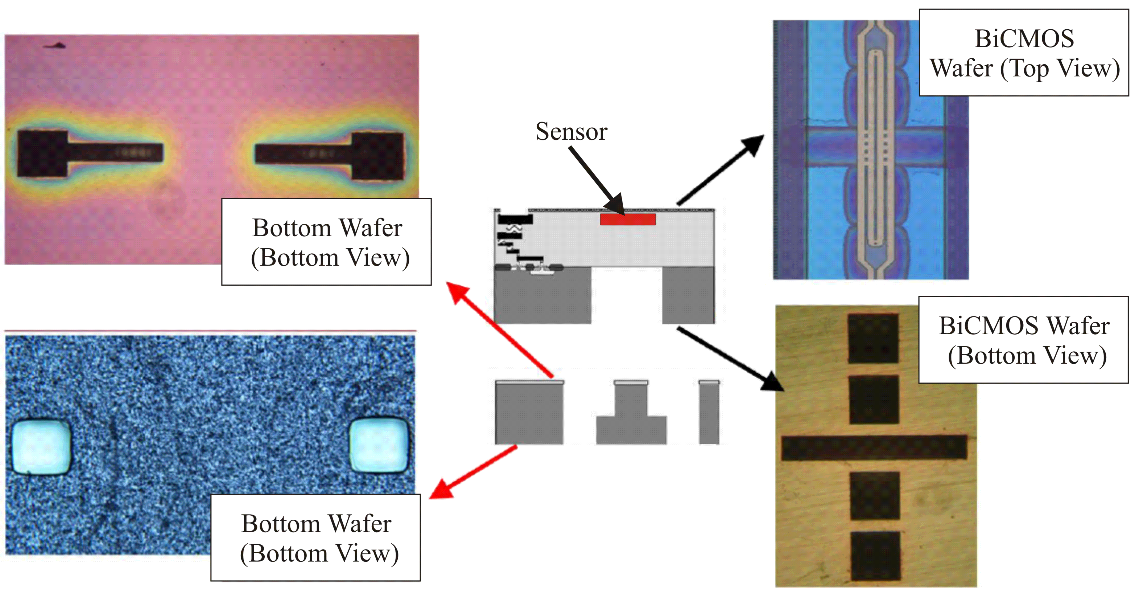

Figure 7-5: *Setup of the integrated microfluidics [121].*

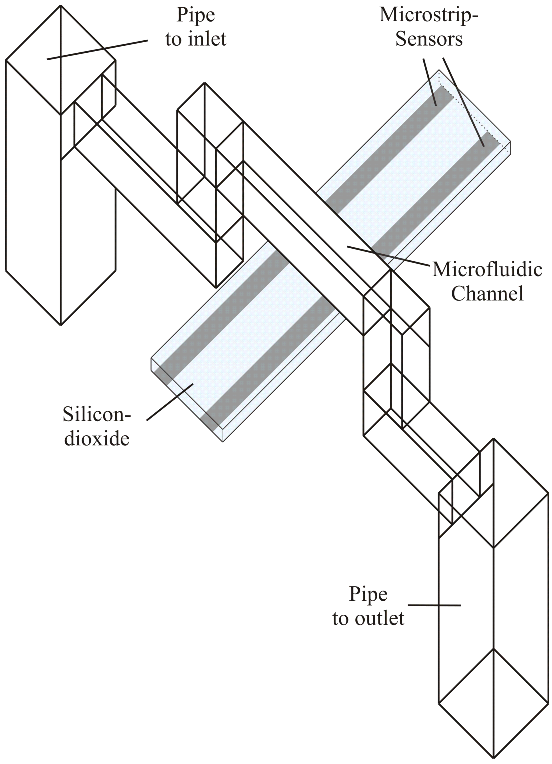

Figure 7-6: *Integrated microfluidic channel beneath reference and sensing line of the on-chip interferometer.*

Two wafers are needed for the setup. After the BiCMOS process is finished, deep reactive ion etching (RIE) is used below the particular sensor structure. The surface on the backside of this wafer must be smooth so that wafer level bonding accomplished by oxide fusion becomes feasible. This is achieved by chemical mechanical polishing. The bottom wafer is structured by stepped RIE processes using SiO_2 hard masks to design the desired vertical profile. The bottom part that is finally obtained is also depicted in Fig. 7-5. As a next step, the bottom and the BiCMOS wafer are bonded by plasma activation, wafer alignment and annealing. This ensures a strong bond and avoids leakage from the microfluidic channel later on. The SiO_2 on the backside of both wafers must be erased. This last step is realized by a dry etch process.

Using that exact fabrication procedure, the design will be endowed with a microfluidic channel integrated in silicon. The schematic 3D drawing in Fig. 7-6 shows the principle setup. The in- and outlets can be connected to a segmented flow system presented in chapter 1, displayed in Figs.1-1 and 1-2. This step is essential, since the interferometer approach is based on the comparison between a sensing line and a reference line. In the segmented flow system, the liquid of interest is confined by a hydrophobe medium, tetradecane, to form little compartments within the microfluidic channel. The flow ratio can be adjusted so that one line of the interferometer is covered by tetradecane, and the other one is covered by a compartment with the sample under test. The interferometer conducts a comparison between both lines so that the extraction of the liquid's permittivity and with that the cell count is feasible. That way, the developed interferometer can be applied for contactless and label-free monitoring of microorganism cultivation progress in a lab-on-chip constellation.

Bibliography

[1] J. Wessel, K. Schmalz, J. C. Scheytt, and D. Kissinger, "Sensitive permittivity detector for dielectric samples at 120 GHz," in *Proc. IEEE Radio Wireless Symp.* IEEE, 2018, pp. 1–3.

[2] ——, "A 120-GHz electrical interferometer for contactless permittivity measurements with direct digital read-out," *IEEE Microw. Wireless Compon. Lett.*, vol. 27, no. 2, pp. 198–200, 2017.

[3] J. Wessel, K. Schmalz, C. Meliani, B. P. Cahill, and J. C. Scheytt, "A 7 GHz biosensor for permittivity change with enhanced sensitivity through phase compensation," in *Proc. Eur. Microw. Conf.* IEEE, 2014, pp. 699–702.

[4] J. Wessel, K. Schmalz, J. C. Scheytt, and C. Meliani, "Switchable slow wave transmission line in 130 nm SiGe technology at 115 GHz for phase detection based biosensors," in *Proc. IEEE MTT-S Int. Microw. Symp.* IEEE, 2014, pp. 1–3.

[5] J. Wessel, K. Schmalz, G. Gastrock, B. P. Cahill, and C. Meliani, "Contactless investigations of yeast cell cultivation in the 7 GHz and 240 GHz ranges," in *Proc. Journal of Physics: Conference Series*, vol. 434, no. 1. IOP Publishing, 2013, p. 012033.

[6] J. Wessel, K. Schmalz, B. P. Cahill, G. Gastrock, and C. Meliani, "Contactless characterization of yeast cell cultivation at 7 GHz and 240 GHz," in *Proc. IEEE Topical Conf. Biomed. Wireless Technol. Netw. Sens. Syst.* IEEE, 2013, pp. 70–72.

[7] J. Wessel, K. Schmalz, J. C. Scheytt, B. P. Cahill, and G. Gastrock, "Microwave biosensor for characterization of compartments in teflon capillaries," in *Proc. Eur. Microw. Conf.* IEEE, 2012, pp. 534–537.

[8] F. I. Jamal, S. Guha, M. H. Eissa, J. Borngräber, C. Meliani, H. J. Ng, D. Kissinger, and J. Wessel, "Low-power miniature K-band sensors for dielectric characterization of biomaterials," *IEEE Transactions on Microwave Theory and Techniques*, vol. 65, no. 3, pp. 1012–1023, 2017.

[9] S. Vogt, M. Detert, D. Wagner, J. Wessel, R. Ramzan, W. Nimphius, A. Ramaswamy, S. Guha, C. Wenger, F. I. Jamal, M. H. Eissa, U. Schumann, B. Schmidt, G. Rose, C. Dahl, I. Rolfe, G. Notzon, C. Baer, and T. Musch, "A newly developed mm-wave sensor for detecting plaques of arterial vessels," *The Thoracic and Cardiovascular Surgeon*, 2017.

[10] M. H. Eissa, F. I. Jamal, S. Guha, C. Meliani, D. Kissinger, and J. Wessel, "Low-power planar complex dielectric sensor with DC readout circuit in a BiCMOS technology," in *Proc. IEEE MTT-S Int. Microw. Symp.* IEEE, 2016, pp. 1–3.

[11] F. I. Jamal, S. Guha, M. H. Eissa, J. Borngräber, C. Meliani, D. Kissinger, and J. Wessel, "Comparison of microstrip stub resonators for dielectric sensing in low-power K-band VCO," in *Proc. IEEE Topical Conf. Biomed. Wireless Technol. Netw. Sens. Syst.* IEEE, 2016, pp. 59–62.

[12] F. I. Jamal, S. Guha, M. H. Eissa, C. Meliani, D. Kissinger, and J. Wessel, "A 24 GHz dielectric sensor based on distributed architecture," in *Proc. German Microw. Conf.* IEEE, 2016, pp. 173–176.

[13] D. Wagner, F. I. Jamal, S. Guha, C. Wenger, J. Wessel, D. Kissinger, D. Ernst, K. Pitschmann, B. Schmidt, and M. Detert, "Packaging of a BiCMOS sensor on a catheter tip for the characterization of atherosclerotic plaque," in *Proc. IEEE Electron. Syst. Integr. Technol. Conf.* IEEE, 2016, pp. 1–3.

[14] H. J. Ng, J. Wessel, D. Genschow, R. Wang, Y. Sun, and D. Kissinger, "Miniaturized 122 GHz system-on-chip radar sensor with on-chip antennas utilizing a novel antenna design approach," in *Proc. IEEE MTT-S Int. Microw. Symp.*, 2016, pp. 1–4.

[15] F. I. Jamal, S. Guha, M. H. Eissa, C. Meliani, H. J. Ng, D. Kissinger, and J. Wessel, "A fully integrated low-power K-band chem-bio-sensor with on-chip DC read-out in SiGe BiCMOS technology," in *Proc. Eur. Microw. Conf.* IEEE, 2016, pp. 273–276.

[16] K. Schmalz, J. Borngräber, M. Kaynak, W. Winkler, J. Wessel, M. Neshat, and S. Safavi-Naeini, "A 120 GHz dielectric sensor in SiGe BiCMOS," *IEEE Microw. Wireless Compon. Lett.*, vol. 23, no. 1, pp. 46–48, 2013.

[17] E. Caplice and G. F. Fitzgerald, "Food fermentations: role of microorganisms in food production and preservation," *Int. J. Food Microbiol.*, vol. 50, no. 1, pp. 131–149, 1999.

[18] J. L. Adrio and A. L. Demain, "Microbial enzymes: tools for biotechnological processes," *Biomolecules*, vol. 4, no. 1, pp. 117–139, 2014.

[19] M. R. Rondon, R. M. Goodman, and J. Handelsman, "The earths bounty: assessing and accessing soil microbial diversity," *Trends Biotechnol.*, vol. 17, no. 10, pp. 403–409, 1999.

[20] K. Lemke, T. Förster, R. Römer, M. Quade, S. Wiedemeier, A. Grodrian, and G. Gastrock, "A modular segmented-flow platform for 3D cell cultivation," *J. Biotechnol.*, vol. 205, pp. 59–69, 2015.

[21] M. S. Boybay, A. Jiao, T. Glawdel, and C. L. Ren, "Microwave sensing and heating of individual droplets in microfluidic devices," *Lab. Chip*, vol. 13, no. 19, pp. 3840–3846, 2013.

[22] H. Kim, S. Vishniakou, and G. W. Faris, "Petri dish PCR: laser-heated reactions in nanoliter droplet arrays," *Lab. Chip*, vol. 9, no. 9, pp. 1230–1235, 2009.

[23] F. Guo, M. I. Lapsley, A. A. Nawaz, Y. Zhao, S.-C. S. Lin, Y. Chen, S. Yang, X.-Z. Zhao, and T. J. Huang, "A droplet-based, optofluidic device for high-throughput, quantitative bioanalysis," *Anal. Chem.*, vol. 84, no. 24, pp. 10 745–10 749, 2012.

[24] L. Rayleigh, "Lvi. on the influence of obstacles arranged in rectangular order upon the properties of a medium," *The London, Edinburgh, and Dublin Philosophical Magazine and Journal of Science*, vol. 34, no. 211, pp. 481–502, 1892.

[25] O. Wiener, *Die Theorie des Mischkörpers für das Feld der stationären Strömung*. Teubner, 1912.

[26] K. W. Wagner, “Erklärung der dielektrischen Nachwirkungsvorgänge auf Grund maxwellscher Vorstellungen,” *Electrical Engineering (Archiv fur Elektrotechnik)*, vol. 2, no. 9, pp. 371–387, 1914.

[27] “Kultivierungsverfahren,” https://www.iba-heiligenstadt.de/fachbereiche/bioprozesstechnik/kultivierungsverfahren/, accessed: 2018-01-12.

[28] H. Rücker and B. Heinemann, “SiGe BiCMOS technology for mm-wave systems,” in *Proc. IEEE int. SoC Design Conf.* IEEE, 2012, pp. 266–268.

[29] W. Olthuis, W. Streekstra, and P. Bergveld, “Theoretical and experimental determination of cell constants of planar-interdigitated electrolyte conductivity sensors,” *Sens. Actuators, B*, vol. 24, no. 1, pp. 252–256, 1995.

[30] T.-T. Ngo, H. Shirzadfar, D. Kourtiche, and M. Nadi, “A planar interdigital sensor for bio-impedance measurement: theoretical analysis, optimization and simulation,” *Journal of Nano-and Electronic Physics*, vol. 6, no. 1, pp. 1011–1, 2014.

[31] M. R. R. Khan and S.-W. Kang, “Highly sensitive multi-channel idc sensor array for low concentration taste detection,” *Sensors*, vol. 15, no. 6, pp. 13 201–13 221, 2015.

[32] J. W. Kim, P. Pasupathy, S. Zhang, and D. P. Neikirk, “Measurement of liquid complex dielectric constants using non-contact sensors,” in *Proc. IEEE Sensors*. IEEE, 2009, pp. 2017–2020.

[33] S. Guha, M. Lisker, A. Trusch, A. Wolf, C. Meliani, and C. Wenger, “12 GHz CMOS MEMS Lab-on-chip system for detection of concentration of suspended particles in bio-suspensions.” in *Proc. BIODEVICES*, 2015, pp. 49–57.

[34] H. Choi, J. Nylon, S. Luzio, J. Beutler, and A. Porch, “Design of continuous non-invasive blood glucose monitoring sensor based on a microwave split ring resonator,” in *Proc. IEEE MTT-S Int. Microw. Works. Series RF and Wireless Technol. for Biomed. and Healthc. App.* IEEE, 2014, pp. 1–3.

[35] B. W. Hakki and P. D. Coleman, “A dielectric resonator method of measuring inductive capacities in the millimeter range,” *IRE Trans. Microwave Theory Tech.*, vol. 8, no. 4, pp. 402–410, 1960.

[36] U. Schwerthoeffer, C. Warter, R. Weigel, and D. Kissinger, “A microstrip resonant biosensor for aqueous glucose detection in microfluidic medical applications,” in *Proc. IEEE Topical Conf. Biomed. Wireless Technol. Netw. Sens. Syst.* IEEE, 2014, pp. 55–57.

[37] N. Y. Kim, R. Dhakal, K. K. Adhikari, E. S. Kim, and C. Wang, “A reusable robust radio frequency biosensor using microwave resonator by integrated passive device technology for quantitative detection of glucose level,” *Biosens. Bioelectron.*, vol. 67, pp. 687–693, 2015.

[38] A. K. Verma, V. Tyagi, and D. Chakraverty, “Input impedance of probe-fed multilayer rectangular microstrip patch antenna using the modified wolff model,” *Microwave Opt. Technol. Lett.*, vol. 31, no. 3, pp. 237–239, 2001.

[39] S. Vehring, S. Guha, F. I. Jamal, D. Kissinger, and C. Meliani, “Permittivity sensor based on 60 GHz patch antenna,” in *Proc. German Microw. Conf.* IEEE, 2015, pp. 311–314.

[40] C. Deffendol and C. Furse, "Microstrip antennas for dielectric property measurement," in *Proc. IEEE Antennas Propag. Society Int. Symp.*, vol. 3. IEEE, 1999, pp. 1954–1956.

[41] E. M. Cheng, M. Fareq, A. B. Shahriman, R. Mohd Afendi, Y. S. Lee, S. F. Khor, W. H. Tan, M. N. Nashrul Fazli, A. Z. Abdullah, and M. A. Jusoh, "Development of microstrip patch antenna sensing system for salinity and sugar detection in water," *Int. J. of Mechanical & Mechatronics Engineering*, vol. 14, pp. 31–36, 2014.

[42] M. Bogosanovich, "Microstrip patch antenna sensor for measurement of the permittivity of homogeneous dielectric materials," in *Proc. IEEE Instrum. Meas. Technol. Conf.*, vol. 1. IEEE, 1999, pp. 31–36.

[43] C. A. Balanis, "Antenna theory: a review," *Proc. IEEE*, vol. 80, no. 1, pp. 7–23, Jan 1992.

[44] P. Silvester and P. Benedek, "Equivalent capacitances of microstrip open circuits," *IEEE Transactions on Microwave Theory and Techniques*, vol. 20, no. 8, pp. 511–516, Aug 1972.

[45] E. O. Hammerstad, "Equations for microstrip circuit design," in *Proc. Eur. Microw. Conf.* IEEE, 1975, pp. 268–272.

[46] C. A. Balanis, *Antenna theory analysis and design*. John Wiley & Sons Inc., New York, 1982.

[47] D. M. Pozar, "Rigorous closed-form expressions for the surface wave loss of printed antennas," *Electron. Lett.*, vol. 26, no. 13, pp. 954–956, 1990.

[48] R. T. Sheldon, "Radio frequency and capacitive sensors for dielectric characterization of low-conductivity media," *Iowa State University Digital Repository*, 2015. [Online]. Available: http://lib.dr.iastate.edu/etd/14862

[49] A. K. Verma, Nasimuddin, and A. S. Omar, "Microstrip resonator sensors for determination of complex permittivity of materials in sheet, liquid and paste forms," *IEE Proceedings-Microwaves, Antennas and Propagation*, vol. 152, no. 1, pp. 47–54, 2005.

[50] G. Moradi and M. Mosalanejad, "Microstrip patch sensors for complex permittivity measurement of medium loss liquids using 3D-fdtd." *Applied Computational Electromagnetics Society Journal*, vol. 32, no. 4, 2017.

[51] T. Marsland and S. Evans, "Dielectric measurements with an open-ended coaxial probe," in *Proc. IEE H (Microwaves, Antennas and Propagation)*, vol. 134, no. 4. IET, 1987, pp. 341–349.

[52] M. Hofmann, G. Fischer, R. Weigel, and D. Kissinger, "Microwave-based noninvasive concentration measurements for biomedical applications," *IEEE Trans. Microw. Theory Techn.*, vol. 61, no. 5, pp. 2195–2204, 2013.

[53] M. A. Stuchly and S. S. Stuchly, "Coaxial line reflection methods for measuring dielectric properties of biological substances at radio and microwave frequencies-a review," *IEEE Trans. Instrum. Meas.*, vol. 29, no. 3, pp. 176–183, 1980.

[54] G. B. Gajda, "A method for the measurement of permittivity at radio and microwave frequencies," *IEEE Sym. MIT Society*, pp. 112–118, 1982.

[55] D. M. Pozar, *Microwave engineering*. John Wiley & Sons, 2009.

[56] H. A. Wheeler, "Transmission-line properties of parallel wide strips by a conformal-mapping approximation," *IEEE Trans. Microw. Theory Techn.*, vol. 12, no. 3, pp. 280–289, 1964.

[57] ——, "Transmission-line properties of parallel strips separated by a dielectric sheet," *IEEE Trans. Microw. Theory Techn.*, vol. 13, no. 2, pp. 172–185, 1965.

[58] J. Svacina, "Analysis of multilayer microstrip lines by a conformal mapping method," *IEEE Trans. Microw. Theory Techn.*, vol. 40, no. 4, pp. 769–772, 1992.

[59] E. Yamashita, "Variational method for the analysis of microstrip-like transmission lines," *IEEE Trans. Microw. Theory Techn.*, vol. 16, no. 8, pp. 529–535, 1968.

[60] E. Yamashita and K. Atsuki, "Strip line with rectangular outer conductor and three dielectric layers," *IEEE Trans. Microw. Theory Techn.*, vol. 18, no. 5, pp. 238–244, 1970.

[61] A. Farrar and A. T. Adams, "Multilayer microstrip transmission lines (short papers)," *IEEE Trans. Microw. Theory Techn.*, vol. 22, no. 10, pp. 889–891, 1974.

[62] H. P. Schwan, R. J. Sheppard, and E. H. Grant, "Complex permittivity of water at 25 c," *The Journal of Chemical Physics*, vol. 64, no. 5, pp. 2257–2258, 1976.

[63] M. A. Couker and L. J. Kushner, "A microstrip phase-trim device using a dielectric overlay," *IEEE Trans. Microw. Theory Techn.*, vol. 42, no. 11, pp. 2023–2026, 1994.

[64] R. M. Fuoss, "Dielectric materials and applications," *J. Chem. Educ.*, vol. 32, no. 4, p. 236, 1955. [Online]. Available: http://dx.doi.org/10.1021/ed032p236.3

[65] K. B. Khalid, T. S. M. Maclean, M. Razaz, and P. W. Webb, "Analysis and optimal design of microstrip sensors," *IEEE Proceedings H - Microwaves, Antennas and Propagation*, vol. 135, no. 3, pp. 187–195, Jun 1988.

[66] I. J. Bahl and R. Garg, "Simple and accurate formulas for a microstrip with finite strip thickness," *Proceedings of the IEEE*, vol. 65, no. 11, pp. 1611–1612, 1977.

[67] M. V. Schneider, "Microstrip lines for microwave integrated circuits," *The Bell System Technical Journal*, vol. 48, no. 5, pp. 1421–1444, May 1969.

[68] P. Silvester, "TEM wave properties of microstrip transmission lines," in *Proc. of the Institution of Electrical Engineers*, vol. 115, no. 1. IET, 1968, pp. 43–48.

[69] A. Barghouthi and F. Ellinger, "Design of a 54 to 63 GHz differential common collector SiGe colpitts VCO," in *Proc. Int. Conf. Microw. Radar Wireless Commun.* IEEE, 2010, pp. 1–4.

[70] H. Li and H.-M. Rein, "Millimeter-wave VCOs with wide tuning range and low phase noise, fully integrated in a SiGe bipolar production technology," *IEEE J. Solid-State Circuits*, vol. 38, no. 2, pp. 184–191, 2003.

[71] U. L. Rohde, "Microwave and wireless synthesizers: Theory and applications," *John Wiley& Sons, New York, NY*, 1997.

[72] J. W. M. Rogers and C. Plett, *Radio frequency integrated circuit design*. Artech House, 2010.

[73] B. Laemmle, K. Schmalz, J. C. Scheytt, R. Weigel, and D. Kissinger, "A 125-GHz permittivity sensor with read-out circuit in a 250-nm SiGe BiCMOS technology," *IEEE Trans. Microw. Theory Techn.*, vol. 61, no. 5, pp. 2185–2194, 2013.

[74] A. L. Samuel, "An oscillographic method of presenting impedances on the reflection-coefficient plane," *Proc. IRE*, vol. 35, no. 11, pp. 1279–1283, 1947.

[75] I. Nasr, J. Nehring, K. Aufinger, G. Fischer, R. Weigel, and D. Kissinger, "Single-and dual-port 50-100-GHz integrated vector network analyzers with on-chip dielectric sensors," *IEEE Transactions on Microwave Theory and Techniques*, vol. 62, no. 9, pp. 2168–2179, 2014.

[76] C. Song and P. Wang, "A radio frequency device for measurement of minute dielectric property changes in microfluidic channels," *Appl. Phys. Lett.*, vol. 94, no. 2, p. 023901, 2009.

[77] H. F. Laminates, "Ro3000® series circuit materials," *RO3010, ROGERS corporation, USA*, 1998.

[78] R. Corporations, "Ro3000 series high frequency circuit materials," *Internet, http://www. rogerscorporation. com/mwu/pdf/3000data. pdf*, 2005.

[79] E. O. Hammerstad and O. Jensen, "Accurate models for microstrip computer-aided design," in *IEEE MTT-S Int. Microw. Symp. Dig.* IEEE, 1980, pp. 407–409.

[80] H. A. Wheeler, "Formulas for the skin effect," *Proc. IRE*, vol. 30, no. 9, pp. 412–424, 1942.

[81] W. C. Gibson, *The method of moments in electromagnetics*. CRC press, 2014.

[82] E. J. Wilkinson, "An n-way hybrid power divider," *IRE Trans. Microwave Theory Tech.*, vol. 8, no. 1, pp. 116–118, 1960.

[83] J. Reed and G. J. Wheeler, "A method of analysis of symmetrical four-port networks," *IRE Trans. Microwave Theory Tech.*, vol. 4, no. 4, pp. 246–252, 1956.

[84] S. Rodríguez, A. Fajardo, and C. I. Paez, "Characterization of the branch-line and rat-race ideal hybrids through their merit parameters," in *Proc. IEEE Latin American Symp. Circuits Syst.* IEEE, 2011, pp. 1–4.

[85] A. M. Niknejad, *Electromagnetics for high-speed analog and digital communication circuits*. Cambridge University Press, 2007.

[86] S. Nelson, A. Kraszewski, and T. You, "Solid and particulate material permittivity relationships," *J. Microw. Power Electromagn. Energy*, vol. 26, no. 1, pp. 45–51, 1991.

[87] R. Lohaus, "Simulation der Hefezelle (saccharomyces cerevisiae) und ihres Lebenszyklus," mbi Technical Report, at Deutsches Krebsforschungszentrum Heidelberg Abteilung Medizinische und Biologische Informatik, Tech. Rep., 2002.

[88] S. Aiba, S. Nagai, and Y. Nishizawa, "Fed batch culture of saccharomyces cerevisiae: a perspective of computer control to enhance the productivity in baker's yeast cultivation," *Biotechnol. Bioeng.*, vol. 18, no. 7, pp. 1001–1016, 1976.

[89] J.-Z. Bao, M. L. Swicord, and C. C. Davis, "Microwave dielectric characterization of binary mixtures of water, methanol, and ethanol," *The Journal of chemical physics*, vol. 104, no. 12, pp. 4441–4450, 1996.

[90] A. Bhattarai and S. Neupane, "Effects of concentration and solvent composition on the electrical conductivity of sodium bromide in pure water and ethanol-water mixed solvent media," *Kathmandu University Journal of Science, Engineering and Technology*, vol. 8, no. 2, pp. 1–6, 2013.

[91] A. Bhattarai, P. Nandi, and B. Das, "The effects of concentration, relative permittivity and temperature on the transport properties of sodium polystyrenesulphonate in methanol–water mixed solvent media," *J. Polym. Res.*, vol. 13, no. 6, pp. 475–482, 2006.

[92] H. K. B. Pandya, M. E. Austin, and R. F. Ellis, "Study of transmission line attenuation in broad band millimeter wave frequency range," *Rev. Sci. Instrum.*, vol. 84, no. 10, p. 103505, 2013.

[93] U. Kaatze, "Perspectives in dielectric measurement techniques for liquids," *Meas. Sci. Technol.*, vol. 19, no. 11, p. 112001, 2008.

[94] A. Roggenbuck, H. Schmitz, A. Deninger, I. C. Mayorga, J. Hemberger, R. Güsten, and M. Grüninger, "Coherent broadband continuous-wave terahertz spectroscopy on solid-state samples," *New J. Phys.*, vol. 12, no. 4, p. 043017, 2010.

[95] U. Kaatze, "The dielectric properties of water in its different states of interaction," *J. Solution Chem.*, vol. 26, no. 11, pp. 1049–1112, 1997.

[96] T. Meissner and F. J. Wentz, "The complex dielectric constant of pure and sea water from microwave satellite observations," *IEEE Transactions on Geoscience and remote Sensing*, vol. 42, no. 9, pp. 1836–1849, 2004.

[97] W. J. Ellison, "Permittivity of pure water, at standard atmospheric pressure, over the frequency range 0–25 THz and the temperature range 0–100°C," *J. Phys. Chem. Ref. Data*, vol. 36, no. 1, pp. 1–18, 2007.

[98] K. S. Cole and R. H. Cole, "Dispersion and absorption in dielectrics i. alternating current characteristics," *The Journal of chemical physics*, vol. 9, no. 4, pp. 341–351, 1941.

[99] ——, "Dispersion and absorption in dielectrics ii. direct current characteristics," *The Journal of Chemical Physics*, vol. 10, no. 2, pp. 98–105, 1942.

[100] F. Krewer, F. Morgan, and M. O'Halloran, "Development of accurate multi-pole debye functions for electromagnetic tissue modelling using a genetic algorithm," *Progress In Electromagnetics Research Letters*, vol. 43, pp. 137–147, 2013.

[101] C. G. Malmberg and A. A. Maryott, "Dielectric constant of water from 0° to 100°C," *J. Res. Nat. Bur. Stand.*, vol. 56, no. 1, pp. 1–8, 1956.

[102] K. Asami, "Characterization of biological cells by dielectric spectroscopy," *J. Non-Cryst. Solids*, vol. 305, no. 1, pp. 268–277, 2002.

[103] K. Asami, Y. Takahashi, and S. Takashima, "Dielectric properties of mouse lymphocytes and erythrocytes," *Biochimica et Biophysica Acta (BBA)-Molecular Cell Research*, vol. 1010, no. 1, pp. 49–55, 1989.

[104] K. Asami, T. Hanai, and N. Koizumi, "Dielectric analysis of escherichia coli suspensions in the light of the theory of interfacial polarization," *Biophys. J.*, vol. 31, no. 2, pp. 215–228, 1980.

[105] R. Hölzel and I. Lamprecht, "Dielectric properties of yeast cells as determined by electrorotation," *Biochimica et Biophysica Acta (BBA)-Biomembranes*, vol. 1104, no. 1, pp. 195–200, 1992.

[106] P. Höchtl, S. Boresch, and O. Steinhauser, "Dielectric properties of glucose and maltose solutions," *The Journal of Chemical Physics*, vol. 112, no. 22, pp. 9810–9821, 2000.

[107] J. C. Maxwell, *A treatise on electricity and magnetism.* Clarendon press, 1881, vol. 1.

[108] A. J. Deninger, T. Göbel, D. Schönherr, T. Kinder, A. Roggenbuck, M. Köberle, F. Lison, T. Müller-Wirts, and P. Meissner, "Precisely tunable continuous-wave terahertz source with interferometric frequency control," *Rev. Sci. Instrum.*, vol. 79, no. 4, p. 044702, 2008.

[109] M. L. Meade, "Advances in lock-in amplifiers," *J. Phys. E: Sci. Instrum.*, vol. 15, no. 4, p. 395, 1982. [Online]. Available: http://stacks.iop.org/0022-3735/15/i=4/a=001

[110] K. Martin, T. Henkel, V. Baier, A. Grodrian, T. Schön, M. Roth, J. M. Köhler, and J. Metze, "Generation of larger numbers of separated microbial populations by cultivation in segmented-flow microdevices," *Lab. Chip*, vol. 3, no. 3, pp. 202–207, 2003.

[111] M. Neshat and S. Safavi-Naeini, "Performance analysis of resonance-based transducers in terahertz bio-chips using equivalent surface impedance model," *IEEE Photonics Technology Letters*, vol. 22, no. 20, pp. 1512–1514, 2010.

[112] K. Schmalz, W. Winkler, J. Borngräber, W. Debski, B. Heinemann, and J. C. Scheytt, "A subharmonic receiver in SiGe technology for 122 GHz sensor applications," *IEEE J. Solid-State Circuits*, vol. 45, no. 9, pp. 1644–1656, Sept 2010.

[113] B. G. Hall, H. Acar, A. Nandipati, and M. Barlow, "Growth rates made easy," *Mol. Biol. Evol.*, vol. 31, no. 1, pp. 232–238, 2014. [Online]. Available: +http://dx.doi.org/10.1093/molbev/mst187

[114] H. Rücker, B. Heinemann, R. Barth, J. Bauer, K. Blum, D. Bolze, J. Drews, G. Fischer, A. Fox, O. Fursenko, T. Grabolla, U. Haak, W. Höppner, D. Knoll, K. Kopke, B. Kuck, A. Mai, S. Marschmeyer, T. Morgenstern, H. Richter, P. Schley, D. Schmidt, K. Schulz, B. Tillack, B. Weidner, W. Winkler, D. Wolansky, H. E. Wulf, and Y. Yamamototo, "SiGe BiCMOS technology with 3.0 ps gate delay," in *Proc. IEEE Int. Electron Devices Meeting*. IEEE, 2007, pp. 651–654.

[115] H. Rücker, B. Heinemann, W. Winkler, R. Barth, J. Borngräber, J. Drews, G. G. Fischer, A. Fox, T. Grabolla, U. Haak *et al.*, "A 0.13 SiGe BiCMOS technology featuring ft/fmax of 240/330 GHz and gate delays below 3 ps," *IEEE J. Solid-State Circuits*, vol. 45, no. 9, pp. 1678–1686, 2010.

[116] B. Heinemann, R. Barth, D. Bolze, J. Drews, G. G. Fischer, A. Fox, O. Fursenko, T. Grabolla, U. Haak, D. Knoll *et al.*, "SiGe hbt technology with ft/fmax of 300GHz/500GHz and 2.0 ps cml gate delay," in *Proc. IEEE Int. Electron Devices Meeting*. IEEE, 2010.

[117] U. L. Rohde, A. K. Poddar, and G. Böck, *The design of modern microwave oscillators for wireless applications: theory and optimization*. John Wiley & Sons, 2005.

[118] H. Hasegawa, M. Furukawa, and H. Yanai, "Slow wave propagation along a microstrip line on Si-SiO2 systems," *Proc. IEEE*, vol. 59, no. 2, pp. 297–299, 1971.

[119] A. M. Niknejad and H. Hashemi, *mm-Wave silicon technology: 60 GHz and beyond*. Springer Science & Business Media, 2008.

[120] Y. Mao, K. Schmalz, J. Borngräber, and J. C. Scheytt, "Comparison of 122 GHz LNAs in SiGe with different transmission line topologies," in *Proc. IEEE MTT-S Int. Microw. Works. Series Millim. Wave Integr. Technol.* IEEE, 2011, pp. 152–155.

[121] M. Kaynak, M. Wietstruck, C. B. Kaynak, S. Marschmeyer, P. Kulse, K. Schulz, H. Silz, A. Kruger, R. Barth, K. Schmalz, G. Gastrock, and B. Tillak, "BiCMOS integrated microfluidic platform for Bio-MEMS applications," in *Proc. IEEE MTT-S Int. Microw. Symp.* IEEE, 2014, pp. 1–3.